NASA CONTRACTOR REPORT 165744

CONSIDERATIONS IN THE DESIGN OF LARGE SPACE STRUCTURES

**John M. Hedgepeth, Richard H. MacNeal*,
Karl Knapp, and Charles S. MacGillivray**

Astro Research Corporation
Carpinteria, California 93013
*MacNeal Schwendler Corporation
Los Angeles, California 90041

**CONTRACT NAS1-15347
August 1981**

National Aeronautics and
Space Administration

Langley Research Center
Hampton, Virginia 23665

TABLE OF CONTENTS

CHAPTER 1:	DISTURBING TORQUES AND POINTING ERRORS - LARGE EARTH-ORIENTED MICROWAVE REFLECTORS	1
CHAPTER 2:	EFFECTS OF PHASE ERRORS ON ANTENNA PERFORMANCE	103
CHAPTER 3:	DEPLOYMENT OF FOLDED FOIL SURFACES	159
CHAPTER 4:	METEOROID DAMAGE TO ROD-TYPE STRUCTURAL ELEMETNS	219

CHAPTER 1

DISTURBING TORQUES AND POINTING ERRORS FOR LARGE EARTH-ORIENTED MICROWAVE REFLECTORS

by

Richard H. MacNeal

PREFACE

The successful performance of any structure depends largely on the identification of the critical or primary loads and design criteria on which the design is based. The future promises large structures which must be deployed, erected, assembled, or fabricated in space. For such structures, which will not be required to face the launch environment, the primary design requirements will be derived from the space-flight environment and will deal with phenomena as primary criteria which have been considered as only secondary in the past. The design of such genuine "space" structures will require a solid foundation of critical criteria.

Astro Research Corporation has a contract from NASA Langley Research Center to study critical design criteria for large space structures. The objective is to identify and establish critical baseline design requirements for a family of structures by a series of rational parametric analyses. The results, presented clearly and in detail, should improve the basis for future space structures system and technology efforts. They will also form the beginning of the needed solid foundation of design criteria.

This report is one of a series dealing with critical design requirements for large space structures. In particular, this chapter investigates the disturbing torques on large Earth-oriented parabolic reflectors and of methods to control the resulting pointing errors. The chapter considers an altitude range and ranges of reflector size, mass density, focal ratio, and pointing error which are sufficiently broad to cover most applications. This chapter was prepared at MacNeal-Schwendler Corporation under a subcontract from Astro Research Corporation.

CHAPTER 1

TABLE OF CONTENTS

SECTION 1: INTRODUCTION 9

SECTION 2: MISSION PARAMETERS AND CONTROL SYSTEM FUNCTION 10

SECTION 3: OVERTURNING MOMENTS AND POINTING ERRORS DUE TO ENVIRONMENTAL EFFECTS 11

3.1 Temperature Gradient and Thermal Shock. . . 12
3.2 Aerodynamic Drag 13
3.3 Solar Radiation Pressure 16
3.4 Micrometeoroids 19
3.5 Gravity Gradient 21

SECTION 4: CANDIDATE CONTROL SYSTEMS 23

4.1 Expelled Mass 27
4.2 Stored Angular Momentum 30
4.3 Gravity Gradient 35
4.4 Aerodynamic Pressure 35
4.5 Solar Radiation Pressure 37
4.6 Interaction with the Earth's Magnetic Field 40

SECTION 5: ANALYSIS OF GRAVITY GRADIENT CONTROL SYSTEMS . . 43

5.1 Stability and Pointing Error for an Uncontrolled Rigid Vehicle 43
5.2 Conceptual Design of a Gravity Gradient Control System 50
5.3 Steady State Pointing Errors 53
5.4 Dynamic Response 56

SECTION 6: ACTIVE CONTROL 58

SECTION 7: CONCLUDING REMARKS 59

REFERENCES 60

APPENDIX A: Effect on Pointing Error Due to Thermally Induced Length Changes in the Feed Supports. . . 59

APPENDIX B: Overturning Moment Due to Aerodynamic Drag . . . 71

APPENDIX C: Estimation of Pointing Error Due to Micrometeoroids 74

APPENDIX D: Complete Small Motion Equations for the Rotations of a Rigid Body in Circular Orbit. . . 80

APPENDIX E: Dynamic Analysis of the Pitching Moments of a Passive Gravity Gradient Control System 85

E.1 Equations of Motions 85
E.2 Calculation of Vibration Modes 87
E.3 Response to Sinusoidal Pitching Moment 88
E.4 Estimate of Modal Damping and Response to Random Excitation 90

APPENDIX F: Elimination of Steady-State Error by Integral Feedback 97

LIST OF TABLES AND FIGURES

Table 1.	Mission Parameters	61
Table 2.	Summary of Control Moment Sources	62
Table 3.	Steady Restoring Moments for Various Control Systems	63
Figure 1.	Equavilent Loading Pressure vs. Orbital Altitude	64
Figure 2.	Gravity Gradient Control System	65
Figure 3.	Steady Pitch Angle Due to Aerodynamic Drag with Gravity Gradient Stabilization	66
Figure 4.	Minimum Value of $m'z_a/m_r$ Required to Control Steady State Pitching Moment Due to Aerodynamic Drag	67
Figure 5.	Second Harmonic Pitch Angle Due to Solar Radiation Pressure with Gravity Gradient Stabilization.	68
Figure D-1.	Rigid Body Modes in Geocentric Orbit	84
Figure E-1.	Motions of System in Pitch Plane	93
Figure E-2.	Pitch Vibration Frequencies of Gravity Gradient Stabilized System	94
Figure E-3.	Relative Modal Displacements	95
Figure E-4.	Dynamic Amplification Factor for $\alpha = 10$	96
Figure F-1.	Block Diagram for Control System	101

LIST OF SYMBOLS

A. Root Symbols

A = area

B = magnetic field intensity

C = dimensionless coefficient

D = diameter of reflector

f = focal distance

g = damping coefficient

G = acceleration due to gravity at Earth's surface

h = altitude

H = angular momentum

I = moment of inertia; current

I_{sp} = specific impulse

k = dimensionless coefficient

ℓ = distance

m = mass

m' = mass per unit area of reflector aperture

M = moment

p = pressure; d/dt

r = radius

R = distance to center of Earth

R' = resistivity (ohm-meter)

t = time

T = tension

v = velocity; volume

x = distance from c.g. in forward direction along flight path

y = distance to right from c.g., looking forward

z = distance from c.g. downward toward Earth

α = angle of attack; dimensionless coefficient

γ = angle between sunline and normal to surface (or pointing axis)

ε = small number

ρ = density

σ = stress

ϕ = roll angle

θ = pitch angle

ψ = yaw angle

ω = frequency, rad/sec

Ω = orbital angular velocity, rad/sec

B. Subscripts

a , anchor

c , control

d , drag

e , expelled mass

o , steady value; overturning moment

i , inertia

m , moment; mission

r , reflector

s , solar radiation pressure

w , inertia wheel

SECTION 1
INTRODUCTION

One of the earliest types of large space structures will be parabolic microwave reflectors with diameters ranging from 100 meters to 1000 meters. An important application of such reflectors will be to conduct surveys of the Earth's surface in order to obtain prompt and detailed information regarding oceanographic and biological phenomena.

This chapter is part of a study of large space structures undertaken by Astro Research Corporation for NASA under Contract NAS1-15347. It reports the results of a general investigation of the disturbing torques on large Earth-oriented parabolic reflectors and of methods to control the resulting pointing errors. The chapter considers an altitude range and ranges of reflector size, mass density, focal ratio, and pointing error which are sufficiently broad to cover most applications.

SECTION 2

MISSION PARAMETERS AND CONTROL SYSTEM FUNCTION

The range of mission parameters to be investigated is shown in Table 1. The function of the control system is to maintain the pointing accuracy within the range of tolerance indicated in Table 1 (10^{-2} to 10^{-5} radian). No tolerance is given for the angular deviation about the pointing axis (yaw direction), but it can be assumed that some tolerance must exist, if the incoming radiation is polarized, or if the microwave beam is to be electronically scanned.

Since the orbit is assumed to be circular, the nominal pointing direction is toward the center of the Earth (geotropic). Thus, the vehicle must rotate at constant angular velocity once per orbit in the pitch direction. No excursions of any kind from this pointing direction are desired.

It will be noted from Table 1 that the ranges of the mission parameters and the pointing error tolerances are very broad. As a result, no single type of control system is optimum over the entire spectrum of parameters and tolerances. Unconventional control systems should be considered because the size and mass density parameters are outside the current state-of-the-art.

SECTION 3

OVERTURNING MOMENTS AND POINT ERRORS DUE TO ENVIRONMENTAL EFFECTS

The principal potential sources of pointing error in the vehicle's operational environment are

1. Temperature Gradient and Thermal Shock
2. Atmospheric Drag
3. Solar Radiation Pressure
4. Micrometeoroids
5. Gravity

Each of these items is discussed in separate subsections. Figure 1 summarizes and compares equivalent loading pressures as a function of orbital altitude due to atmospheric drag, solar radiation pressure, and the combined effect of gravity gradient and unsymmetrical mass distribution. The following conditions are assumed in Figure 1.

- Drag Coefficient, $C_D = 2.5$
- Normal incidence and perfect reflection of solar radiation
- Worst case orientation (45°) of the mass unbalance (mass per unit area times distance) from the geocentric direction, i.e., the pointing axis.

Within the range of orbital altitudes considered in this study (200 km to geosynchronous), one or another of the three effects dominates the others at different altitudes.

Maneuvers are not a source of pointing error, because it is not required that the vehicle exercise maneuvers. Moments due to interaction with the Earth's magnetic field, which are significant for some spinning spacecraft, are not considered to be significant for the mission under consideration. They can, however, be used as a means of active control, see Section 4.6.

3.1 Temperature Gradient and Thermal Shock

Temperature gradients occur for various reasons including the facts that some parts of the vehicle are shaded from the Sun by others, and that the entire vehicle may pass into the shadow of the Earth. The main effect of temperature gradient on pointing accuracy is to cause thermal strains which distort the shape of the reflector and thereby change the pointing axis. Such errors cannot be detected by simple devices, and they are beyond the scope of the present investigation. Appendix A includes a very simple analysis of the effect on pointing accuracy of thermally induced length changes of the feed supports. It is shown that the pointing errors in radians is of the same order of magnitude as the differences in the thermal strains, and that the allowable differential strain decreases as f/D increases.

The effects of thermal shock caused by a rapid change in temperature are similar in nature, except that inertia forces are brought into play. Thermal shock occurs when the vehicle passes into the Earth's shadow. At 500 km altitude, for example, the time to cross the penumbra is about 8 seconds, so that structural modes with periods this long or longer will respond dynamically. Cumulative changes in the pointing direction due to nonlinear kinematic effects will be much smaller than the linear effects and may be disregarded, provided that some form of directional stability is provided.

3.2 Aerodynamic Drag

Newtonian flow theory may be used to estimate the aerodynamic forces and moments at orbital altitudes. In Newtonian flow, the pressure is normal to the surface and has the magnitude

$$p = \frac{1}{2}\rho V^2 C_N \cdot \sin^2\alpha \qquad (1)$$

where

$\frac{1}{2}\rho V^2$ = dynamic pressure

C_N = normal force coefficient (2.5)

α = angle of attack

Both density and velocity are functions of altitude. The following table gives values of p vs. altitude for $\alpha = \pi/2$.

h (km)	$P_d = \frac{1}{2}\rho V^2 C_N$ N/m^2
300	300×10^{-5}
400	60
500	20
600	6
700	2
800	.8
900	.4
1000	0.15

It is noteworthy that P_d is less than p_s, the solar radiation pressure at normal incidence, for altitudes greater than 800 km, see Figure 1.

If the vehicle is symmetrical, the only component of moment due to aerodynamic pressure is in the pitch direction (normal to the plane of the orbit). Incidental or accidental lack of symmetry causes small moments in the roll and yaw directions.

If the surface of the reflector is smooth and if it is assumed, for convenience, to be spherical, then, clearly, the center of pressure passes through the center of the sphere. The moment arm between this point and the center of gravity is slightly less than 2f, where f is the focal distance. An expression for the moment is

$$M_d = C_m \frac{\pi}{4} P_d D^3 \qquad (2)$$

where D is the diameter of the reflector and C_m is a coefficient which depends on the focal ratio as shown in the following table

f/D	C_m
0.5	.0117
1.0	.00277
2.0	.000672

The values of C_m are derived in Appendix B. If the surface of the reflector is not smooth, (for example, a surface consisting of a grid work of wires) the force per unit area will be greater, but the moment arm will be less, resulting in a moment coefficient of the same order as C_m in the table shown above. It is also possible, with non-smooth surfaces, to balance the drag forces by design so as to achieve zero net pitching moment.

In order to appreciate the magnitude range of the pitching moment due to aerodynamic drag, consider the following table which records M_d vs. D and f/D for h = 500 km.

f/D \ D	100 m	300 m	1000 m
	M (Newton-meters)		
0.5	1.9	49.7	1842
1.0	0.5	11.7	434.5
2.0	0.1	2.9	106.1

For h = 300 km, the moments are an order of magnitude larger and for h = 700 km, they are an order of magnitude smaller. For non-solid surfaces, the moments should be reduced by the surface solidity ratio.

Since the orientation of the vehicle remains constant with respect to the flight path, the dynamic component of aerodynamic moment is very small. Control surfaces may, however, be used to produce dynamically varying aerodynamic moments, see Section 4.4.

3.3 Solar Radiation Pressure

Solar radiation pressure is a significant source of overturning moment for large spacecraft. For a perfect reflector, the pressure is normal to the surface and has the magnitude

$$p = p_s \cos^2\gamma \tag{3}$$

where $p_s = .9\text{x}10^{-5}$ N/m^2 near the Earth

γ = angle between Sun line and normal to surface.

For a perfectly absorbing surface which radiates equally from both sides, the pressure is directed away from the Sun and has the magnitude

$$p = \frac{1}{2} p_s \cos\gamma \tag{4}$$

Equation (3) will be used for the purpose of estimation, except that p_s will be reduced to $.75\text{x}10^{-5}$ N/m^2 to account for absorptivity.

A method has been developed in Reference 1 to calculate the moment due to radiation pressure on a perfectly reflecting cylindrical segment of small included angle. The moment per unit length about the midchord of the strip, as predicted by the method, is

$$m_\theta = \frac{1}{12} p_s C^3 \sin 2\gamma / R_c \tag{5}$$

where C is chord of the cylindrical segment, R_c is its radius of curvature, and γ is the angle between the normal to the surface and a line pointing at the Sun. Note that the magnitude of the moment is maximum for $\gamma = 45°$ plus multiples of 90°. For Sun angles near 90° and 270°, some parts of the reflector shade other parts and Equation (5) becomes inapplicable, although it is clear, in any case, that the moment should change sign near $\gamma = 90°$.

Equation (5) is adequate to make rough estimates of the moments on a spherical reflector, with the following identifications:

C = D, the diameter of the spherical reflector

R_c = 2f, the radius of the spherical reflector

$\frac{m_\theta}{c} = \frac{M_\theta}{\frac{\pi}{4} D^2}$, the moment per unit area

then

$$M_\theta = k_s \frac{\pi}{4} p_s D^3 \tag{6}$$

where

$$k_s = \frac{1}{24} \frac{D}{f} \sin 2\gamma \tag{7}$$

The following table evaluates k_s for various values of the focal ratio, f/D, and $\gamma = 45°$.

f/D	k_p
0.5	.0833
1.0	.0417
2.0	.0208

Since the axis of the reflector points toward the center of the Earth at all times, the angle between the Sun line and the axis will vary in a manner that depends on the orbit. If the Sun line is normal to the plane of the orbit, then $\gamma \simeq 90°$ at all times, and the overturning moments are small and steady. If the Sun line is tangent to the plane of the orbit, γ will rotate through 360° in one orbital revolution and the pitching moment will exhibit a strong 2/rev component. Such trajectories may also pass

through the Earth's shadow, further complicating the harmonic content of the overturning moment. The transfer from light to darkness through the penumbra at an altitude of 500 km requires about eight seconds which is less than one-thousandth of the orbital period. The gradient of light intensity across the reflector disk is not significant during passage of the penumbra, which has a length of 60 km at 500 km altitude. In addition, the angle between the Sun line and the plane of the orbit will show an annual variation, unless the orbit is in the ecliptic plane.

For non-solid smooth surfaces, the moments should be reduced by the surface solidity ratio. For a surface consisting of wires with circular cross-section, the moments will be zero unless some parts shade others. For real structures, the calculation of k_s in Equation (6) will require detailed analysis.

3.4 Micrometeoroids

A worst case analysis of the pointing error due to meteoroid impact is worked out in Appendix C. It is shown there that the maximum error angle due to multiple impacts of small meteoroids (micrometeoroids) is

$$\theta_{max} = \frac{k(m')^2}{D^2(\omega^3 g)^{1/2}} \qquad (8)$$

where k is a constant, ω is the natural frequency in pitch, and $g = 2C/C_c$ is the damping coefficient of rigid body pitching oscillations.

In Equation (8), it is assumed that the reflector is a shell of uniform thickness which is penetrated by large micrometeoroids. Open construction, or concentrated reinforcement, increases the probability of severe structural damage and occasional large pointing disturbances due to heavy impacts.

If the following worst case values are assumed:

$\theta_{max} = 10^{-5}$ radian

$m' = 1$ kg/m^2

$D = 100$ m

$\omega = 10^{-3}$ rad/sec (approximate orbital frequency for altitudes below 1000 km)

then the required amount of damping is $g = 7.3 \times 10^{-4}$. This is a very small value which should be exceeded for other reasons.

Although micrometeoroids do not appear to be a significant source of pointing error for the range of vehicle parameters considered in the present study, it is clear from Equation (8) that their effect is magnified for the smaller, denser vehicles which typify conventional spacecraft design.

Also, the possibility of severe structural damage due to meteoroids should not be overlooked, particularly for vehicles with a large running length of structural reinforcement. Redundant design is the order of the day for such members (see Reference 2).

3.5 Gravity Gradient

Gravity gradient is a strong source of overturning moment for orbiting spacecraft which are required to point in arbitrary directions. In the present case, the desired pointing axis is toward the center of the Earth, and the vehicle is in a circular (or nearly circular) orbit. For this case, the vehicle can be designed so that gravity gradient is a source of stability rather than a source of disturbing torque. If the principle axis of inertia with the least polar moment of inertia is aligned with the pointing axis, then gravity gradient will tend to resist overturning moments (see Appendix D). If, in addition, the intermediate principle axis of inertia is aligned with the flight path, gravity gradients will tend to resist yawing moments (moments about the pointing axis).

If the principle axes of inertia are not aligned with the pointing axis and with the flight path, gravity gradient will produce moments whose magnitudes may be computed by Equation (6) of Appendix D. They are proportional to the cross-products of inertia which are under design control (within manufacturing tolerance).

A more serious requirement is that the pointing axis be the axis of least polar moment of inertia in order to achieve stability. This is illustrated by the following table which indicates the minimum ratio of feed mass to reflector mass required to obtain stability for reflectors with various f/D ratios. (The mass of the reflector is assumed to be uniformly distributed and the feed supports are assumed to be massless.)

f/D	$m_{feed}/m_{refl.}$
0.5	.50
1.0	.07
2.0	.015

Since the indicated feed mass may be larger than that desired for other reasons, a potential stability problem arises which can be solved either by placing additional mass on the pointing axis or by providing an active control system. This subject is treated later.

Another important effect is that, if the orbit is noncircular, the pitching angular velocity required to point the reflector toward the center of the Earth is not constant. This effect, although important, is beyond the scope of the present investigation. It results in a scanning velocity, as measured at the surface of the Earth, that is nonuniform, but predictable.

The effects of variations in the magnitude of the gravitational constant (oblateness) will be discussed later in connection with the stability of a gravity-gradient control system, Section 5.1.

SECTION 4
CANDIDATE CONTROL SYSTEMS

As applied to attitude control, a control system consists of a means to detect angular error, a means to apply a mechaniccal moment to correct the error, and a means to modify the moment in response to the error. A control system is passive if all three elements of the system are combined in the same mechanism. Otherwise, it is active. The advantages usually attributed to passive control systems are that they are more reliable and less subject to instability. Their principle disadvantage is larger weight for the same error.

Emphasis will be placed, in the present discussion, on the means to apply a moment. The other elements of an active control system are conventional and have no unusual requirements in the present application.

The source of moment to correct angular error may either be internal (expelled mass or stored angular momentum) or it may be external, deriving from environmental effects such as gravity gradient and solar radiation pressure. The external sources of moment are particularly interesting for the present application because their intensity is weak compared to internal sources, and consequently they require large physical dimensions in order to be effective. For the same reason they are not particularly attractive for small spacecraft.

The properties of seven different sources of control moment are summarized in Table 2. The first three employ internal sources of control moment and the last four employ external (environmental) sources. Formulas for the control moments provided by each of the seven sources are given in Table 3. Each of the candidate control systems will be discussed in separate

subsections, but it is useful to examine the summary information presented in Tables 2 and 3 before going into the details.

It will be noted from Tables 2 and 3 that the internal sources of control moment are not altitude dependent, in contrast to the external sources which are, with the exception of solar radiation pressure which depends only on distance from the Sun. The effect of radiation pressure is, however, so weak that it is masked by aerodynamic pressure at low altitudes, as indicated in Table 2. The same is true of gravity gradient and the Earth's magnetic field with the added restriction of a practical upper altitude limit due to $1/R^3$ decay of both effects (see Table 3, last column). Aerodynamic pressure decays rapidly with altitude and is unusable as a source of control moment above 1000 km altitude. Thus, it is seen that no single external source of control moment is practical within the entire altitude range of the present study (200 - 30,000 km).

The practical size ranges shown in Table 2 are derived from detailed analysis supporting the present study, but they can be inferred, to some extent, from the formulas presented in Table 3 and from previous discussion.

The discussion of Section 3 showed that aerodynamic pressure and solar radiation pressure are the largest sources of overturning moments for the present application. Therefore, the use of the same sources to provide control moments should not result in any preferences with regard to size. The control moment available from gravity gradient, on the other hand, is seen to depend on the fourth power of vehicle size rather than on the third power. Thus, gravity gradient should be a powerful source of control moment for large vehicles, as indicated in Table 2.

The instantaneous value of the control moment available from expelled mass can be very high, but the average long term value is limited by weight considerations. Thus, the major limitation on the use of expelled mass (in particular, chemical propulsion) is the duration of the mission, which must be long for large expensive spacecraft in order to return initial investment. The size of the vehicle does not directly affect the effectiveness of expelled mass relative to aerodynamic pressure and solar radiation pressure.

Control systems which utilize stored angular momentum are penalized in the present application by a limitation on their size and by the constant vehicle angular velocity required by geotropic pointing. The size limitation derives from the fixed diameter of the launch vehicle and from the assumption that it will be impractical, for the foreseeable future, to construct a high performance inertia wheel in space. Fixed size degrades performance relative to environmental effects because the stored angular momentum, H, is proportional to the diameter of the wheel, given a fixed mass and optimized material selection, whereas the overturning moments are proportional to the cube of the diameter of the vehicle.

Geotropic pointing limits the axis of the wheel to be the pitch axis (normal to the orbital plane) with the result that control from stored angular momentum can only be achieved by a combination of momentum bleeding (pitch axis) and gyrostabilization (roll and yaw axes). Gyrostabilization is particularly weak for large vehicles as shown by the formula in Table 3.

The conclusions in Table 2 regarding use of the Earth's magnetic field are based on a study, Reference 3, in which the vehicle was very large

(1500 m) and very light (.001 kg/m^2). For this case magnetic field interaction appeared to be a very effective means of control.

The answers to the questions regarding passive and active control posed in Table 2 are in most cases self-evident, particularly if the requirements of the present application are considered. For example, a passive control system based on aerodynamic pressure (i.e., simple aerodynamic control surfaces) is possible because the velocity vector has a fixed orientation with respect to the vehicle. Solar radiation pressure cannot be so used because its direction and magnitude change continuously relative to vehicle axes.

4.1 Expelled Mass

If gas jets are placed at four equally spaced points on the perimeter of the reflector, then the average available long-term restoring moment about a transverse (pitch or roll) axis is

$$M_e = \frac{G\, m_e\, I_{sp}\, D}{4 t_m} \tag{9}$$

where G = acceleration of gravity

m_e = stored mass of expellant

I_{sp} = specific impulse

D = diameter of reflector

t_m = mission duration

In order to estimate the required value of m_e, assume that M_e opposes an overturning moment due to solar radiation pressure. Solar radiation pressure provides a good example because it is independent of orbital altitude. Equations (6) and (7) of Section 3.3 provide an expression for the maximum overturning moment due to radiation pressure. If it is assumed that $f/D = 1.0$, and that the average overturning moment is equal to one-half of the maximum value, then the overturning moment is

$$M_o = .0208 \cdot \frac{\pi}{4} p_s\, D^3 \tag{10}$$

In Equation (9), substitute

$$m_e = m'_e \cdot \frac{\pi}{4} D^2 \tag{11}$$

Then, by equating M_e to M_o

$$m'_e = \frac{.0832\ p_s\ t_m}{G\ I_{sp}} \tag{12}$$

which shows that, m'_e, the propellant mass per unit of reflector area, is independent of vehicle size. As an example, select

$$p_s = .75 \times 10^{-5}\ N/m^2$$

$$t_m = 10\ \text{years} = 3.15 \times 10^8\ \text{sec}$$

$$G = 9.81\ m/sec^2$$

$$I_{sp} = 200\ \text{sec}$$

where the value of I_{sp} is typical for chemical propulsion.

For this example, $M'_e = .1002\ kg/m^2$. Referring to Table 1, the range of the mass per unit area of the reflector is from .01 to 1.0 kg/m^2. It is seen that the required propellant mass is excessively large, at least for the low range of reflector mass density.

The required propellant mass to overcome solar radiation pressure can be reduced dramatically by using open wire construction for the reflector rather than solid construction, as mentioned in Section 3.3.

Much lower values of m'_e can be achieved by using solar electric propulsion (ion propulsion) which electrically accelerates charged particles. Energy is provided by solar cells. Values of I_{sp} of the order of 10,000 are technically possible for ten years of continuous thrust, Reference 4, but the level of technical complexity is high.

At low altitudes an exactly similar method may be used to estimate the expelled mass required to resist overturning moment due to aerodynamic drag. A related problem, which may set a minimum feasible altitude, is orbital decay due to aerodynamic drag. Mass can be expelled continuously at a low rate to resist the drag force. The force exerted by expelled mass is

$$F_e = \frac{Gm_e I_{sp}}{t_m} \tag{13}$$

The drag force for a smooth reflector is

$$F_d = C_d \cdot \frac{\pi}{4} p_d D^2 \tag{14}$$

The drag coefficient C_d is evaluated in Appendix B as a function of f/D. For f/D = 1.0, C_d = .00138. Using this value, the required expelled mass per unit area is, from Equations (11), (13) and (14)

$$m'_e = \frac{.00138\ p_d\ t_m}{G\ I_{sp}} \tag{15}$$

As an example, select

$m'_g = .01\ Kg/m^2$

$t_m = 10$ years $= 3.15 \times 10^8$ sec

$G = 9.81\ m/sec^2$

$I_{sp} = 200$ sec

and calculate p_d and the corresponding altitude. For this example $p_d = 4.51 \times 10^{-5}$ and the altitude is, from the short table given in Section 3.2, about 650 km. Increasing the expellant mass by a factor of ten decreases the altitude to about 450 km. The use of solar electric propulsion would appear to be the only practical method to achieve even lower altitudes for the application considered in this report.

4.2 Stored Angular Momentum

As indicated in previous discussion, stored angular momentum is not an attractive source of restoring moment for the application treated in this report.

As an exercise, consider the use of inertia bleeding from a wheel mounted parallel to the pitch axis, which is the only possible axis, given a geotropic pointing axis. The available angular momentum of an inertia wheel is, assuming maximum efficient use of materials,

$$H = r\, m_w \sqrt{\frac{\sigma}{\rho}} \tag{16}$$

where r = radius of the wheel

m_w = mass of the wheel

σ = allowable material stress

ρ = material density

The average restoring moment is

$$M_w = H/t_m \tag{17}$$

where t_m is the mission duration. The ratio of the restoring moments available from an inertia wheel and from expelled mass is, from Equations (9), (16) and (17)

$$\frac{M_w}{M_e} = \left(\frac{m_w}{m_e}\right) \cdot \left(\frac{r}{D}\right) \cdot \left(\frac{4\sqrt{\frac{\sigma}{\rho}}}{G\, I_{sp}}\right) \tag{18}$$

For graphite composite, which is probably the best available material,

$$\sigma = 5 \times 10^8 \text{ n/m}^2$$

$$\rho = 1522 \text{ Kg/m}^3$$

and $\sqrt{\sigma/\rho} = 573.2$ m/sec

Thus, using $G = 9.31$ m/sec^2 and $I_{sp} = 200$ sec

$$\frac{M_w}{M_e} = 1.16 \left(\frac{m_w}{m_e}\right)\left(\frac{r}{D}\right) \tag{19}$$

In order for the inertia wheel to be competitive with expelled mass, it is seen that the radius of the wheel, r, should be of the same order as the diameter of the reflector, which is considered to be impractical if the required value of r is greater than the radius of the launch vehicle, as previously discussed. This result applies only to the average moment and not to dynamic variations. In the case of the latter, the momentum wheel is greatly superior to expelled mass because it does not run down.

For moments whose axes are normal to the axis of the wheel (roll and yaw axes) the inertia wheel acts as a gyrostabilizer. The equations for motion about the roll and yaw axes are, in matrix form,

$$\begin{bmatrix} I_x p^2 & Hp \\ -Hp & I_z p^2 \end{bmatrix} \begin{Bmatrix} \phi \\ \psi \end{Bmatrix} = \begin{Bmatrix} M_x \\ M_z \end{Bmatrix} \tag{20}$$

where x = roll axis

z = yaw axis

ϕ = roll angle

ψ = yaw angle

I_x = moment of inertia about roll axis

I_z = moment of inertia about yaw axis

$p = d/dt$

H = angular momentum of inertia wheel.

For the case of a steady rolling moment, M_x, Equation (20) may be solved to give

$$\phi = \frac{I_z}{H^2} M_x$$

$$\psi = \frac{M_x t}{H} \tag{21}$$

Both I_z and M_x increase rapidly with vehicle size, while H is fixed by dimensional constraints. Thus, gyrostabilization becomes increasingly less attractive as the size of the vehicle is increased. Consider, for example, that M_x is equal to the maximum moment produced by solar radiation pressure on a reflector with f/D = 1. The moment, obtained from Equation (10) with $p_s = .75 \times 10^{-5}$ N/m^2, is

$$M_o = 1.23 \times 10^{-7} D^3 \tag{22}$$

The angular momentum for the wheel, obtained from Equation (16) with r = 2m, and $\sqrt{\sigma/\rho}$ = 573.2 m/sec, is

$$H = 1146\ m_w \tag{23}$$

An approximate value of the polar moment of inertia of the vehicle is

$$I_z = \frac{1}{8} m_r D^2 \tag{24}$$

where m_r is the mass of the reflector. Using Equations (22), (23), and (24), the roll angle ϕ computed from Equation (21) is:

$$\phi = 1.17 \times 10^{-14} \, m_r D^5 / m_w^2 \tag{25}$$

Since

$$M_w = \frac{\pi}{4} D^2 \, m'_w \tag{26}$$

where m'_w is the mass per unit area, Equation (23) can be written

$$\phi = 1.49 \times 10^{-14} \, \frac{m' D^3}{(m'_w)^2} \tag{27}$$

If the mass of the inertia wheel is permitted to be ten percent of the mass of the reflector, then

$$\phi = 1.49 \times 10^{-12} \, \frac{D^3}{m'} \tag{28}$$

Both D and m' may vary over wide ranges as indicated in Table 1. The most favorable values of D and m' are D = 100 m and m' = 1 kg/m^2. In this case,

$$\phi = 1.49 \times 10^{-6} \text{ radian} \tag{29}$$

The least favorable values of D and m' are D = 1000 m and m' = .01 kg/m^2. In this case

$$\phi = .149 \text{ radian} \tag{30}$$

The value given by Equation (29) is less than the smallest pointing error tolerance listed in Table 1, while the value given by Equation (30) is greater than the largest tolerance. Note that these values are instantaneous values.

The yaw angle due to steady rolling moment, obtained from Equation (8), using Equations (22), (23) and (24) is

$$\psi = 1.37 \times 10^{-10} \frac{D\,t}{m'_w} \tag{31}$$

Assuming t = 10 years = 3.15×10^8 sec, and using the favorable values D = 100 m and $m'_w = 0.1$ kg/m^2, produces

$$\psi = 43.16 \text{ radians} \tag{32}$$

which indicates the inability of the gyrostabilizer to resist steady moments for long time periods.

In summary, the prescribed spectrum of mission parameters does not appear to favor a control system based on stored angular momentum.

4.3 Gravity Gradient

Gravity gradient is a strong candidate for control of the vehicle considered in this report, because the pointing axis is geotropic and because the diameter of the reflector is large. Large diameter favors a gravity gradient control system because the control moment is proportional to the fourth power of diameter, which is a higher power than that for any other candidate system.

A detailed study of gravity gradient control for the present application is contained in Section 5.

4.4 Aerodynamic Pressure

Aerodynamic pressure is a candidate for control of the vehicle at altitudes below 1000 km. Due to geotropic pointing, the flow velocity is steady relative to the vehicle, and aerodynamic control surfaces similar to those of a conventional airplane can be used. Pitch and yaw can be controlled with passive (fixed) control surfaces but roll cannot. In any event, the addition of active control greatly increases the effectiveness. For example, active trim control can reduce the steady pitch error to zero.

If the altitude is low enough, pitching moment due to aerodynamic drag will be the only important component of overturning moment and for this case it is relatively easy to size the aerodynamic surfaces required to control pitch. The overturning moment for a smooth reflector is evaluated from Equation (2) of Section 3.2 and the accompanying table of pitching coefficients vs. f/D. Selecting f/D = 1.0, the pitching moment about the center of gravity is

$$M_o = .00277\ p_d\ A_r \cdot D \tag{33}$$

where p_d is the stagnation pressure and A_r is the area of the reflector. Consider a control surface of area A_c, placed at a distance D/2 behind the center of gravity with an angle of attack α. From Equation (1) of Section 3.2 the control moment is

$$M_c = \sin^2\alpha \cos\alpha\ p_d\ A_c \cdot D/2 \tag{34}$$

Equating M_c to M_o gives

$$\sin^2\alpha \cos\alpha = .00554\ A_r/A_c \tag{35}$$

The maximum value of $\sin^2\alpha \cos\alpha$ is .385 at $\alpha = 54.7°$. Thus, the minimum value of A_c/A_r is

$$A_c/A_r = .00554/.385 = .0144 \tag{36}$$

A somewhat larger control surface should be used to provide a margin of safety and also to reduce the drag of the control surface, which is proportional to $\tan\alpha$. Note also, from data presented in Section 3.2, that the size of the overturning moment is a strong function of f/D.

The control surfaces required for roll and yaw are much smaller (at low altitudes) because the roll and yaw moments are much smaller.

4.5 Solar Radiation Pressure

At altitudes above 700 Km, the maximum overturning moment due to solar radiation pressure exceeds the steady pitching moment due to aerodynamic drag, which suggests that solar radiation pressure may be used for control at such altitudes. Furthermore, in deep space, and also in geosynchronous orbit, solar radiation pressure is the largest of the environmental effects that are available for vehicle control, exceeding even gravity gradient.

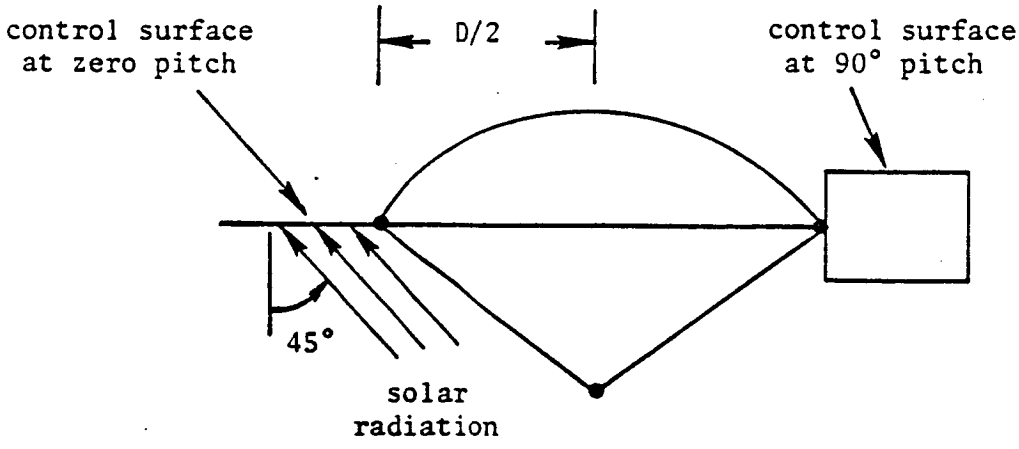
Solar radiation pressure is the basis of solar sail propulsion which has been extensively studied, References 1, 5, 6, and 7, and which is competitive with solar electric propulsion for high energy interplanetary missions of long duration, Reference 4.

For the present application, control moments can be provided by orientable reflecting panels attached to the periphery of the reflector. Formulas for control moments as functions of panel orientation and the Sun direction are published in Reference 8. Since the orientation of the vehicle relative to the direction of the Sun changes continuously during each orbit, the control surface orientations must change continuously and they must, furthermore, be actively controlled.

At altitudes greater than 1000 Km, solar radiation pressure is the dominant source of overturning moment for the present application, and it is relatively easy to size the reflecting panels in this case. The overturning moment is maximum for a Sun angle of 45°, as discussed in Section 3.3. For $f/D = 1.0$, the maximum overturning moment on a smooth control panel is

$$M_o = .0417\, p_s A_c D \tag{37}$$

where p_s is the solar radiation pressure for normal incidence, and A_c is the area of the panel. Assume that two control surfaces are located at a distance D/2 from the center of gravity and oriented as shown in the following sketch.



The force on the left-hand control surface is

$$F = p_s A_c \cdot \cos^2(45°) = \frac{1}{2} p_s A_c \tag{38}$$

and the force on the right-hand surface is zero. The resulting control moment is

$$M_c = \frac{1}{4} p_s A_c D \tag{39}$$

Equating M_c to M_o gives the required size of the control surface

$$A_c = .167\, A_r \tag{40}$$

A variable control moment is produced by pitching the axes of the control surfaces. Since at least three control surfaces are required, the total control surface area equals at least one-half of the reflector area for f/D = 1.0. Smaller control surfaces can be achieved by placing them at a greater distance from the reflector, at an added cost in weight and complexity. Typically, the mass of a control panel, using available materials, is about .01 kg/m^2.

Very much smaller control surfaces are required if the reflector is constructed from a network of wires which produce very little net overturning moment due to radiation pressure.

4.6 Interaction with the Earth's Magnetic Field

If a current, I, flows through a circular loop of wire whose plane is parallel to a magnetic field of intensity, B, the wire experiences a torque

$$M = \frac{\pi}{4} D^2 \, I \, B \tag{41}$$

about an axis perpendicular to the magnetic field and tangent to the current loop. The use of this principle for the control of orbiting spacecraft by interaction with the Earth's magnetic field has been explored in Reference 3 and is the basis of control for a proposed low frequency orbiting radio telescope (LOFT), Reference 9. In that application the purpose of control was to produce useful scanning rates for a very large (1500 m) reflector. Several current loops were provided, of which one was the rim of the reflector, and the others included meridional segments. Control laws were fairly complex. They required sensors to detect the magnetic field and computers to select the current loops. The weight of the control system was less than that of competing systems.

Magnetic interaction has limited utility for the present application because it is not possible to produce a torque about an axis which coincides in direction with the magnetic field. In the case of an orbit in the magnetic equatorial plane, this axis would be the pitch axis, and in the case of a polar orbit it would be an axis in the longitudinal (roll-yaw) plane which varies with orbital latitude. Thus, to be useful, magnetic interaction must be supplemented by some other source of moment.

In order to compare the mass of a magnetic-interaction control system with that of other systems, the current, I, in Equation (41) should be expressed in terms of the mass of the control system. The mass of the system is concentrated in two components, a power source, probably utilizing solar cells, and the conductors which carry the current. Assuming that the mass of the power source is proportional to its rated power, it can easily be shown that, for an optimized design, the rated current is

$$I = \frac{D\, m'_c}{8\sqrt{C\, R'\, \rho}} \tag{42}$$

where D = diameter of the loop

m'_c = control system mass divided by reflector area

C = power source mass divided by power

R' = resistivity of conductor material

ρ = density of conductor material

Upon inserting this value of I into Equation (39), it is seen that the maximum available control moment is proportional to $m'_c D^3$. In this respect a magnetic interaction control system is similar to most of the previously examined control systems including expelled mass, aerodynamic control, and control by solar radiation panels.

In order to evaluate the mass of a magnetic interaction control system relative to other types, assume the following conditions

$B = 10^{-5}$ webers/m^2 (typical for an altitude of 6000 Km)

$C = .05$ kg/watt

$R' = 2.83 \times 10^{-8}$ ohm-meter

$\rho = 2700$ Kg/m^3

} values for commercial aluminum wire

and compute the maximum available torque. For these conditions

$$M = \frac{\pi D^3 m_c' B}{32 C R' \rho} = \frac{D m_c B}{8\sqrt{C R' \rho}} = 64 \times 10^{-5} D m_c \qquad (43)$$

For comparison, the control moment for a solar radiation control panel, given by Equation (39) of Section 4.5, is

$$M = \frac{1}{4} p_s A_c D \qquad (44)$$

Assuming $p_s = .75 \times 10^{-5}$ N/m^2 and $A_c/m_c = 100$ m^2/kg, gives

$$M = 18.75 \times 10^{-5} D m_c \qquad (45)$$

which is seen to be less than that for the magnetic interaction control system. Note, however, that the Earth's magnetic field decays as $1/R^3$, so that magnetic field interaction is not competitive with solar radiation control panels at a geosynchronous altitude.

SECTION 5

ANALYSIS OF GRAVITY GRADIENT CONTROL SYSTEMS

A gravity gradient control system is particularly suitable for the mission considered in this report because the pointing axis is geotropic and because the diameter of the reflector is large. Accordingly, more space is assigned to gravity gradient control than to the other types discussed in the previous section.

The discussion begins with passive gravity gradient control of a rigid body and proceeds to consideration of a control system which includes flexible structural elements and, possibly, active control elements.

5.1 Stability and Pointing Error for an Uncontrolled Rigid Vehicle

The complete small motion equations for the rotations of a rigid body in circular orbit are derived in Appendix D. The assumed equilibrium state is a circular orbit with the pointing axis directed toward the center of the Earth, and with zero angular velocity about the pointing axis. This state corresponds exactly to the desired orientation of a geotropic reflector.

The conditions for stability of the desired orientation, as derived in Appendix D, are

$$I_{zz} > I_{xx} > I_{yy} \tag{46}$$

where

$$I_{zz} = \int \rho_z^2 \, dv \quad , \text{etc.} \tag{47}$$

and x = distance from cg in forward direction along flight path

y = distance from cg to right, looking forward

z = distance from cg downward toward Earth.

For a vehicle which is symmetrical about the pointing axis, $I_{xx} = I_{yy}$. I_{zz} depends on the focal ratio, f/D, and on the mass placed at the feed. The following table shows the approximate minimum value of the feed mass required to satisfy the stability conditions.

f/D	$\frac{m_{feed}}{m_{refl}}$
0.5	.50
1.0	.07
2.0	.015

If the stability conditions are not satisfied, then some means of stability augmentation must be supplied. The simplest, but not necessarily the lightest method, is to add mass to a point on the pointing axis that is far from the center of gravity. Alternatively, some other form of stability augmentation may be used, employing any of the physical principles described in Section 4.

If the stability conditions are satisfied, the angular errors may be found from Equation (2) of Appendix D. Since the cross-products of inertia are zero in the assumed load-free equilibrium state, the rotations due to small steady loads are determined by the following simple uncoupled formulas

$$\phi = \frac{M_x}{4\Omega^2\left(I_{zz} - I_{yy}\right)} \tag{48}$$

$$\theta = \frac{M_y}{3\Omega^2\left(I_{zz} - I_{xx}\right)} \tag{49}$$

$$\psi = \frac{M_z}{\Omega^2 \left(I_{xx} - I_{yy}\right)} \tag{50}$$

where Ω is the orbital angular velocity (2π divided by the orbital period). Values of Ω^2 vs. altitude are given in the following table for the range of altitudes considered in this study.

Altitude (Km)	0	500	1000	2000	5000	10,000	20,000	geosyn-chronous
$\Omega^2[(\text{rad/sec})^2 \times 10^6]$	1.541	1.228	.995	.679	.271	.091	.022	.0053

Note from Equations (48) to (50) that it is not merely sufficient to satisfy the stability conditions, but also necessary to satisfy them by some finite amount in order to achieve small angular errors under steady load. Consider, for example, the steady pitching moment due to aerodynamic drag, given by Equation (2) of Section 3.2, and also express $I_{zz} - I_{xx}$ as

$$I_{zz} - I_{xx} = C_i \cdot \frac{\pi}{4} m' D^4 \tag{51}$$

where C_i is a dimensionless coefficient and m' is the mass per unit area of the reflector. For this case the steady state pitching error is

$$\theta_o = \frac{C_m p_d}{3C_i \Omega^2 m' D} \tag{52}$$

As an example, assume the following conditions

500 Km altitude

f/D = 1.0, and a smooth reflector

Feed mass = 1/2 reflector mass

Massless feed supports.

For these conditions

$$C_m = .00277$$

$$p_d = 20\text{x}10^{-5} \ (N/m^2)$$

$$C_i = .2502$$

$$\Omega^2 = 1.288\text{x}10^{-6} \ (\text{rad/sec})^2$$

$$I_{zz}/I_{xx} = 4.98$$

so that

$$\theta_o = \frac{.573}{m'D} \ \text{(radians)} \tag{53}$$

From the range of parameters given in Table 1, m'D ranges from 1.0 to 1000, and the permitted tolerance on θ ranges from .01 to 10^{-5}. Thus, only for m'D > 57.3 is the steady state pointing error in pitch less than the maximum permitted tolerance, .01 radian. It may be concluded that, in the example considered, passive gravity gradient stabilization is adequate under some, but not all, design conditions.

For time dependent loading conditions, the mass and Coriolis damping terms derived in Appendix D must also be taken into account. Dynamic analysis of the pitch degree of freedom is easier than roll and yaw because its full dynamic equation is simply

$$(I_{zz} + I_{xx})\ddot{\theta} + 3\Omega^2 \ (I_{zz} - I_{xx}) \ \theta = M_y \tag{54}$$

If M_y is harmonically varying at frequency ω, the harmonic response θ is given by

$$\theta = \frac{\theta_o}{1 - \left(\frac{\omega}{\omega_y}\right)^2} \tag{55}$$

where θ_o is the static response to a load of magnitude M_y, and

$$\omega_y = \Omega \sqrt{\frac{3(I_{zz} - I_{xx})}{I_{zz} + I_{xx}}} \tag{56}$$

For the example cited above, $I_{zz}/I_{xx} = 4.98$, and $\omega_y = 1.413\Omega$. The amplification factor for excitation with frequency equal to the second harmonic of the orbital frequency is

$$\frac{1}{1 - \left(\frac{\omega}{\omega_y}\right)^2} = -.997 \tag{57}$$

The second harmonic of the orbital frequency is important because it is the dominant harmonic of solar radiation pressure. For example, if the orbit of the vehicle is in the ecliptic plane, then Equations (6) and (7) of Section 3.3 give the following equation for the second harmonic coefficient of pitching moment.

$$M_{\theta_2} = K_p \cdot \frac{\pi}{4} p_s D^3 \tag{58}$$

The second harmonic response to a pitching moment of this magnitude is

$$\theta_2 = \frac{K_p p_s}{3C_i \Omega^2 m'D} \cdot \frac{1}{1 - \left(\frac{\omega}{\omega_y}\right)^2} \tag{59}$$

The assumed value of p_s is $.75 \times 10^{-3}$ N/m^2, and, for a smooth reflector surface with f/D=1, $K_p = .0417$. Using the parameters for the previous example

$$\theta_2 = -\frac{0.322}{m'D} \tag{60}$$

which has the same order of magnitude as the steady state error due to aerodynamic drag at 500 Km. The response to higher harmonics is much smaller because both the harmonic content of the pitching moment and the dynamic amplification factor decay rapidly with frequency.

Nothing has been said yet about damping, and indeed no damping is available if the vehicle is rigid and no other means of control is provided. Damping is necessary because otherwise transient disturbances persist indefinitely. Sources of transient disturbance which have been discussed earlier are meteoroid impact, Section 3.4, and thermal shock due to entry and exit from the Earth's shadow, Section 3.1. The discussion of meteoroid impact quoted a very small value of damping ($g = 7.3 \times 10^{-4}$) required to contain the pointing error in a worst case analysis.

Another matter which has not yet been discussed is the effect of variations in gravity gradient due to orbit ellipticity and anomalies in the gravitational field. The principal effect of these variations is to cause the stiffness coefficient represented by $3\Omega^2$ in Equation (54) to have a small variable part consisting of harmonics of the orbital frequency. The strongest harmonic of the Earth's gravitational field is a second harmonic component in the meridional direction which is at least three orders of magnitude smaller than the steady part. Orbital ellipticity will produce gravitational variations which include odd harmonic components of the orbital frequency.

As mentioned, an important result of such anomalies is to replace the stiffness coefficient in Equation (54) by

$$K = 3\Omega^2(1 + \varepsilon_1\cos(\Omega t + \phi_1) + \varepsilon_2\cos(2\Omega t + \phi_2) + \ldots) \qquad (61)$$

If only the first perturbation term is considered, Equation (54) becomes a form of the Mathieu-Hill equation which has been studied extensively and whose stability characteristics are well known. These studies show that, if ε_1 is small, the system will be unstable if the resonant frequency given by Equation (56) lies within a small band located at all of the integer and half-integer harmonics of Ω. For example, if $\varepsilon_1 = 0.2$, then the unstable ranges of ω_y/Ω are from .48 to .53, from .99 to 1.02, etc., with increasingly narrow ranges at higher harmonics. The width of each unstable range is approximately proportional to ε_1, and since the expected values of the ε's are very small, all that is required to avoid this type of instability is to avoid nearly exact resonances with the harmonics and half-harmonics of the orbital frequency. This conclusion also holds if several non-zero values of the ε's are present simultaneously. A correlary of this conclusion is that it must be possible to compute the rigid body frequencies and some of the lower structural frequencies fairly accurately. At the higher harmonics of orbital frequency, very small amounts of internal damping are sufficient to prevent instability, even with exact resonances.

5.2 Conceptual Design of a Gravity Gradient Control System

It has been shown in the previous subsection that pointing errors can be corrected by gravity gradient stabilization, in some cases, without any explicit design modifications. This is effective for some vehicles, including the type considered in this report provided that it has a heavy feed mass. Although stability is achieved at no additional weight or cost, the pointing accuracy is not spectacular and damping of rigid body modes is not provided.

Gravity gradient stabilization and control can be improved by the deliberate addition of mechanical components to the vehicle system. Consider, for example, the design shown in Figure 2. The additional components are a small mass, called the anchor, plus a long cable and a harness consisting of three or more shorter cables which attach the long cable to the rim of the reflector.

Each of the harness cables is in series with an elastomeric damper and a winch. The winches are needed only if it is desired to exercise active control of the pointing axis.

Gravity gradient produces a tension in the long cable equal to

$$T = 3\Omega^2 m_a z_a \tag{62}$$

where m_a is the mass of the anchor (assuming that the mass of the cable is negligible), and z_a is the distance from the anchor to the center of gravity of the complete system, including reflector, feed and anchor. Thus,

$$z_a = \frac{m}{m+m_a}(\ell+\ell_a) \tag{63}$$

where m is the mass of reflector and feed.

If the reflector is pitched through a small angle, θ, the tension T will produce a moment on the reflector which resists the pitch angle. The use of this principle to reduce pointing errors is discussed in following subsections.

A lateral force at the apex of the harness cables will tend to increase the tension in some cables and to reduce the tension in others. This will cause extensional motions of the elastomeric dampers (which are assumed to be much less stiff than the cables) and, if the motions are time-dependent, damping will result. It will be shown later that both the rigid body modes and the elastic vibrations of the system are damped.

Operating the winches in a differential manner will alter the junction point of the long cable and the harness cables, thereby creating moments about the center of gravity of the reflector and feed. In this manner, the pointing axis can be deliberately altered in response to commands or to feedback from pointing error detectors.

The control system shown in Figure 2 does not resist yawing moments. Such moments are presumably small because the reflector surface is axisymmetric; also, the error tolerance for yaw is probably much larger than the tolerance for pointing error. The correction of yaw errors can be achieved by adding small masses that are connected to the rim by booms and dampers in the fore-aft directions. Note that booms rather than cables are needed because the component of gravity gradient in the fore-aft direction is very small (assumed zero in Appendix D) compared to the component in the vertical direction.

The length of the anchor cable is likely to be of the order of 100 times the diameter of the reflector. Based on previous work with long

filamentary structures, the cable should be constructed from several separated strands with frequent load interchanges in order to reduce the probability that the cable will be severed by micrometeoroids. The added weight penalty to meet this threat is estimated to be low.

5.3 Steady State Pointing Errors

Steady state pointing errors can easily be estimated for passive operation of the gravity gradient control system described in the previous section.

If the reflector is pitched through a small steady angle θ, the long cable will be translated without rotating, because the component of gravity gradient force in the fore-aft direction is negligibly small (see Equation (1) of Appendix D). As a result, the tension in the cable exerts a restoring pitching moment

$$M_y = kT\ell\theta \tag{64}$$

on the reflectors, where k is a reduction factor to account for the flexibility of the harness. For the present, the flexibility of the harness will be ignored and the reduction factor will be set equal to unity. The moment given by Equation (64) has an upper limit

$$(M_y)_{max} = kTD/2 \tag{65}$$

which occurs when $\theta = D/2\ell$. For larger angles one cable goes slack.

An additional (positive or negative) restoring moment will be provided by gravity gradient acting on the reflector itself, but this effect will be ignored because it is intended to provide a much larger restoring moment by adding the anchor and cable. As a result we may express the steady state pointing error due to aerodynamic drag by means of Equation (52) of the preceding section with the inertia coefficient C_i set equal to

$$C_i = \left(\frac{m_a}{m_r}\right)\cdot\left(\frac{z_a\ell}{D^2}\right) \tag{66}$$

where m_r is the mass of the reflector.

The resulting pitch angles are plotted in Figure 3 vs. the product $C_i m'D$ with altitude and focal ratio as parameters. The product m'D ranges from 1.0 to 1000 for the applications considered here. A practical upper limit for C_i is probably around 100, based on weight and other considerations. This is a very large increase over the value used in the preceding section (.2502) for an uncontrolled vehicle with heavy feed mass, and it extends considerably the range of mission parameters for which passive gravity gradient stabilization is practical.

The results for steady roll moment are similar to those for steady pitching moment, except that the restoring moment given by Equation (64) is multiplied by a factor which is approximately equal to $(1+\ell/4\ell_a)$. There is, however, no change in the maximum moment given by Equation (65).

The steady pitch (or roll) error can be reduced to zero by introducing active trim control through the winches shown in Figure 2. In effect, the junction point of the long cable and the harness is deflected through the angle, θ relative to the reflector, rather than deflecting the pointing axis of the reflector itself. As mentioned, the angle at which one of the harness cables goes slack is $\theta = D/2\ell$. Thus, using Equation (52),

$$\theta_{max} = \frac{D}{2\ell} = \frac{C_m P_d}{3C_i \Omega^2 m' D} \tag{67}$$

from which, using Equation (66),

$$\left(m' z_a \frac{m_a}{m_r}\right)_{min} = \frac{2C_m P_d}{3\Omega^2} \tag{68}$$

This result provides the minimum value of $m'z_a\ m_a/m_r$ required to produce a control moment equal to the aerodynamic pitching moment. The expression on the right-hand side is a function of the altitude and the focal ratio only. Equation (68) is plotted in Figure 4. As an example, if the altitude is 400 Km and f/D = 1.0, then the minimum required value of $m'z_a m_a/m_r = 1.1$. If we double this value to provide a margin of safety and select $m' = 0.01$ and $m_a/m_r = 0.02$, then the required cable length is approximately equal to

$$z_a = 2 \times 1.1/0.01 \times .02 = 11{,}000 \text{ meters} \qquad (69)$$

independent of reflector diameter.

5.4 Dynamic Response

Appendix E includes an analysis of the dynamic response in pitch of the gravity gradient control system described in Section 5.2. The topics treated in Appendix E are vibration modes, modal damping, and response to dynamic pitching moments. The major conclusions will be summarized here.

The system has two pitching modes: a low frequency mode which is nearly a rigid body mode, and a high frequency mode which mainly involves pitch of the reflector, with a small opposing motion of the anchor mass. Frequencies and mode shapes are plotted in Figures E-2 and E-3 vs. two characteristic parameters. The parameter α in these figures is directly related to the parameter C_i defined in Equation (66) by

$$\alpha = \frac{\ell_a}{\ell+\ell_a} \cdot \frac{m_r D^2}{I} \cdot C_i \qquad (70)$$

where I is the pitching moment of inertia of the reflector-feed system and m_r is the mass of the reflector. The practical range of the parameter α is from about two to about two hundred.

As mentioned in Section 5.2, damping is provided by elastomeric dampers in series with the harness cables. Appendix E includes an approximate analysis of the damping provided by the dampers to each of the modes. The damping for the higher mode is much larger than the damping for the lower mode, as shown by the results tabulated in Section E.4. It is also shown that the damping of the low frequency mode is adequate, for reasonable parameter values, because the excitation of the low frequency mode is small.

For sinusoidal excitation, the response can be expressed as an equivalent static response multiplied by a dynamic amplification factor. The dynamic amplification factor is plotted versus frequency in Figure E-4 for a typical value of α and extreme values of ℓ/ℓ_a.

As discussed in Section 5.1, the most important component of sinusoidal excitation is the second harmonic component of solar radiation pressure. Equation (59) of that section gives the second harmonic pitching response for an uncontrolled vehicle. The same equation can be applied to the passive control system under discussion by using the value of C_i given by Equation (66) of Section 5.3 and by replacing the dynamic amplification factor $(1/(1-(\omega/\omega_y)^2)$ in Equation (59) by the value derived in Section E.3. From Figure E-4, a typical value of the amplification factor for second harmonic excitation ($\omega/\Omega=2$) is 1.0. Using this value, and previously derived parameters for solar radiation pressure, produces the plots of pointing error shown in Figure 5. By comparing Figure 5 with Figure 3, it is seen that the second harmonic response to solar radiation pressure is greater than the steady state response to aerodynamic drag for altitudes greater than 600 Km.

The dynamic response of the system in roll and yaw has not been treated. The analysis is more difficult than the analysis of pitch because the roll and yaw degrees of freedom are coupled. It is expected that results similar to those for pitch will be obtained, except that the response to second harmonic excitation may be larger due to the close proximity of the rigid body roll mode to the second harmonic of orbital frequency, indicated in Figure 1 of Appendix D.

SECTION 6
ACTIVE CONTROL

The emphasis in this report has been on the physical means used to apply control moments, rather than on control laws. Active control of a gravity gradient control system was discussed briefly in Section 5.2 and, in general, it has been mentioned repeatedly that steady state pointing error could be eliminated by trim control. This subject is discussed in some detail in Appendix F, where it is shown that integral feedback (feedback which is asymtotic to a constant times $1/\omega$ as the frequency, ω, approaches zero) can entirely eliminate steady state error due to external (environmental) moments, and can generally reduce errors due to low frequency excitation.

The discussion of Appendix F is largely concerned with stability. A practical design approach is described which yields good stability and good error suppression characteristics.

SECTION 7
CONCLUDING REMARKS

Of the sources of control moment that have been reviewed, only stored angular momentum and interaction with the Earth's magnetic field appear to be inappropriate for the mission spectrum considered in this report. All of the others have some potential application, depending on altitude and vehicle parameters.

Due to the long mission duration, expelled mass using chemical propulsion results in a relatively heavy control system. Electric propulsion, on the other hand, is a strong candidate at all altitudes.

Aerodynamic pressure is a strong candidate at low altitudes and solar radiation pressure is a strong candidate at high altitudes. Gravity gradient is probably the strongest candidate, except at very low and at very high altitudes, and it is, furthermore, the only source of control moment that increases more rapidly with vehicle size than the environmental sources of overturning moment. The requirement for geotropic pointing makes gravity gradient stabilization particularly appropriate for the mission spectrum that has been studied.

An important aspect of control that has not been discussed to any extent is orbital maintenance, i.e., the application of a force at the center of gravity of the vehicle to maintain orbital altitude and ellipticity within acceptable limits. The only available sources of such a force are expelled mass and solar radiation pressure.

REFERENCES

1. MacNeal, R.H.: Structural Dynamics of the Heliogyro. NASA CR-1745, May 1971.
2. MacNeal, R.H.: Meteoroid Damage to Filamentary Structures. NASA CR-869, September 1967.
3. Robbins, W.M., Jr.: The Feasibility of an Orbiting Radio Telescope. NASA CR-792, June 1967.
4. MacNeal, R.H.: Comparison of the Solar Sail with Electric Propulsion Systems. NASA CR-1986, February 1972.
5. Wiley, C. (pseudonym: Sauders, R.). "Clipper Ships of Space," Astounding Science Fiction, May 1951, p. 135.
6. Garwin. "Solar Sailing, A Practical Method of Propulsion Within the Solar System," Jet Propulsion Laboratory, March 1958.
7. Friedman, L., et al. "Solar Sailing -- The Concept Made Realistic," AIAA 16th Aerospace Sciences Meeting, Huntsville, Alabama, January 16-18, 1978.
8. MacNeal, R.H.; Hedgepeth, J.M.; and Schuerch, H.U.: Heliogyro Solar Sailer Summary Report. NASA CR-1329, June 1969.
9. Schuerch, H.U.; and Hedgepeth, J.M.: Large Low-Frequency Orbiting Radio Telescope. NASA CR-1201, October 1968.
10. MacNeal, R.H.: The Dynamics of Rotating Elastic Bodies. MacNeal-Schwendler Corporation Report MSR-36, August 1973.

Table 1

Mission Parameters

Reflector Diameters:	100 to 1000 meters
Circular Orbits:	200 to 20,000 kilometers altitude and geosynchronous
f/D:	0.5 to 2.0
Physical Pointing Accuracy Maximum Error:	10^{-2} to 10^{-5} radians
Mass per unit area:	10^{-2} to 1 kg/m^2
Surface Solidity:	.01 to 1.0
$Mass_{feed}/Mass_{reflector}$	.01 to 1.0
Mission Duration:	10 years

Table 2

Summary of Control Moment Sources

Physical Effect	Practical Altitude range (km)	Practical size range (m)	Passive Control Possible	Active Control Practical
Expelled Mass	Any	Any	No	Yes
Inertia Wheel	Any	< 5	No	Yes
Gyrostabilizer	Any	< 5	Yes	No
Gravity Gradient	400-20,000	> 10	Yes	Yes
Aerodynamic Pressure	< 1000	Any	Yes	Yes
Solar Radiation Pressure	> 600	Any	No	Yes
Earth's Magnetic Field	400-20,000	Any	No	Yes

Table 3

Steady Restoring Moments for Various Control Systems

PHSYCIAL EFFECT	FORMULA	DEPENDENCE ON ALTITUDE
Expelled Mass	$M = \frac{k\ G\ m_e\ I_{sp}\ D}{t_m}$	None
Inertia Wheel	$M = \frac{H}{t_m}$	None
Gyrostabilizer	$M = k \frac{H^2}{m'\ D^4} \theta$	None
Gravity Gradient	$M = 3k\ \Omega^2\ m'\ D^4\ \theta$	$\Omega^2 \sim \frac{1}{R^3}$
Aerodynamic Pressure	$M = C_m \frac{\pi}{4} p_d\ D^3$	$p_d \sim e^{-kh}$
Solar Radiation Pressure	$M = k_s \frac{\pi}{4} p_s\ D^3$	None
Magnetic Field	$M = \frac{\pi}{4} D^2\ I\ B$	$B \sim \frac{1}{R^3}$

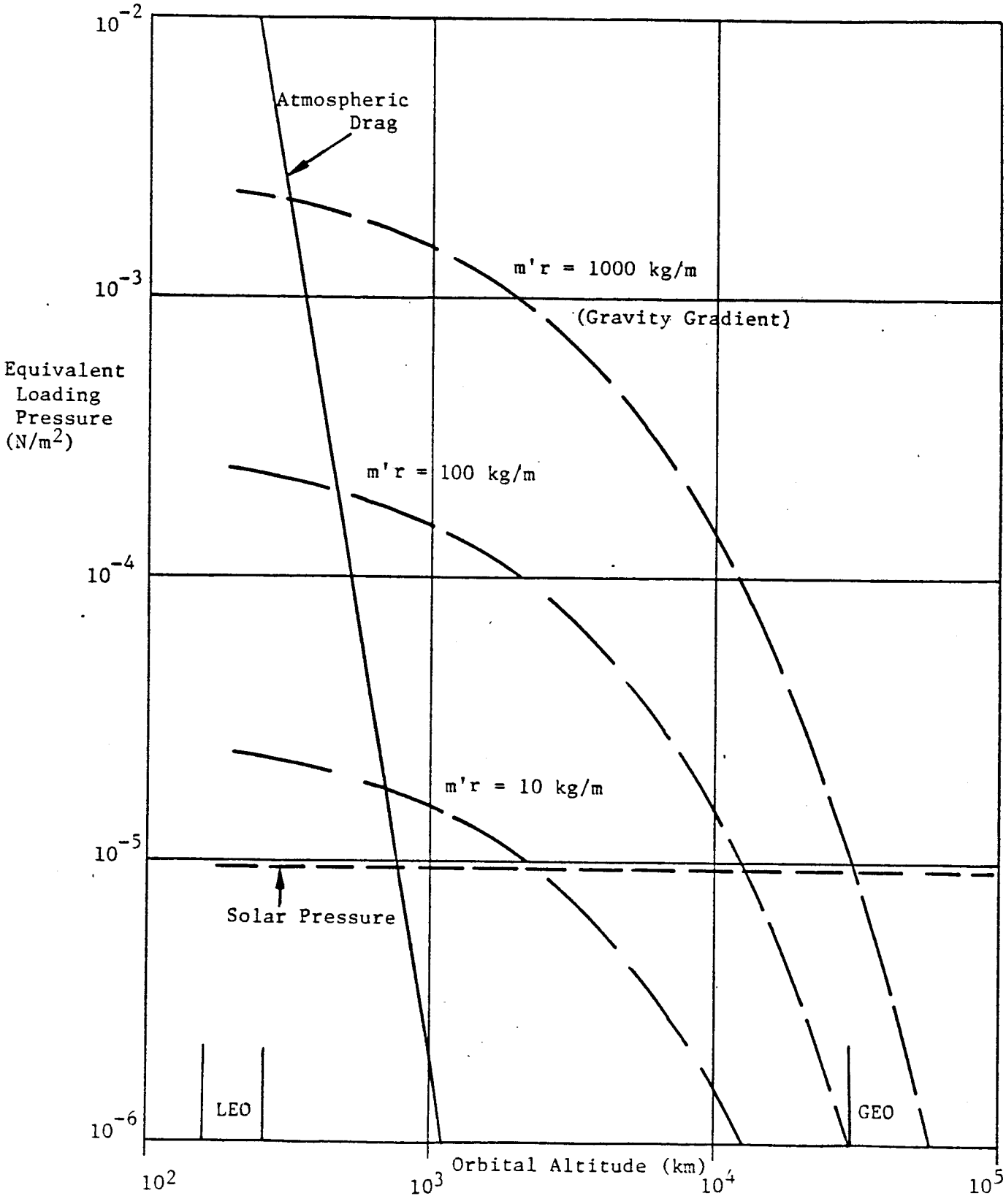


Figure 1. Equivalent Loading Pressure vs. Orbital Altitude.

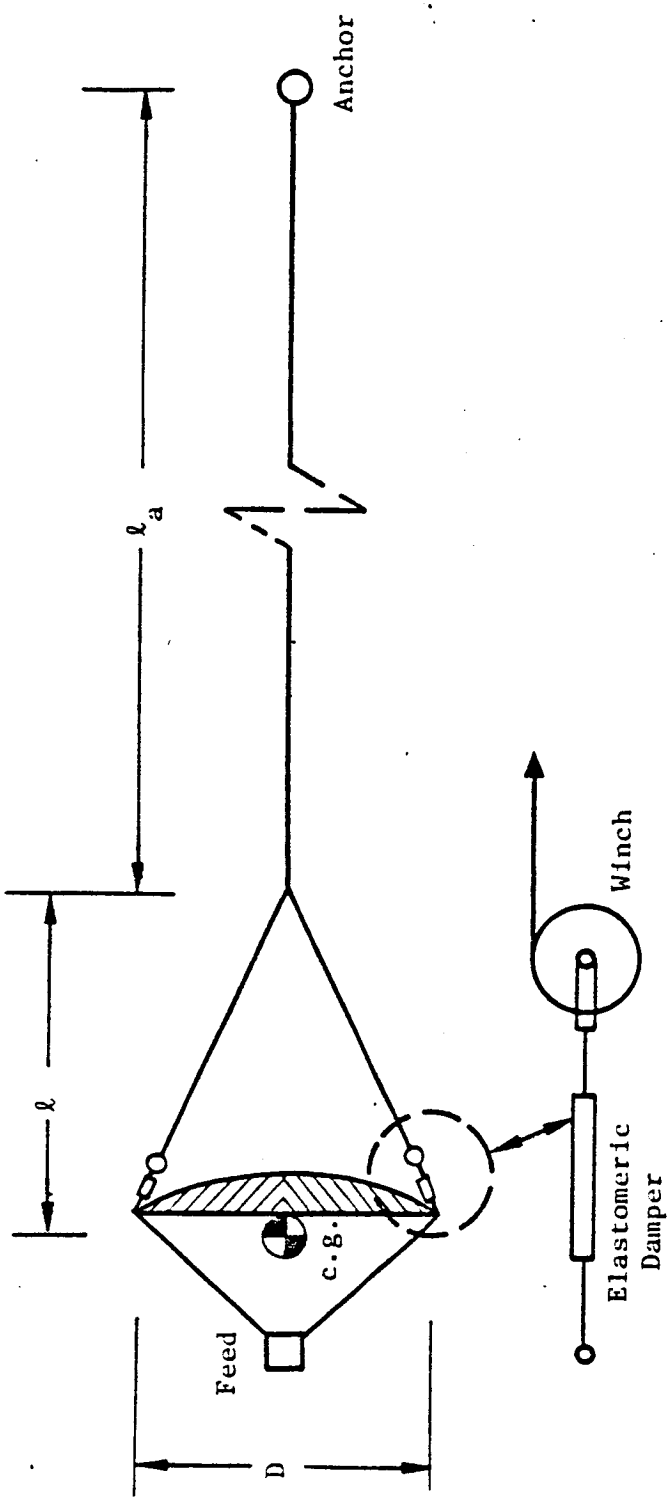


Figure 2. Gravity Gradient Control System.

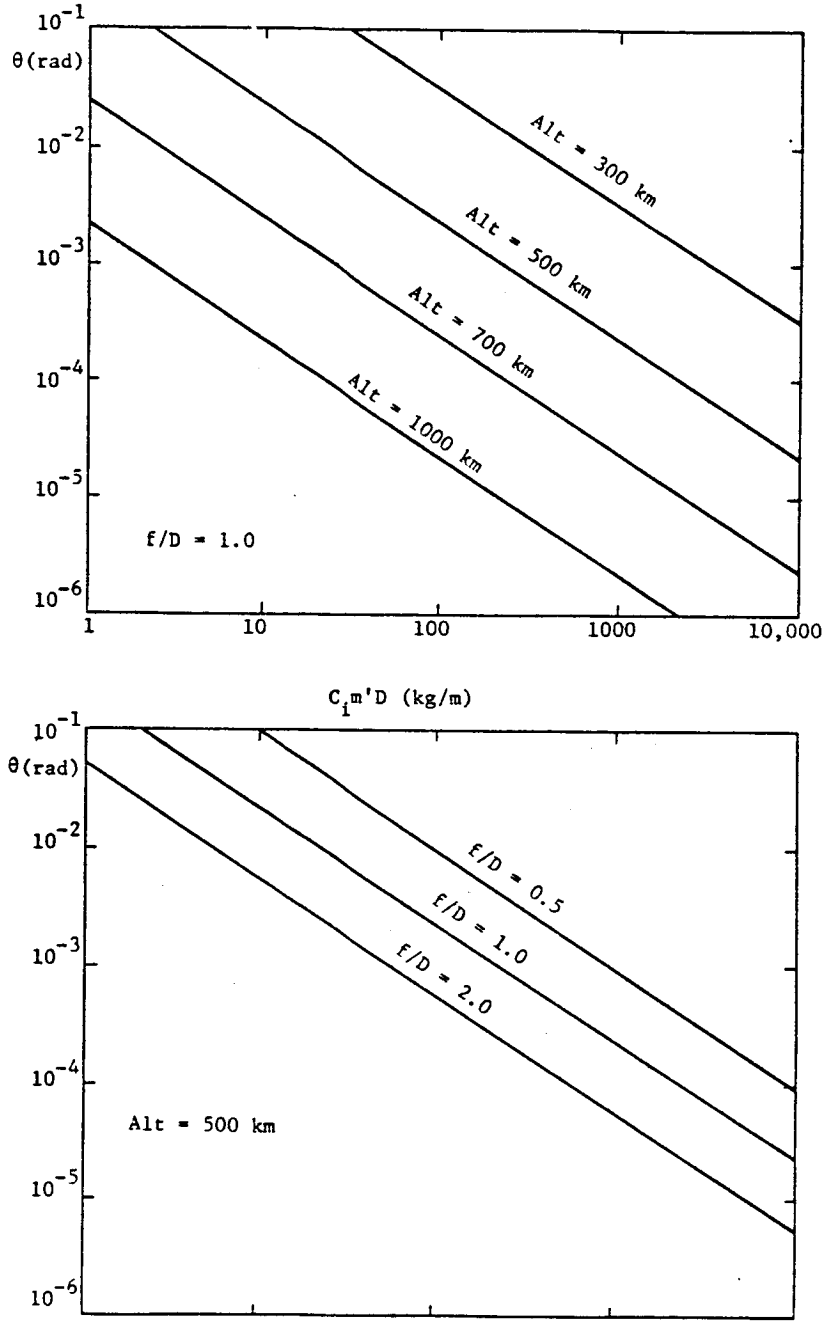


Figure 3. Steady Pitch Angle Due to Aerodynamic Drag with Gravity Gradient Stabilization.

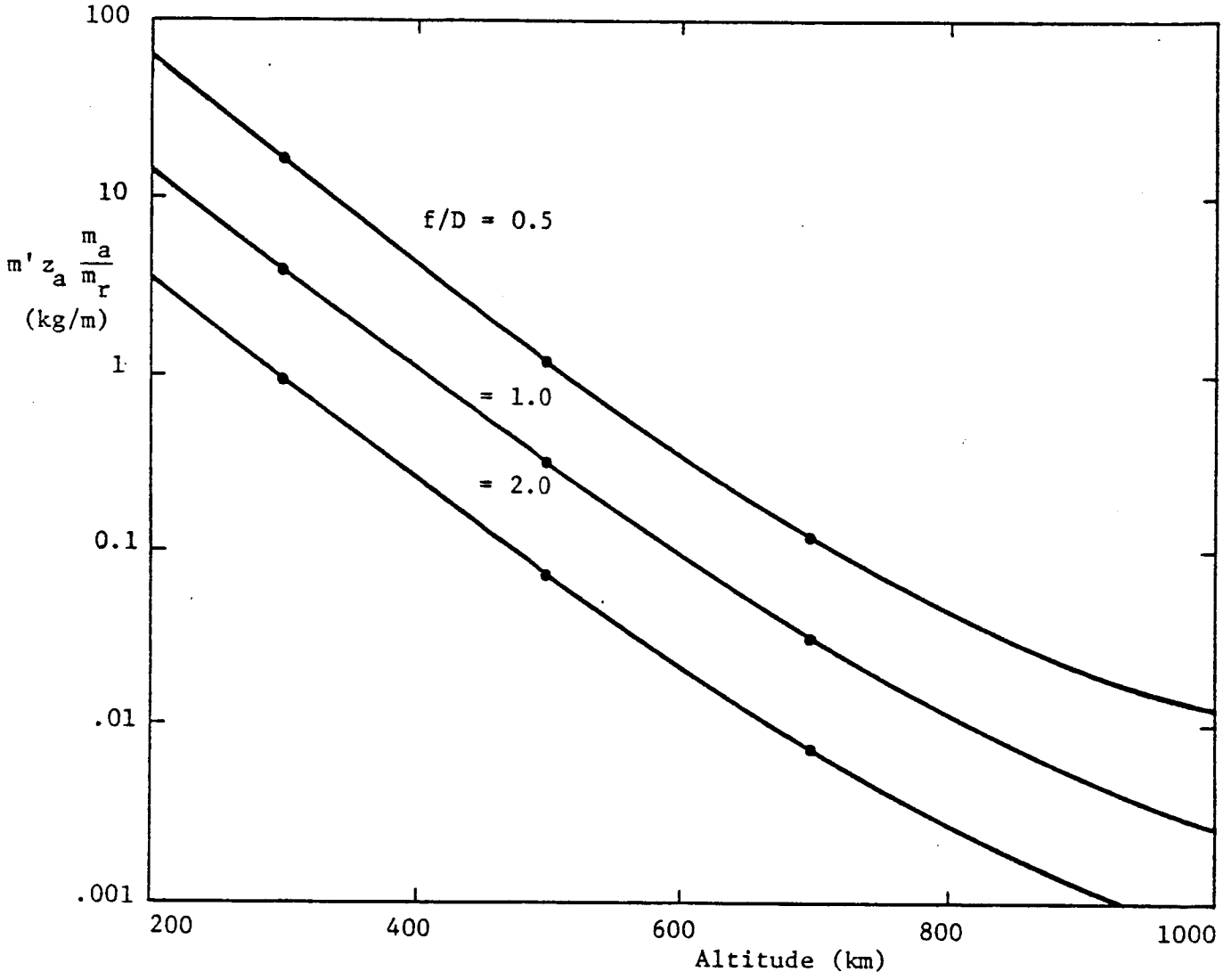


Figure 4. Minimum Value of $m' z_a \frac{m_a}{m_r}$ required to Control Steady Pitching Moment Due to Aerodynamic Drag.

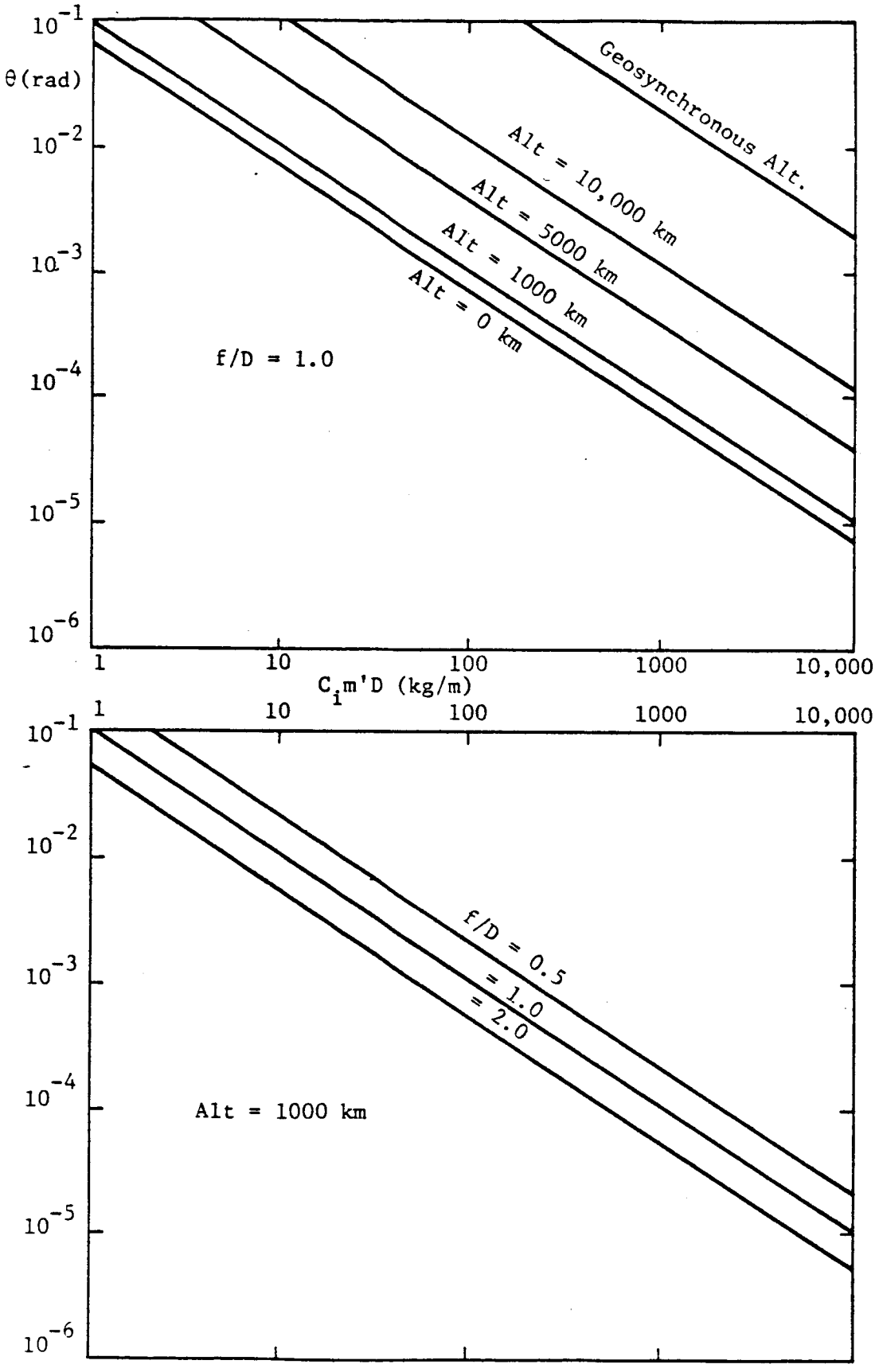


Figure 5. Second Harmonic Pitch Angle Due to Solar Radiation Pressure with Gravity Gradient Stabilization.

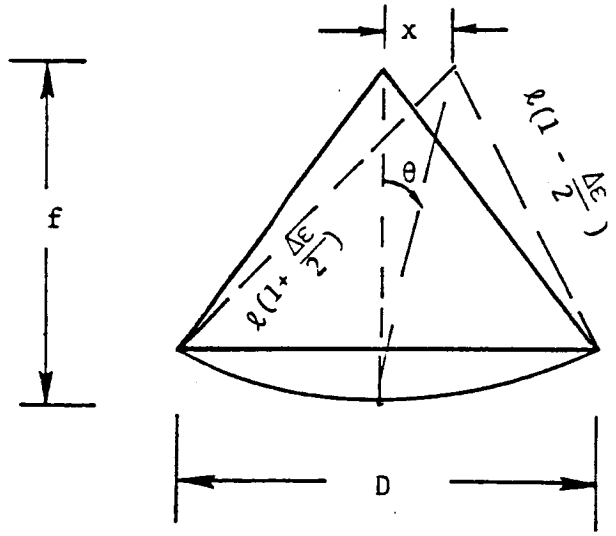
Appendix A

Effect on Pointing Error Due to Thermally Induced Length Changes in the Feed Supports

In the sketch shown below, the length of the left support is $\ell(1 + (\Delta\varepsilon/2))$ and the length of the right support is $\ell(1 - (\Delta\varepsilon/2))$ where ℓ is the undistorted length and

$$\Delta\varepsilon = \alpha\Delta T \qquad \text{(A-1)}$$

In Equation (A-1), α is the coefficient of thermal expansion and ΔT is the difference in the temperatures of the two support columns.



A simple geometrical analysis shows that, for $\varepsilon \ll 1$, the error in pointing accuracy due to differential thermal strain is

$$\theta = \frac{x}{f} = \varepsilon \cdot \left(\frac{\ell}{D}\right)^2 \cdot \frac{D}{f} \qquad \text{(A-2)}$$

ℓ/D is an easily computed function of the focal ratio f/D. The following table lists ε/θ for three values of f/D

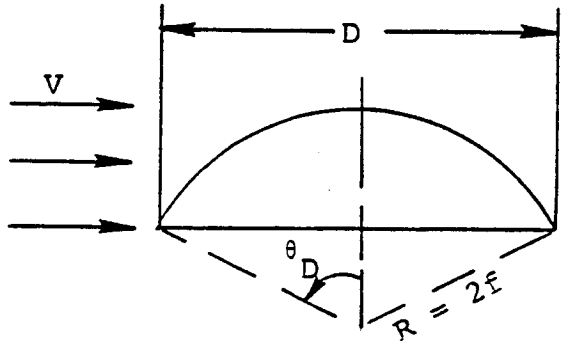
f/D	$\Delta\epsilon/\theta$
0.5	1.302
1.0	.887
2.0	.485

Thus, if the allowable error (due to this source) is 10^{-5} rad, the allowable differential strain for f/D = 1.0 is $.887 \times 10^{-5}$. Note that an increase of f/D decreases the allowable differential strain.

Appendix B

Overturning Moment Due to Aerodynamic Drag

The velocity vector is normal to the pointing axis as shown below



The reflector is assumed to be a segment of a sphere and to be smooth. According to Newtonian theory, the aerodynamic pressure is normal to the surface and proportional to $\cos^2\gamma$ where γ is the angle between the normal to the surface and the velocity vector. The component of pressure in the direction of the velocity vector is equal to $\cos\gamma$ times the normal pressure. Thus, the total drag force

$$F_d = \int p_d \cos^3 \gamma \, d S \qquad \text{(B-1)}$$

where the pressure for normal incidence, $p_d = (1/2)\rho V^2 \cdot C_N$

The value of C_N, the pressure coefficient for normal incidence, is approximately equal to 2.5. The surface integral is taken over the forward half of the reflector.

The drag per unit area of the reflector is

$$F'_d = \frac{F_d}{\frac{\pi D^2}{4}} = \frac{4}{\pi D^2} p_d \int \cos^3\gamma \, d\, S \qquad (B\text{-}2)$$

Since pressure acts normal to the surface, the resultant aerodynamic force acts at the center of the sphere and may be resolved into lift and drag components. Only the drag component contributes to the overturning moment. The moment arm for the overturning moment is the distance from the center of the sphere to the center of gravity which will conservatively be assumed equal to the radius of the sphere, 2f. Thus, the overturning moment due to drag is

$$M_d = 2f \cdot F_d \qquad (B\text{-}3)$$

and the moment coefficient is

$$C_m = \frac{4M_d}{\pi p_d D^3} = \frac{8f\, F_d}{\pi p_d D^3} = \frac{8f}{\pi D^3} \int \cos^3 \gamma \, d\, S \qquad (B\text{-}4)$$

The surface integral is evaluated as follows. In terms of angles θ and ϕ measured along the meridian and around the azimuth respectively,

$$\cos\gamma = \sin\theta\cos\phi \qquad (B\text{-}5)$$

and the surface area increment

$$d\, S = (2f)^2 \sin\theta d\theta d\phi \qquad (B\text{-}6)$$

Thus

$$\int \cos^3 \gamma \, d\, S = 4f^2 \int_0^{\theta_D} \int_{-\pi/2}^{\pi/2} \sin^4\theta\cos^3\phi d\theta d\phi \qquad (B\text{-}7)$$

$$= \frac{f^2}{6} (12\theta_D - 8\sin 2\theta_D + \sin 4\theta_D)$$

and

$$C_m = \frac{4}{3\pi}\left(\frac{f}{D}\right)^3 \cdot (12\theta_D - 8\sin 2\theta_D + \sin 4\theta_D) \qquad \text{(B-8)}$$

where

$$\sin\theta_D = \frac{D}{4f} \qquad \text{(B-9)}$$

C_m is evaluated below for three values of f/D. The drag coefficient

$$C_d = \frac{4F_d}{\pi D^2 p_d} = \frac{1}{2}\frac{D}{f} C_m \qquad \text{(B-10)}$$

is also tabulated.

f/D	C_m	C_d
0.5	.0117	.0117
1.0	.00277	.00138
2.0	.000672	.000168

The strong dependence on f/D is noted.

Appendix C

Estimation of Pointing Error Due to Micrometeoroids

A micrometeoroid which strikes the surface of the reflector will either penetrate it, or it will not. For particles which penetrate the surface, only a part of their momentum is transferred to the surface. It will be assumed that the maximum momentum transfer is equal to that of a particle which just penetrates the surface. This assumption will not cause important error because the momentum transfer for larger particles increases at a rate no greater than the diameter of the particle while the flux density decreases with about the third power of the particle diameter, for particles with masses near 10^{-9} kg.

The diameter of a particle which will just penetrate a sheet is approximately equal to one-third the thickness of the sheet (Reference 2, page 7). Thus,

$$d_p = \frac{1}{3} t_s \qquad \text{(C-1)}$$

The thickness of the sheet may be expressed as

$$t_s = \frac{m'}{\rho_s} \qquad \text{(C-2)}$$

where m' is the mass per unit area and ρ_s is the density of the material.

The mass of the particle is, using Equations (C-1) and (C-2)

$$m_p = \frac{\pi}{6} \rho_p (d_p)^3 = \frac{\pi}{6} \rho_p \left(\frac{m'}{3\rho_s}\right)^3 \qquad \text{(C-3)}$$

Assuming

ρ_p = 500 kg/m^3 (a standard assumption)

ρ_s = 2000 kg/m^3

m' = .1 kg/m^2 (the maximum range of this parameter)

then

$$t_s = 5 \times 10^{-4} \text{ m}$$

$$d_p = 1.67 \times 10^{-4} \text{ m}$$

$$m_p = 1.212 \times 10^{-9} \text{ kg}$$

The standard velocity assumed for micrometeoroids is 30 km/sec (Reference 2, page 6) so that momentum of a particle that will just penetrate the sheet is

$$m_p V_p = 1.212 \times 10^{-9} \times 30 \times 10^{3} = 3.64 \times 10^{-5} \text{ Newton-sec}$$

The magnitude of the angular momentum imparted to the vehicle by a single micrometeoroid is

$$H^{(1)} = x_i m_p V_p \cdot k_p \qquad \text{(C-4)}$$

where

x_i = moment arm of impact point

m_p = mass of particle

V_p = velocity of particle

k_p = is a factor to account for glancing impact

It is not possible to make a simple comparison between the angular impulse imparted by micrometeoroids and the moments due to other environmental effects. We can, however, estimate the maximum pointing error caused by a single impact if we make some very simple assumptions about the control system, namely that it acts like a simple spring to produce, in conjunction with the pitching inertia, I, a control frequency, ω_c. It can then be shown that the maximum angular displacement due to a single impact is

$$\theta^{(1)}_{max} = \frac{H^{(1)}}{I\omega_c} \qquad \text{(C-5)}$$

Now I can be expressed as

$$I = C_i \frac{\pi}{4} m' D^4 \qquad \text{(C-6)}$$

where C_i is a factor that depends on shape. A typical value for C_i is 0.15. Substituting from Equations (C-4) and (C-6) into Equation (C-5), and assuming $x_i = D/2\sqrt{2}$

$$\theta^{(1)}_{max} = \frac{m_p V_p k_p}{C_i \frac{\pi}{\sqrt{2}} m' D^3 \omega_c} \qquad \text{(C-7)}$$

Note immediately that, for constant ω_c, θ_{max} decreases as $1/D^3$, so that the effect is largest for small vehicles.* It has already been shown (Equation (C-3)), that m_p increases as the cube of m' so that $\theta^{(1)}_{max}$ increases as the square of m'. Using the largest value of m' (1 kg/m^2) and the smallest value of D (100 m), to be considered in the present investigation

$$\theta^{(1)}_{max} = \frac{3.6 \times 10^{-5}}{.15 \times \frac{\pi}{\sqrt{2}} \times 1 \times (100)^3 \omega_c} \qquad \text{(C-8)}$$

$$= 1.08 \times 10^{-10}/\omega_c$$

*It is shown, later on, that the effect of multiple impacts increases as the square root of the number of impacts, which value is proportional to D. Thus, for multiple impacts, θ_{max} decreases as $1/D^2$.

The number of impacts in a given time period can be estimated from the mean flux density, f_p, of particles greater than a given size and the size of the vehicle. According to current estimates, the mean flux density of particles with mass greater than 10^{-9} kg is about 10^{-7} particles per square meter per second. Thus, the rate of particles of this size intersecting a reflector with 100 m diameter is approximately

$$N'_p = \frac{\pi}{4} D^2 f_p = \frac{\pi}{4} \times (100)^2 \times 10^{-7} = .785 \times 10^{-3} \text{ particles/sec} \qquad \text{(C-9)}$$

This amounts to one impact every 21.2 minutes which is of the same order as the period of pitching oscillation.

The effects of particle impacts on pointing error are added statistically, because their directions and impact points are randomly distributed. According to statistical theory, the combined effect of N_p random impacts is equivalent to $\sqrt{N_p}$ simultaneous impacts at a point of mean radius, $D/2\sqrt{2}$. Thus, selecting x_i in Equation (C-1) to be $D/2\sqrt{2}$, and k_p to be $\sqrt{N_p}$, the equivalent angular momentum is

$$H = D\, m_p\, V_p \sqrt{N_p} \,/\, 2\sqrt{2} \qquad \text{(C-10)}$$

and the maximum pointing error is

$$\theta_{max} = \frac{H}{I\omega_c} \qquad \text{(C-11)}$$

The effect of smaller particles has not been considered in this calculation. Their effect may be estimated by assuming that the effective particle mass is

$$m_e = \sqrt{\sum m_i^2} = \left[\int_o^{m_p} m_i^2 \, d\, N_i\right]^{1/2} \qquad \text{(C-12)}$$

and that particle flux is inversely proportional to particle mass. Thus,

$$N_i = \frac{k}{m_i} \tag{C-13}$$

where

$$k = N_p \, m_p \tag{C-14}$$

so that

$$dN_i = \frac{-N_p m_p}{m_i^2} \, dm_i \tag{C-15}$$

and

$$m_e = \left(N_p \, m_p^2\right)^{1/2} = m_p \sqrt{N_p} \tag{C-16}$$

Thus, the net effect of smaller particles is just equal to the net effect of larger particles. Their effect is included by doubling the value of H in Equation (C-10).

It remains to select an appropriate time period to use in computing N_p. If the control system has no damping, then the appropriate time is the useful life of the vehicle (assumed to be 10 years). In this case

$$N_p = N'_p \cdot t = .785 \times 10^{-3} \times 3.15 \times 10^{8} = 2.47 \times 10^{5} \tag{C-17}$$

$$2\sqrt{N_p} = 994.0$$

and

$$\theta_{max} = 994 \times \theta_{max}^{(1)} = 994 \times 1.08 \times 10^{-10}/\omega_c = 1.07 \times 10^{-7}/\omega_c \tag{C-18}$$

The smallest control frequency, ω_c, that can be considered to be practical is the orbital frequency which is about 10^{-3} rad/sec for altitudes up to 1000 km. Thus

$$\theta_{max} = 1.07 \times 10^{-7}/10^{-3} = 1.07 \times 10^{-4} \text{ radian}$$

which is larger than the smallest allowable pointing error (10^{-5} radian) given in Table 1.

This result shows that the vehicle pitch mode should be damped if all the worst case assumptions are correct. If it is damped, the appropriate time period to use in computing N_p is the time constant of the damped oscillations which is

$$t = \frac{2}{\omega_c g} \tag{C-19}$$

where $g = 2c/c_c = 1/Q$ is the damping coefficient. For this case, assuming $\omega_c = 10^{-3}$ rad/sec,

$$N_p = N'_p \cdot t = .785 \times 10^{-3} \times 2/10^{-3}\ g = 1.57/g \tag{C-20}$$

and

$$\theta_{max} = 2\sqrt{N_p} \cdot \theta^{(1)}_{max} = 2\sqrt{\frac{1.57}{g}} \times 1.08 \times 10^{-7} = \frac{2.7 \times 10^{-7}}{\sqrt{g}} \tag{C-21}$$

The amount of damping required to reduce θ_{max} to the minimum allowable value is

$$g = \left(\frac{2.7 \times 10^{-7}}{10^{-5}}\right)^2 = 7.29 \times 10^{-4} \tag{C-22}$$

which is a very small amount.

Appendix D

Complete Small Motion Equations for the Rotations of a Rigid Body in Circular Orbit

The equations of motion will be written with reference to a vehicle coordinate system whose origin is at the center of gravity of the vehicle and whose axes are right-handed and oriented as follows:

x axis: pointing forward (in the orbital direction)

y axis: pointing to the right (as sensed by an observer standing on the Earth, directly under the vehicle and looking forward)

z axis: pointing down (toward the center of the Earth)

The rotations about these axes are (using the right-hand rule)

About x-axis: ϕ (roll)

About y-axis: θ (pitch)

About z-axis: ψ (yaw)

The equations of motion are derived by adding the effect of gravity gradient to the complete dynamic equations of a rigid body rotating about the negative y-axis with constant angular velocity, Ω (the orbital frequency in rad/sec).

The steady inertia force density vector, including both gravity gradient and centrifugal force terms, is

$$\begin{Bmatrix} f_x \\ f_y \\ f_z \end{Bmatrix} = \rho\Omega^2 \begin{Bmatrix} \dfrac{x}{1 + R/z} \\ -y \\ 3z \end{Bmatrix} \qquad \text{(D-1)}$$

where R = distance from the center of gravity to the center of the Earth. The force component, f_x, is extremely small and will be neglected.

The complete equations of motion for pitch, roll and yaw may be written in the form

$$[I\,p^2 + Bp + K] \begin{Bmatrix} \phi \\ \theta \\ \psi \end{Bmatrix} = \begin{Bmatrix} M_x \\ M_y \\ M_z \end{Bmatrix} \tag{D-2}$$

where $p = d/dt$ and

$$[I] = \begin{bmatrix} I_{yy} + I_{zz} & -I_{xy} & -I_{xz} \\ -I_{xy} & I_{xx} + I_{zz} & -I_{yz} \\ -I_{xz} & -I_{yz} & I_{xx} + I_{yy} \end{bmatrix} \tag{D-3}$$

$$[B] = 2\Omega \begin{bmatrix} 0 & I_{yz} & -I_{yy} \\ -I_{yz} & 0 & I_{xy} \\ I_{yy} & -I_{xy} & 0 \end{bmatrix} \tag{D-4}$$

$$[K] = \Omega^2 \begin{bmatrix} 4(I_{zz} - I_{yy}) & 3I_{xy} & -4I_{xz} \\ 3I_{xy} & 3(I_{zz} - I_{xx}) & 3I_{yz} \\ -4I_{xz} & 3I_{yz} & I_{xx} - I_{yy} \end{bmatrix} \tag{D-5}$$

$$\begin{Bmatrix} M_x \\ M_y \\ M_z \end{Bmatrix} = \Omega^2 \begin{Bmatrix} -4I_{yz} \\ 3I_{xz} \\ I_{xy} \end{Bmatrix} + \begin{pmatrix} \text{Terms due to other} \\ \text{environmental effects} \end{pmatrix} \tag{D-6}$$

and where the inertia integrals

$$I_{ab} = \int_v \rho abdv \quad , \quad a, b = x, y, z \tag{D-7}$$

This definition does not conform to standard definitions of moments and products of inertia which are, unfortunately, not well suited for representing the Coriolis damping matrix.

The inertia matrix [I] and the Coriolis damping matrix [B] are taken directly from Reference 4 with an appropriate transformation of axes. The stiffness matrix [k] has been derived from Equation (D-1) using the method of Reference 4.

If the principal axes of the body are aligned with the coordinate axes, it is seen from Equations (D-3), (D-4) and (D-5) that the pitch degree of freedom is uncoupled, and that the roll and yaw degrees of freedom are coupled by the Coriolis damping terms, $\pm 2\Omega I_{yy} p$.

The equation for uncoupled pitching oscillations is

$$\omega = \Omega \left(\frac{3(I_{zz} - I_{xx})}{I_{zz} + I_{xx}} \right)^{1/2} \tag{D-8}$$

from which it is seen that $I_{zz} > I_{xx}$ is a condition of stability.

The coupled rolling and yawing frequencies are obtained by the solution of

$$\begin{aligned} &\omega^4 (I_{xx}+I_{yy})(I_{zz}+I_{yy}) \\ &- \omega^2 \Omega^2 \left[4(I_{xx}+I_{yy})(I_{zz}-I_{yy}) + (I_{zz}+I_{yy})(I_{xx}-I_{yy}) + 4I_{yy}^2 \right] \\ &+ 4\Omega^4 (I_{zz}-I_{yy})(I_{xx}-I_{yy}) = 0 \end{aligned} \tag{D-9}$$

The pitching, rolling, and yawing frequencies are plotted in Figure D-1 as functions of I_{zz}/I_{xx} and I_{xx}/I_{yy}. It is seen from Figure D-1 that the conditions for stability ($\omega^2 > 0$) are:

$$I_{zz} > I_{xx} > I_{yy} \tag{D-10}$$

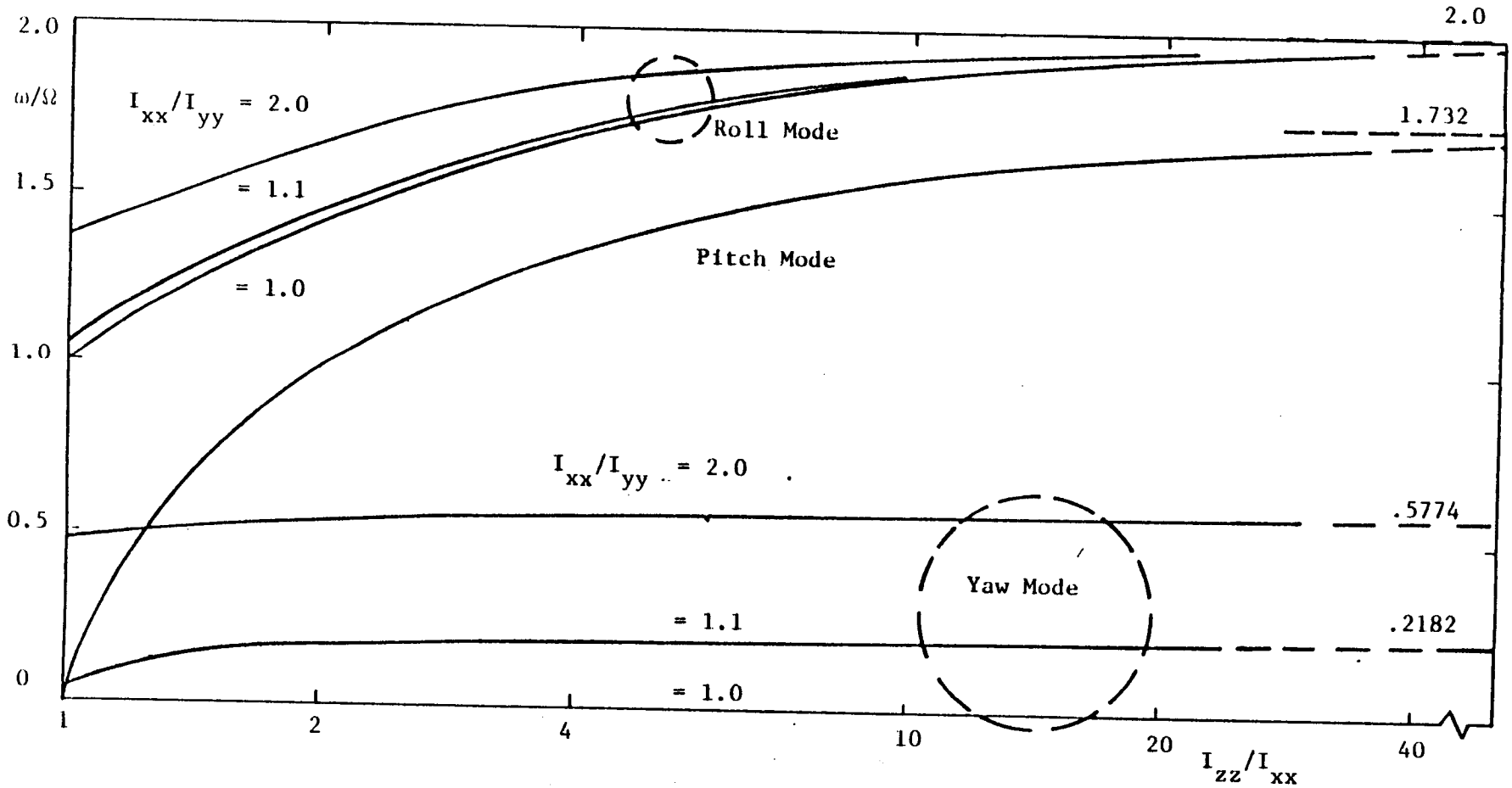


Figure D-1. Rigid Body Modes in Geocentric Orbit

Stability Requirement: $I_{zz} \geq I_{xx} \geq I_{yy}$

Appendix E

Dynamic Analysis of the Pitching Moments of a Passive Gravity Gradient Control System

Figure E-1 shows the dynamic degrees of freedom of the vehicle in the pitch plane. All of the cables are assumed to be massless and inextensional. The reflector-feed system is assumed to be rigid. The analysis consists of the following parts:

1. Derive the equations of motion, for small motions
2. Calculate vibration modes
3. Calculate response to sinusoidal pitching moment
4. Estimate modal damping due to elastomeric dampers

E.1 Equations of Motion

Referring to Figure E-1, the kinetic energy of the system is

$$E_k = \frac{1}{2}\left[m(\dot{w})^2 + m_a(\dot{w}_a)^2 + I(\dot{\theta})^2\right] \qquad \text{(E-1)}$$

where m = mass of reflector-feed system

m_a = mass of anchor

I = inertia in pitch of reflector-feed system.

The potential energy of the system is, for small motions,

$$E_p = \frac{1}{2} T \left(\ell\, \theta^2 + \ell_a\, \theta_a^2\right) \qquad \text{(E-2)}$$

where T is the tension in the long cable, given by Equations (62) and (63) in the main text. Note that the static restoring moment due to

gravity gradient acting directly on the reflector-feed system is neglected, as explained in Section 5.3 of the main text.

The translational degrees of freedom, w and w_a, can be eliminated by using the conservation of momentum

$$mw + m_a w_a = 0 \tag{E-3}$$

and the kinematic relationship

$$w = w_a + \ell\theta + \ell_a\theta_a \tag{E-4}$$

After eliminating w and w_a from Equation (E-1), a straightforward application of Lagrange's equations yields the following equations of motions.

$$\left[\begin{array}{c|c} (I + \bar{m}\ell^2)p^2 + T\ell & \bar{m}\ell\ell_a p^2 \\ \hline \bar{m}\ell\ell_a p^2 & \bar{m}\ell_a^2 p^2 + T\ell_a \end{array}\right] \left\{\begin{array}{c} \theta \\ \hline \theta_a \end{array}\right\} = \left\{\begin{array}{c} m_y \\ \hline 0 \end{array}\right\} \tag{E-5}$$

where $p = d/dt$ and $\bar{m} = mm_a/(m+m_a)$.

E.2 Calculation of Vibration Modes

It will be noted that the determinant of Equation (E-5) is quadratic in p^2. Thus, the calculation of the frequencies of free vibration requires the solution of a quadratic equation in the variable $p^2 = -\omega^2$. The frequencies are expressed by the result

$$\left(\frac{\omega}{\Omega}\right)^2 = \frac{3\beta}{2}\left[1 + \alpha\beta \pm \sqrt{(1+\alpha\beta)^2 - 4\alpha}\right] \qquad \text{(E-6)}$$

where

Ω = orbital frequency

$\alpha = \bar{m}\ell\ell_a/I$

$\beta = 1+\ell/\ell_a$

The frequency ratio, ω/Ω, is plotted vs. α and $\ell/\ell_a = \beta-1$, in Figure E-2. For $\alpha > 1$, which is the range of interest, the lower of the two frequencies corresponds closely to rigid body motion with an asymtotic frequency limit, $\omega/\Omega = \sqrt{3}$, for $\beta = 1.0$. For $\alpha > 1$, the higher of the two frequencies represents a pitching mode of the reflector, with little rotation of the long cable.

The relative mode shapes, obtained by solving the bottom half of Equation (E-5) for θ_a/θ are given by

$$\frac{\theta_a}{\theta} = \frac{\beta - 1}{3\beta(\Omega/\omega)^2 - 1} \qquad \text{(E-7)}$$

where ω is either of the frequencies given by Equation (E-6). The relative mode shapes are plotted vs. α in Figure E-3 for $\ell/\ell_a = 0.1$ and $\ell/\ell_a = 0.5$.

E.3 Response to Sinusoidal Pitching Moment

The response to sinusoidal pitching moment may be obtained by solving Equation (E-5) with $p = i\omega$, where ω is the frequency. The resulting pitch of the reflector may be expressed as follows in terms of the parameters α, β, and Ω.

$$\theta = \theta_o \left[1 - \left(\frac{1-\alpha+\alpha\beta}{3\alpha\beta} \right) \left(\frac{\omega}{\Omega} \right)^2 - \left(\frac{\beta-1}{9\beta^2} \right) \frac{(\omega/\Omega)^4}{\left(1 - \frac{1}{3\beta} (\omega/\Omega)^2\right)} \right]^{-1} \qquad \text{(E-8)}$$

where $\theta_o = M_y/T\ell$, is the static response. The bracketed expression is a dynamic amplification factor. It is plotted vs. ω/Ω in Figure E-4 for a typical value of α and extreme values of β. It is seen in Figure E-4 that the low frequency mode has a narrow peak while the high frequency mode has a broader peak.

Another way to calculate sinusoidal response of the reflector is to first compute the response of each of the modes and then to combine the modal responses. The following equation describes the general procedure

$$u_j = \sum_i \sum_k \frac{\phi_{ji}\, \phi_{ki}\, F_k}{m_i\, (\omega_i^2 - \omega^2)} \qquad \text{(E-9)}$$

where

F_k = exciting force on k^{th} degree of freedom

m_i = generalized mass of i^{th} mode

ω_i = frequency of i^{th} mode

u_j = displacement of j^{th} degree of freedom

ϕ_{ji} = displacement of u_j in i^{th} mode

ϕ_{ki} = displacement of u_k in i^{th} mode

For our particular case, the exciting force is a pitching moment on the reflector, and there are only two modes. For this case, Equation (E-1) can be expressed in the following particular form

$$\theta = \frac{M_y}{I\omega^2} \sum_{i=1,2} \frac{P_i}{(\omega_i/\omega)^2 - 1} \qquad \text{(E-10)}$$

where the "modal participation factor", P_i is

$$P_i = \frac{1}{1 + \alpha\,[\ell/\ell_a + (\ell_a/\ell)(\theta_a/\theta)^2]} \qquad \text{(E-11)}$$

The following table records P_i for $\alpha = 10$ and two values of ℓ/ℓ_a

ℓ/ℓ_a	0.1	0.5
P_1	.0012	.043
P_2	.2907	.085

Note that an important effect of increasing ℓ/ℓ_a is to greatly increase the contribution of the first mode (the rigid body mode) to the response of the reflector.

E.4 Estimate of Modal Damping and Response to Random Excitation

The elastomeric dampers are in series with the harness cables. An elastomeric damper has the property that the force in the damper is out of phase with the motion but is nearly independent of frequency (for frequencies below 10 Hz.). Therefore, the force-displacement relationship for sinusoidal motions can be represented by

$$F = k(1+ig) \cdot u \tag{E-12}$$

The per-unit critical damping of a system consisting of the damper and a mass is $C/C_{cr} = g/2$.

If the damper is very stiff compared to other elements in the system and if g is small, then the modal damping due to the damper can be estimated from

$$\left(\frac{C}{C_{cr}}\right)_{modal} = \frac{g}{2} \cdot \frac{\Delta E_p}{E_p} \tag{E-13}$$

where E_p is the potential energy in the mode due to all stiffness elements, and ΔE_p is the potential energy in the damper

$$\Delta E_p = \frac{F^2}{2k} = \frac{1}{2} k u^2 \tag{E-14}$$

If the damper is very stiff, then the force in the damper is not affected by the presence of the damper. Thus, in order to estimate the modal damping, it is only necessary to compute the force in the damper and the total potential energy from the undisturbed mode shape.

For our case, the moment resisted by the dampers is the moment acting on the reflector

$$M = \omega^2 I \theta \tag{E-15}$$

so that the potential energy in the dampers is

$$\Delta E_p = \frac{M^2}{2k_d} = \frac{\omega^4 I \theta^2}{2k_d} \qquad \text{(E-16)}$$

where k_d is the rotational stiffness of the dampers acting together to resist applied moment. Equation (E-2) gives the potential energy of the undisturbed system. Thus, using Equation (E-2),

$$\left(\frac{C}{C_{cr}}\right)_{modal} = \frac{g\,\omega^4 I}{2k_d T\ell(1 + (\ell_a/\ell)(\theta_a/\theta)^2)} \qquad \text{(E-17)}$$

where the parameters ω and θ_a/θ are the frequency and amplitude ratio for a particular mode.

This result can be expressed as follows in terms of the parameters α, β, Ω, and the ratio, θ_a/θ, given by Equation (E-7)

$$\left(\frac{C}{C_{cr}}\right)_{modal} = \frac{g}{2}\left(\frac{T\ell}{k_d}\right)\cdot \left[\frac{(\omega/\Omega)^4}{9\alpha^2\beta^2\,(1 + (1/\beta - 1)(\theta_a/\theta)^2)}\right] \qquad \text{(E-18)}$$

$$= \frac{g}{2}\left(\frac{T\ell}{k_d}\right)\cdot A_d$$

The following table records values of the bracketed expressed, A_d, referred to as the "damping amplification factor", for several values of α and ℓ/ℓ_a.

α	3	3	10	10	10
ℓ/ℓ_a	.01	.10	.01	.10	.50
Mode	Damping Amplification Factor, A_d				
1st	.00234	.01422	.00012	.00088	.00155
2nd	1.0072	1.085	1.020	1.10	1.513

It will be noted that the damping amplification factor for the 2nd mode is high in all cases and that the damping amplification factor for the first (rigid body) mode is low in all cases. Since the response to random excitation is inversely proportion to the square root of the damping, the above table would indicate that the response of the rigid body mode to random excitation would greatly exceed that of the 2nd mode. However, as indicated in Section E.3, the modal participation factor for the rigid body mode in the response of the reflector is much smaller, in most cases, than the modal participation factor for the 2nd mode. The ratio of the modal participation factor to the square root of the damping amplification factor is a good measure of the contribution of each mode to random oscillations of the reflectors. This ratio is recorded below for $\alpha = 10$, and two values of ℓ/ℓ_a.

ℓ/ℓ_a	0.1	0.5
	$C_i/\sqrt{A_{d_i}}$	
1st mode	.0405	1.092
2nd mode	.277	.069

From the data in this table, it appears that a value of ℓ/ℓ_a somewhere between 0.1 and 0.5 would minimize reflector response to random excitation.

It should also be pointed out that the elastomeric dampers will also damp the vibration modes of the cables. This matter is discussed in Reference 1.

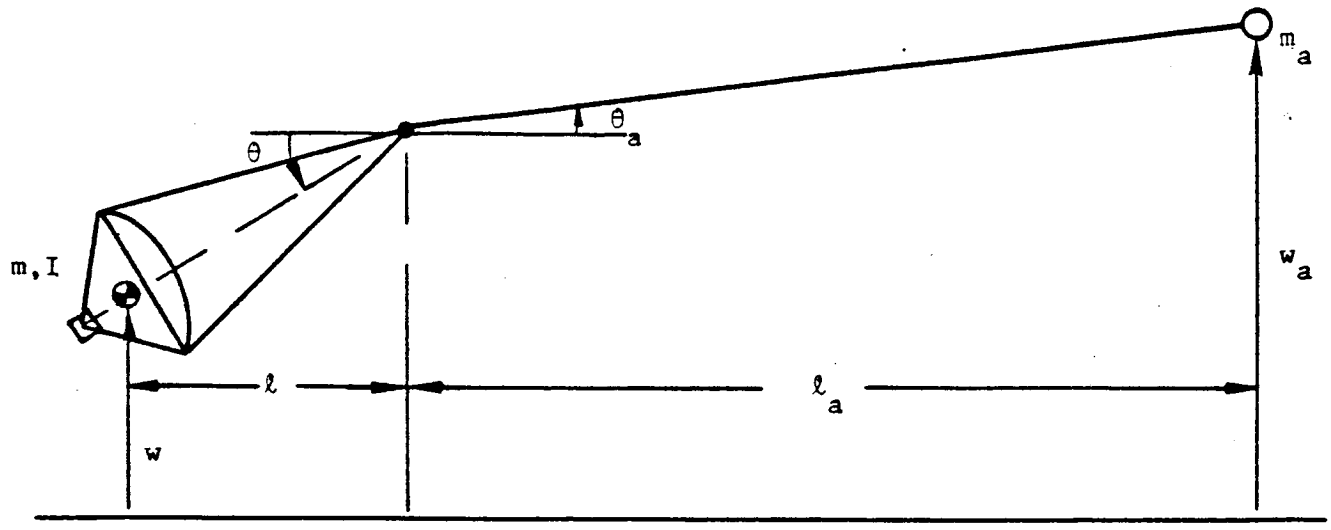


Figure E-1. Motions of System in Pitch Plane.

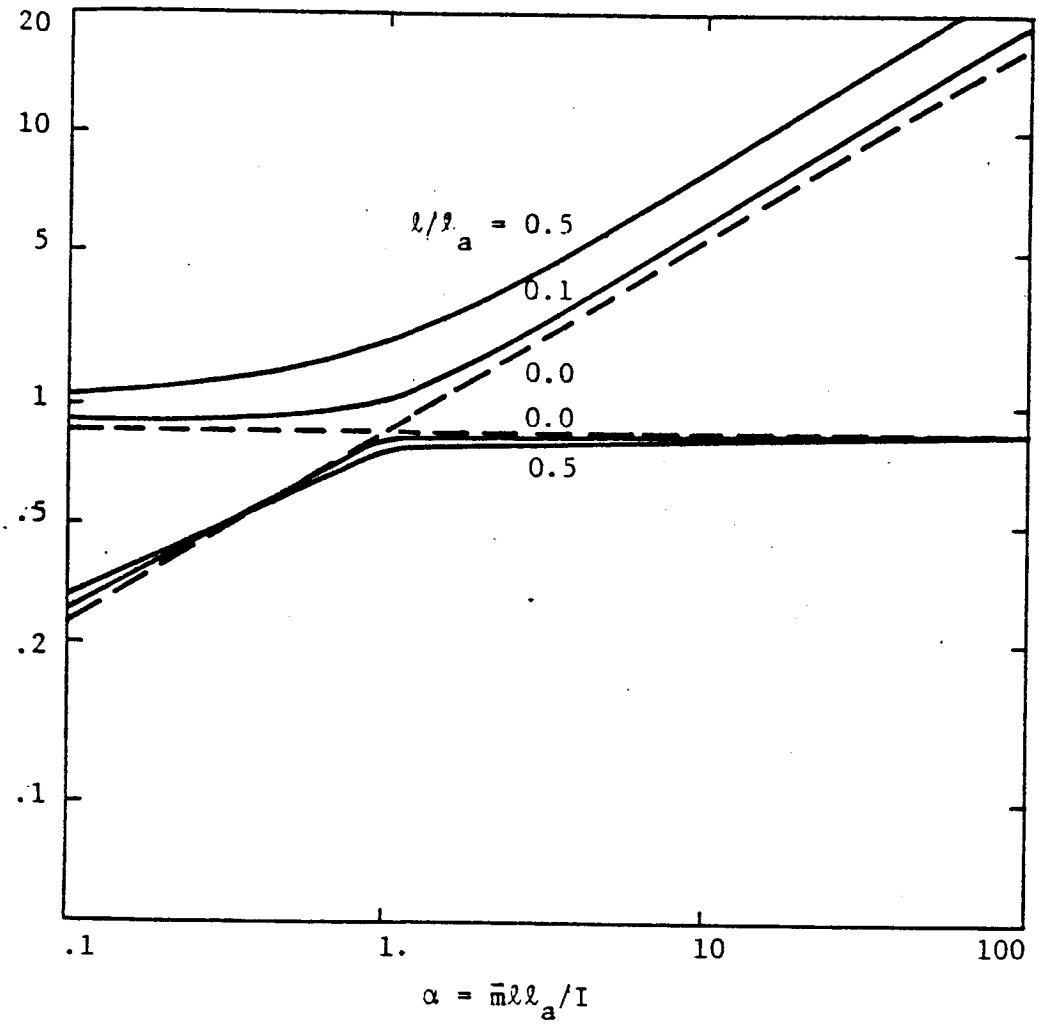


Figure E-2. Pitch Vibration Frequencies of Gravity Gradient Stabilized System.

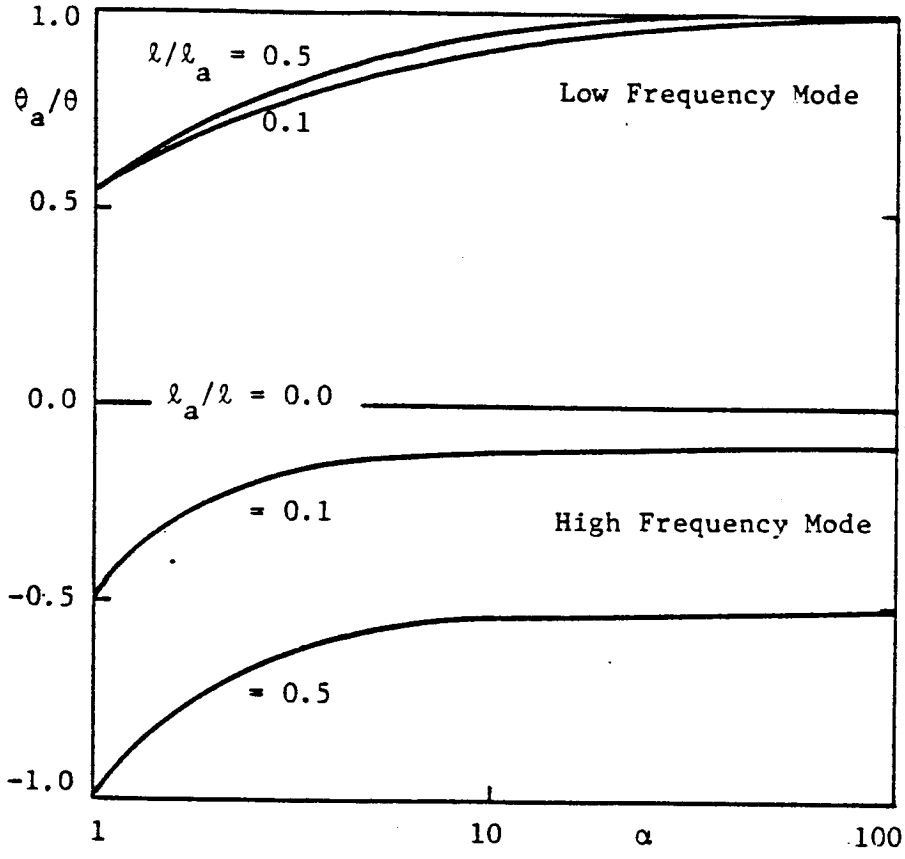


Figure E-3. Relative Modal Displacements.

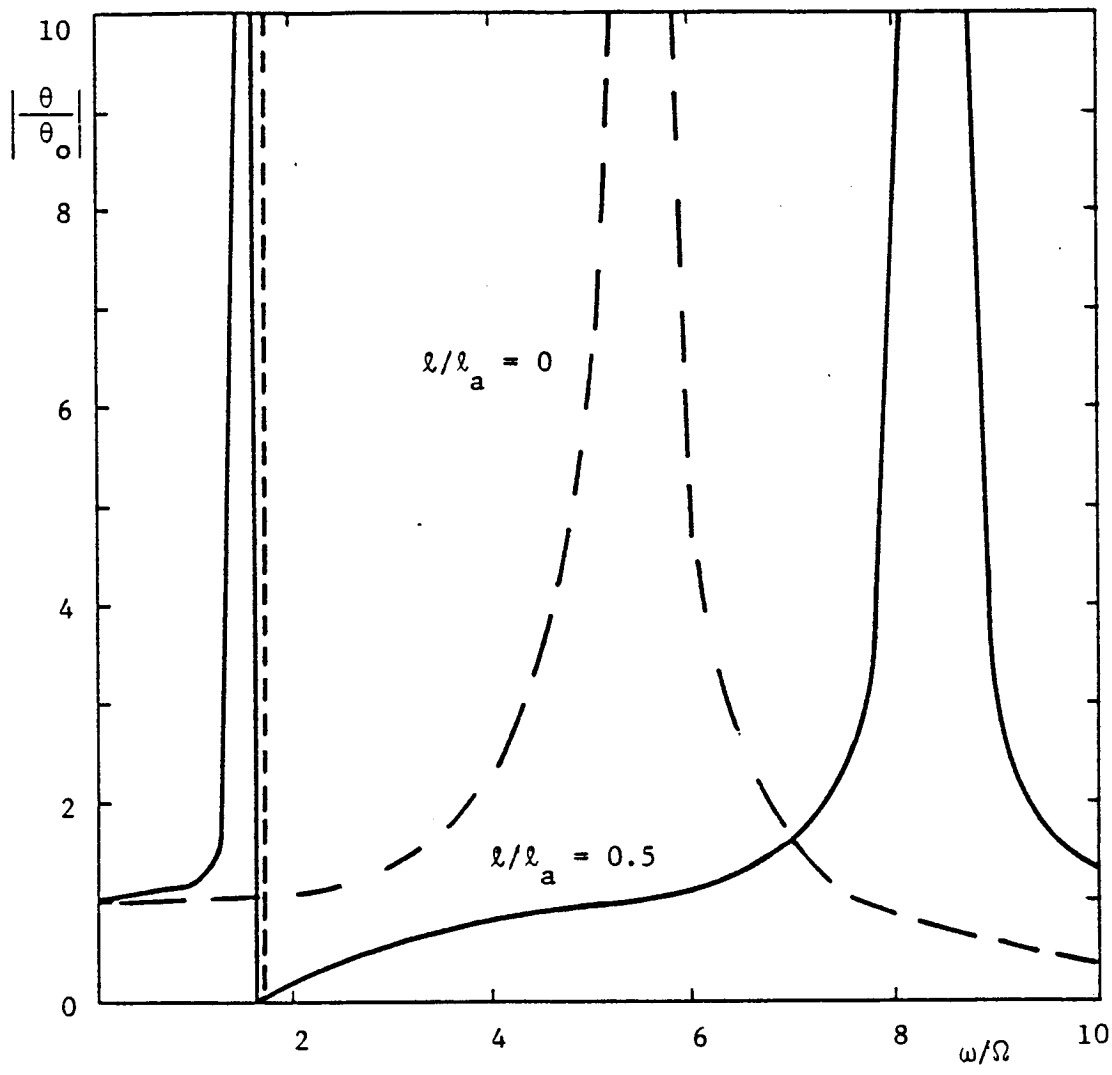


Figure E-4. Dynamic Amplification Factor for $\alpha = 10$.

Appendix F

Elimination of Steady-State Error by Integral Feedback

In aircraft, steady-state pointing error is eliminated by trim control, which can be regarded as a very low frequency control system, often with the pilot in the control loop. The subject of low frequency control is investigated in this Appendix from the viewpoint of control system theory.

Figure F-1 shows a conventional block diagram for a control system interacting with a rigid body, whose rotational inertia is I. In Figure F-1, δ_i is an input command, and M is an external (environmental) moment applied to the rigid body. For no input command, it is easily shown that the pointing error is

$$\varepsilon = \frac{M}{I\,p^2 + F(p)} \qquad \text{(F-1)}$$

wherein p may either be regarded as frequency ($p = i\omega$) or as a derivative operator. In order to achieve zero error as $p \to 0$, it is clear that the feedback F(p) must be asymtotic to A/p^n where A and n are constants and $n > 0$. In discrete systems, n is an integer and F(p) is the ratio of two polynomials, $F(p) = G(p)/H(p)$. The control system design problem is to select F(p) so that ε is smaller than a desired upper limit which may be a function of frequency, and such that the system is stable.

Stability is determined by examining the roots of

$$I\,p^2 \cdot H(p) + G(p) = 0 \qquad \text{(F-2)}$$

Elementary analysis shows that the simple forms

$$F(p) = A/p$$

and

$$F(p) = A(p+p_o)/p \qquad \text{(F-3)}$$

produce unstable roots.* The simplest form that will produce stable roots is

$$F(p) = \frac{A(p^2 + \omega_o g p + \omega_o^2)}{p} \qquad \text{(F-4)}$$

where A, ω_o, and g are constants. The asymtotic form of the error for $p \to 0$ is

$$\varepsilon \to \frac{Mp}{A\omega_o^2} \qquad \text{(F-5)}$$

which indicates the desirability of a large steady state gain, $A\omega_o^2$. The maximum error occurs near $p = i\omega_o$ and has a magnitude $\varepsilon = M/A\omega_o g$.

The stability equation for this case is

$$I\,p^3 + A\,p^2 + A\omega_o g p + A\omega_o^2 = 0 \qquad \text{(F-6)}$$

and the conditions for stability (roots with negative real parts) are that A and $\omega_o g$ be positive and that

$$A > \frac{I\omega_o}{g} \qquad \text{(F-7)}$$

*For the reason that the coefficients of p and p^2 must be positive (not merely zero) for a cubic equation to have all stable roots.

Equation (F-7) indicates a lower limit for the gain, A. An upper limit is provided by the requirement that the system be stable in the presence of structural vibration modes. In order to include such modes, the impedance of the structure $Z = 1/Ip^2$ is replaced by

$$Z = \frac{1}{Ip^2} + \sum_i \frac{1}{I_i(p^2 + g_i\omega_i p + \omega_i^2)} \qquad \text{(F-8)}$$

where I_i, ω_i, and g_i are respectively the generalized mass, frequency, and damping of the i^{th} mode. The loop gain of the system is

$$L = F(p)/Z \qquad \text{(F-9)}$$

Assuming small structural damping, the loop gain will have peaks at the modal frequencies, ω_i. If $\omega_i \gg \omega_o$ then, from Equation (F-4), $F(i\omega_i) \simeq iA\omega_i$ near a structural peak and the i^{th} peak in the loop gain has the approximate magnitude

$$L(\omega_i) = \frac{A}{I_i g_i \omega_i} \qquad \text{(F-10)}$$

In order to provide gain stability relative to every structural mode, it is required that $L(\omega_i) < 1$, or

$$A < I_i g_i \omega_i \qquad \text{(F-11)}$$

Combining this stability condition with the low frequency stability condition, Equation (F-7), gives

$$\frac{I\omega_o}{g} < A < I_i g_i \omega_i \qquad \text{(F-12)}$$

which can only be satisfied if

$$\frac{I_i \omega_i}{I \omega_o} \; g \; g_i > 1 \qquad \text{(F-13)}$$

It is difficult in practice to ensure that this condition will be satisfied. The control system can be improved by adding high frequency roll-off which will ensure that none of the structural modes are destabilized. The roll-off must be at least second order in order to satisfy the physical requirement that the feedback F(p) be zero at infinite frequency. If such roll-off is not provided deliberately, it will be provided by structural flexibility and other parasitic effects, with potentially unpleasant consequences. With the addition of second order roll-off, the feedback function is

$$F(p) = \frac{A(p^2 + \omega_o g p + \omega_o^2)}{p(1+p/\omega_1)(1+p/\omega_2)} \qquad \text{(F-14)}$$

which is the simplest possible form for practical integral feedback.

If $\omega_o^2 \ll \omega_1 \omega_2$, then it can be shown that the conditions for stability are

$$\frac{I \omega_o}{g} < A < I \; (\omega_1 + \omega_2) \qquad \text{(F-15)}$$

As a matter of practical design, A, ω_o, ω_1, ω_2, and g should all be chosen as large as possible in order to reduce the low frequency errors. The values of these parameters are, however, inevitably limited by the presence of structural modes.

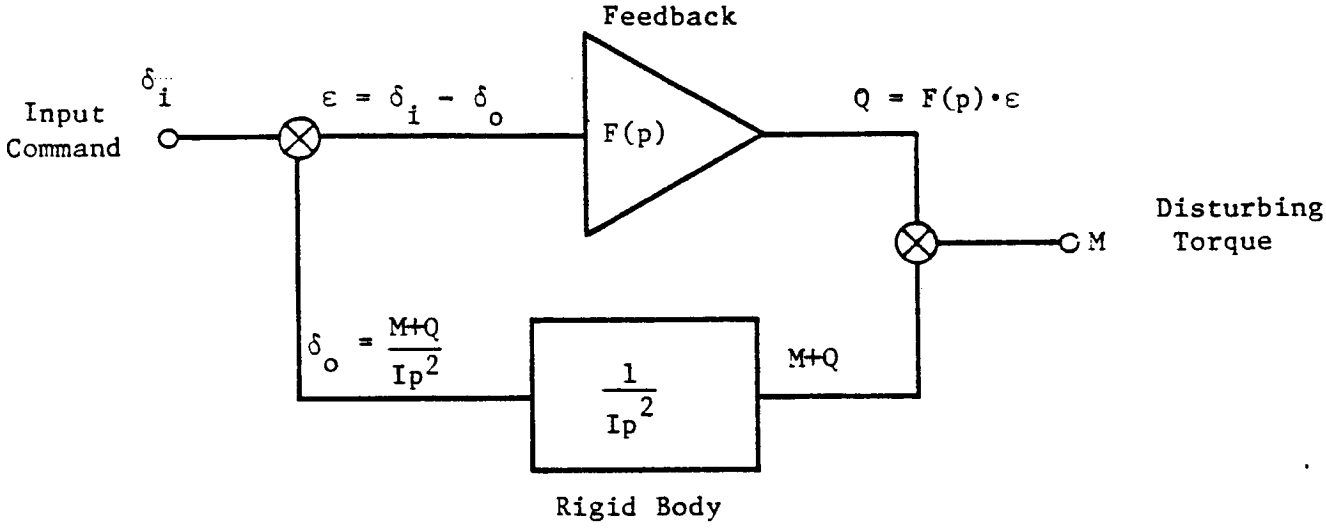


Figure F-1. Block Diagram for Control System.

CHAPTER 2

EFFECTS OF PHASE ERRORS ON ANTENNA PERFORMANCE

by

John M. Hedgepeth and Karl Knapp

CHAPTER 2

TABLE OF CONTENTS

SECTION 1: INTRODUCTION 107

SECTION 2: BASIC ANTENNA FIELD EQUATIONS AND PHASE ERROR-FREE SOLUTIONS 111

SECTION 3: THE EFFECTS OF OVERALL PHASE ERRORS 115
- 3.1 Uniform Illumination and Linear Phase Errors 117
- 3.2 Quadratic Illumination and Linear Phase Errors 120
- 3.3 Quadratic Illumination and Quadratic Errors 122
- 3.4 Quadratic Illumination of a Spherical Reflector 123

SECTION 4: THE EFFECTS OF SMALL WAVELENGTH ERRORS ON THE SECONDARY PATTERNS OF ANTENNAS WITH CIRCULAR APERTURES 126

SECTION 5: THE EFFECTS OF PHASE ERRORS ON THE SECONDARY PATTERN OF A SQUARE ANTENNA ARRAY . . . 129
- 5.1 Uniform Illumination and No Phase Errors 130
- 5.2 Uniform Illumination and Random Errors . . . 132
- 5.3 Uniform Illumination: A Checkerboard Pattern of Phase Errors 134

SECTION 6: CONCLUDING DISCUSSION 140

REFERENCES 142

APPENDIX A: PROGRAM FOR SERIES EXPANSIONS 154

APPENDIX B: PROGRAM FOR M AND N 156

LIST OF TABLES AND FIGURES

TABLE I. SECONDARY PATTERN CHARACTERISTICS PRODUCED BY A DISTRIBUTION $(1-r^2)^p$ OVER A CIRCULAR APERTURE WITHOUT PHASE ERRORS 143

Figure 1. Coordinates of a circular antenna aperture 144

Figure 2. The effect of linear phase errors on the secondary pattern of a uniformly illuminated antenna 145

Figure 3. The effect of linear phase errors on the secondary pattern of an antenna with a quadratic illumination 146

Figure 4. The effect of quadratic phase errors on the secondary pattern of an antenna with quadratic illumination 147

Figure 5. The effect of phase errors on the secondary pattern of a spherical reflector 148

Figure 6. The effect of small-scale linear phase errors on the secondary pattern of a uniformly illuminated antenna 149

Figure 7. Secondary patterns of a square antenna array without phase errors 150

Figure 8. Secondary patterns of a square antenna array with checkerboard phase errors 151

Figure 9. Effect of errors on main-lobe gain 152

Figure 10. Effect of errors on antenna side lobes 153

SECTION 1
INTRODUCTION

The successful performance of any structure depends largely on the identification of the critical or primary loads and design criteria on which the design is based. The future promises large structures which must be deployed, erected, assembled, or fabricated in space. For such structures, which will not be required to face the launch environment, the primary design requirements will be derived from the space-flight environment and will deal with phenomena as primary criteria which have been considered as only secondary in the past. The design of such genuine "space" structures will require a solid foundation of critical criteria.

This chapter examines the influences of deviations of the surface of a large radio-frequency antenna on the antenna pattern. Clearly, such information is needed in order to establish requirements on the accuracy of the structure of the antenna so that it can properly perform its mission function.

From a mission-usefulness point of view, three characteristics of an antenna pattern are important. The first is the intensity of the radiated pattern at its center. This "on-axis gain" or "main-lobe gain" is important because it establishes how much power must be supplied to the antenna in order to achieve an acceptable power density at the receiving station. Alternately, if the antenna is used as a receiver, the main-lobe gain determines the strength of the received signal relative to the strength of the various noise sources in the antenna and other parts of the receiver system.

For some missions the amount of energy of the main antenna lobe is important as the main-lobe gain. This so-called "side-lobe gain" is of concern in those type of missions in which the

radiation of energy outside the main lobe is undesirable. Geosynchronous communication systems, for example, must have low side lobes in order to avoid crosstalk among the various satellite-Earth station links that are using the same frequency channels. In sensor applications, low side lobes are required in order to eliminate the ambiguity that arises because of off-axis "hot spots."

The third characteristic is that of "main-beam efficiency." Antennas used to transmit power, for example, must concentrate the power in the main beam so that the receiver can capture it. A sensing antenna would need to minimize the power gathered outside of the main beam if the contrast were low. Microwave radiometry is an example of such an application.

The effect of antenna errors on the gain pattern arises primarily from nonuniformity of the phase of the radiated signal as it crosses the aperture plane of the antenna. This phase error in a reflector type of antenna is composed of errors arising from the antenna feed, those due to blockage, those caused at the reflector surface, and those due to improper geometry of the reflector and feed position. (If the reflector were a perfect paraboloid and the feed were located exactly at its focal point, there would be no errors from antenna geometry.) For directly radiating antennas, a similar separation of phase-error sources is possible: those due to inaccuracies in the signal fed to various antenna elements and those due to imperfect antenna geometry. In this paper, attention is focused on the phase error itself without consideration of the source; of course, the overall intent is to investigate these types of phase errors which might arise from geometrical imperfections.

The loss of main-lobe gain in the far field due to phase imperfections is generally agreed to be a straightforward function of an average phase nonuniformity. To be precise, the main-lobe

gain is proportional to exp $(-\overline{\delta^2})$ where $\overline{\delta^2}$ is the weighted mean square deviation of phase (in radians), the mean being taken across the aperture with a weighting function of the illumination intensity. This formula is given by Ruze in his classic survey paper (ref. 1). It agrees for small values of $\overline{\delta^2}$ with previous work by others, as well as the earlier work of Ruze himself. Incidentally, Ruze's earlier work contains a different form for larger values of $\overline{\delta^2}$ and purports to show that the main-lobe gain depends on the distribution of the error across the aperture in addition to the weighted mean square (ref. 2). The more recent result, in which the areal distribution has no independent effect on the main-lobe gain, is used in the results herein.

The side-lobe gain is generally agreed to be influenced by the distribution of the errors as well as their weighted mean. Ruze shows, for example, that in the case of random errors, the side-lobe gain is a strong function of the correlation interval (ref. 1). Different types of structural phenomena will create different types of phase-error distribution. For example, the distortions due to thermal effects or maneuver loads are likely to have characteristic lengths that are a large fraction of the aperture size. Such large-scale errors are termed herein as "overall" errors. On the other hand, errors due to random manufacturing inaccuracies, which are treated in ref. 3, generally have much smaller characteristic lengths. Such small-scale errors are termed herein as "local" errors.

The loss in main-beam efficiency due to phase errors is dependent on the effects on main-lobe shape as well as main-lobe gain.

This paper contains newly derived results as well as results taken from and developed from the literature for the effect on main-lobe gain and shape and side-lobe gain of various types of imperfection patterns.

SECTION 2

BASIC ANTENNA FIELD EQUATIONS AND PHASE ERROR-FREE SOLUTIONS

An estimate of the scalar diffraction pattern for a plane circular aperture can be obtained by using the Fraunhofer approximation:

$$E(\theta,\phi) = \int_0^{2\pi}\int_0^{a} f(r,\phi')e^{i\left[\delta(r,\phi') + \frac{2\pi r}{\lambda}\sin\theta\cos(\phi-\phi')\right]}rdrd\phi' \qquad (1)$$

where $f(r,\phi')$ is the magnitude of the illumination at the aperture and $\delta(r,\phi')$ is its phase. The coordinates in respect to a parabolic reflector antenna are shown in Figure 1. The above expression is referred to as the far-field equation, as it is a good approximation of the antenna field only when the distance from the antenna is large compared with the aperture radius a and beyond the interference pattern of the Fresnal zone. Reference 4 contains a complete discussion of the derivation of the Fraunhofer approximation.

For a circular aperture, it is convenient to change the variables so that

$$u = \frac{2\pi a}{\lambda}\sin\theta$$

and

$$\rho = \frac{r}{a}$$

so that the above equation becomes

$$E(u,\phi) = a^2 \int_0^{2\pi} \int_0^1 f(\rho,\phi') e^{i[\delta(\rho,\phi') + u\rho \cos(\phi-\phi')]} \rho d\rho d\phi' \tag{2}$$

If we restrict ourselves to the circularly symmetric feed illuminations characteristic of this type of antenna, then f will not depend on ϕ' so that the field equation becomes

$$E(u,\phi) = a^2 \int_0^{2\pi} \int_0^1 f(\rho) e^{i[\delta(\rho,\phi') + u\rho \cos(\phi-\phi')]} \rho d\rho d\phi' \tag{3}$$

In the special case where there are no phase errors, $\delta = 0$, the above expression can be integrated with respect to ϕ' which results in

$$E(u) = 2\pi a^2 \int_0^1 f(\rho) J_0(u\rho) \rho d\rho \tag{4}$$

For a uniform illumination, the function f = 1 and the far-field pattern become

$$E(u) = 2\pi a^2 \frac{J_1(u)}{u} \tag{5}$$

The equation for the more general case containing phase errors and tapered illuminations is more difficult to integrate.

The gain of unblocked antenna is given by

$$G(\theta,\phi) = \frac{4\pi}{\lambda^2} \frac{\left| \int_A F(\theta,\phi') dA \right|^2}{\int_A |F(\theta,\phi')|^2 dA} \tag{6}$$

where $F(\theta,\phi') = f(\rho,\phi')e^{i[\delta(\rho,\phi') + u\rho \cos(\phi-\phi')]}$ and A is the area of the aperture.

In the special case, mentioned above, of a uniform illumination with no phase errors, that gain is given by

$$G_{\delta=0}(\theta,\phi) = \frac{16\pi^2 a^2}{\lambda^2} \frac{J_1^2(u)}{u^2} \tag{7}$$

and the maximum gain occurs on the z axis where u = 0.

$$G_{\delta=0}(0) = \frac{4\pi}{\lambda^2} A \tag{8}$$

This represents a theoretical maximum for a paraboloid antenna. The effects of nonuniform illumination, phase errors, spillage, and blocking by the feed and its supports all reduce the gain achieved in practice.

Feed systems produce nonuniform illumination of the reflector resulting in nonuniform aperture fields. Generally, these distributions peak at the center of the reflector and taper to a low value at the edge. For present purposes, it is assumed that none of the feed illumination spills over the reflector edge. Spencer (ref. 5) has treated the case of distributions of the form $f\alpha(1-r^2)^p$, the treatment resulting in the general solution for no phase errors

$$E(u) = \pi^2 a^2 \frac{2^p\, p!\, J_{p+1}(u)}{u^{p+1}} = \frac{A}{p+1} \Lambda_{p+1}(u) \tag{9}$$

where Λ is the Lambda function. The characteristics of these diffraction patterns are shown in Table I. The solution for p = 0 is the uniform illumination case. These tabulated results indicate a reduction in the gain and a widening of the beam as the distribution becomes less uniform over the radius of the circular aperture. However, they also indicate that intensity of the first side lobe in relation to the on-axis gain is significantly reduced as p is increased. The gain factor, G, is the on-axis gain divided by the maximum on-axis gain of Eq. (8) for p = 0.

SECTION 3
THE EFFECTS OF OVERALL PHASE ERRORS

One important class of phase errors results from overall distortions in the mechanical shape of the antenna reflector. In order to examine the effects of these errors, circularly symmetric illuminations of the form

$$f(\rho) = (1+p)(1-\rho^2)^p \tag{10}$$

will be considered where p is an integer. Note that $f(\rho)$ has been normalized so that

$$\frac{\int_A f(\rho)dA}{\int_A dA} = 1 \tag{11}$$

Phase errors of the form

$$\delta(\rho,\phi') = g(\rho) \cos n\phi' \tag{12}$$

will be considered.

The mean square error is defined to be

$$\overline{\delta^2} = \frac{\int_A f(\rho)\delta^2(\rho,\phi')dA}{\int_A f(\rho)dA} \tag{13}$$

One method of solution is to expand the exponential term of Eq. (2) for very small errors so that

$$E(u,\phi) \tilde{=} a^2 \int_0^1 \int_0^{2\pi} f(\rho)\rho e^{iu\rho \cos(\phi-\phi')} \times \left[1 + i\, g(\rho) \cos n\phi' - \frac{g^2(\rho)}{2} \cos^2 n\phi'\right] d\rho d\phi' \quad (14)$$

where $g(\rho) \ll 1$ and terms higher than $g^2(\rho)$ have been dropped.

Let

$$\omega = \phi' - \phi$$

then

$$d\phi' = d\omega$$

and

$$E(u,\phi) \tilde{=} a^2 \int_0^1 \rho f(\rho) \int_{-\phi}^{2\pi-\phi} e^{iu\rho \cos \omega} \times \left[1 + i\, g(\rho) \cos n(\phi+\omega) - \frac{g^2(\rho)}{4} - \frac{g^2(\rho)}{4} \cos 2n(\phi+\omega)\right] d\rho d\omega \quad (15)$$

By expanding the trigonometric terms in $(\phi+\omega)$ and noting that the sine terms integrate to zero, since $e^{in \cos \omega}$ is an even function, then

$$E(u,\phi) \cong a^2 \int_0^1 \rho f(\rho) \int_{-\phi}^{2\pi-\phi} e^{iu\rho \cos \omega}$$

$$\times \left[1 + g(\rho) \cos n\phi \cos n\omega - \frac{g^2(\rho)}{4} - \frac{g^2(\rho)}{4} \cos 2n\phi \cos 2n\omega\right] d\rho d\omega \tag{16}$$

This expression can be integrated with respect to the angle ω so that

$$E(u,\phi) \cong 2\pi a^2 \int_0^1 \rho f(\rho) \left[\left(1 - \frac{g^2(\rho)}{4}\right) J_0(u\rho) + i^{(n+1)} g(\rho) J_n(u\rho) \cos n\phi\right.$$

$$\left. - (-1)^n \frac{g^2(\rho)}{4} J_{2n}(u\rho) \cos 2n\phi\right] d\rho \tag{17}$$

3.1 UNIFORM ILLUMINATION AND LINEAR PHASE ERRORS

As a first case, consider uniform illumination and linear phase errors:

Uniform illumination, $f(\rho) = 1$

Linear phase errors, $\delta(\rho,\phi') = 2\sqrt{\delta^2}\, \rho \cos n\phi'$

Substituting these expressions into Eq. (18) results in

$$E(u,\phi) \cong 2A\left[\int_0^1 \rho J_0(u\rho)d\rho - \overline{\delta^2}\int_0^1 \rho^3 J_0(u\rho)d\rho\right.$$

$$+ (i)^{n+1}\, 2\sqrt{\overline{\delta^2}}\cos n\phi \int_0^1 \rho^2 J_n(u\rho)d\rho$$

$$\left. + (-1)^{n+1}\,\overline{\delta^2}\cos 2n\phi \int_0^1 \rho^3 J_n(u\rho)d\rho\right] \qquad (18)$$

This expression can be evaluated by series expansions where

$$\left.\begin{aligned} F_n &= \int_0^1 \rho^2 J_n(u\rho)d\rho = \sum_{p=0}^{\infty} \frac{(-1)^p}{(2p+n+3)p!(p+n)!}\left(\frac{u}{2}\right)^{2p+n} \\ G_n &= \int_0^1 \rho^3 J_n(u\rho)d\rho = \sum_{p=0}^{\infty} \frac{(-1)^p}{(2p+n+4)p!(p+n)!}\left(\frac{u}{2}\right)^{2p+n} \end{aligned}\right\} \qquad (19)$$

A program suitable for use in a TI-58 or -59 calculator is shown in Appendix A. This program was used to evaluate these terms. Note that

$$\left.\begin{aligned} F_1 &= \int_0^1 \rho^2 J_1(u\rho)d\rho = \frac{J_2(u)}{u} \\ G_2 &= \int_0^1 \rho^3 J_2(u\rho)d\rho = \frac{J_3(u)}{u} \end{aligned}\right\} \qquad (20)$$

Also note that

$$\left.\begin{aligned} \lim_{u\to 0} F_0(u) &= \frac{1}{3} \\ \lim_{u\to 0} G_0(u) &= \frac{1}{4} \end{aligned}\right\} \qquad (21)$$

and that, in general, for $n > 0$ the limit of each function is zero as u goes to zero.

To examine one case in particular, let $n = 2$ so that

$$\delta(\rho,\phi') = 2\sqrt{\overline{\delta^2}}\,\rho\cos 2\phi'$$

Then

$$E(u,\phi) \cong 2A\left\{\frac{J_1(u)}{u} - \overline{\delta^2}\,[G_0(u) + G_4(u)\cos 4\phi] - i\,2\sqrt{\overline{\delta^2}}F_2(u)\cos 2\phi\right\} \qquad (22)$$

and

$$|E^2(u,\phi)| \cong 4A^2\left\{\left[\frac{J_1}{u} - \overline{\delta^2}\,(G_0+G_4\cos 4\phi)\right]^2 + 4\,\overline{\delta^2}F_2^2\cos^2 2\phi\right\} \qquad (23)$$

which, after dropping terms higher than $\overline{\delta^2}$, reduces to

$$|E^2| \cong A^2\left[\frac{4J_1^2}{u^2} - \overline{\delta^2}\,\frac{8J_1}{u}\left(G_0+G_4\cos 4\phi - \frac{2uF_2^2\cos^2 2\phi}{J_1}\right)\right] \qquad (24)$$

Since

$$\int_A |F|^2 \, dA = A \tag{25}$$

the gain is given by

$$G(u,\phi) \cong \frac{4\pi A}{\lambda^2}\left[4\frac{J_1^2}{u^2} - \overline{\delta^2}\frac{8J_1}{u}\left(G_0+G_4\cos 4\phi - \frac{2uF_2^2}{J_1}\cos^2 2\phi\right)\right] \tag{26}$$

which has been plotted in Figure 2 for $\sqrt{\overline{\delta^2}} = 0$, 0.125, and 0.250 when $\phi = 0$. This expression is identical to Eq. (7) for $\delta = 0$.

3.2 QUADRATIC ILLUMINATION AND LINEAR PHASE ERRORS

As a second case, consider quadratic illumination and linear errors:

Quadratic illumination, $f(\rho) = 2(1-\rho^2)$

Linear phase errors, $\delta(\rho,\phi') = \sqrt{6}\sqrt{\overline{\delta^2}}\,\rho\cos u\phi'$

Substituting these relations into Eq. (18) results in

$$E(u,\phi) \cong 2\pi a^2 \int_0^1 (2\rho-2\rho^3)\left[\left(1-\frac{3\overline{\delta^2}\rho^2}{2}\right)J_0(u\rho) + i^{n+1}\sqrt{6}\sqrt{\overline{\delta^2}}\,\rho\,J_n(u\rho)\cos n\phi\right.$$

$$\left. + (-1)^{n+1}\frac{3\overline{\delta^2}\rho^2}{2}J_{2n}(u\rho)\cos n\phi\right] d\rho \tag{27}$$

If we define

$$\left.\begin{aligned} H_n &= \int_0^1 \rho^4 J_n(u\rho)d\rho \\ I_n &= \int_0^1 \rho^5 J_n(u\rho)d\rho \end{aligned}\right\} \tag{28}$$

Eq. (28) can be evaluated using the program in Appendix A. Then

$$E(u,\phi) \cong 4A\left\{\frac{J_1}{u} - G_0 + i^{n+1}\sqrt{6}\sqrt{\overline{\delta^2}}(F_n - H_n)\cos n\phi \right.$$

$$\left. - \overline{\delta^2}\,\frac{3}{2}\left[G_0 - I_0 + (-1)^n(G_{2n} - I_{2n})\cos n\phi\right]\right\} \tag{29}$$

Since

$$\int_A |F^2|dA = a^2\int_0^1\int_0^{2\pi} 4(1-2\rho^2+\rho^4)\rho d\rho d\phi' = \frac{4}{3}A \tag{30}$$

the gain for n = 2, after neglecting terms higher than $\overline{\delta^2}$, is

$$G(u,\phi) \cong \frac{3\pi A}{\lambda^2}\left\{16\left[\frac{J_1}{u} - G_0\right]^2 - \overline{\delta^2}\,48\left[\left(\frac{J_1}{u} - G_0\right)\left(G_0 - I_0 + G_4\cos 4\phi - I_4\cos 4\phi\right)\right.\right.$$

$$\left.\left. - 2(F_2 - H_2)^2\cos^2 2\phi\right]\right\} \tag{31}$$

These results are shown in Figure 3 for $\sqrt{\overline{\delta^2}}$ = 0, 0.125, and 0.250 when ϕ = 0.

3.3 QUADRATIC ILLUMINATION AND QUADRATIC ERRORS

A third case of interest is to examine the effect of quadratic errors combined with a quadratic illumination.

Quadratic illumination, $f(\rho) = 2(1-\rho^2)$

Quadratic phase errors, $\delta(\rho,\phi') = 2\sqrt{3}\sqrt{\overline{\delta^2}}\,\rho^2 \cos\phi'$

Substituting these expressions into Eq. (18) results in

$$E(u,\phi) \cong 2\pi a^2 \int_0^1 2(\rho-\rho^3)\left[(1-3\,\overline{\delta^2}\rho^4)J_0(u\rho) - 3\,\overline{\delta^2}\rho^4 J_4(u\rho)\cos 4\phi - i\,2\sqrt{3}\sqrt{\overline{\delta^2}}\,\rho^2 J_2(u\rho)\cos 2\phi\right]d\rho \tag{32}$$

If we define

$$K_n = \int_0^1 \rho^7 J_n(u\rho)d\rho \tag{33}$$

Eq. (33) can be evaluated with the program in Appendix A. Then for $\phi = 0$

$$E(u,0) \cong 4A\left[\frac{J_1}{u} - G_0 - i\,2\sqrt{3}\sqrt{\overline{\delta^2}}(G_2-I_2) - \overline{\delta^2}\,3(I_0-K_0+I_4-K_4)\right] \tag{34}$$

and

$$G(u,0) = \frac{3\pi A}{\lambda^2}\left\{16\left(\frac{J_1}{u} - G_0\right)^2 - \overline{\delta^2}\,96\left(\frac{J_1}{u} - G_0\right)(I_0-K_0+I_4-K_4) - (G_2-I_2)^2\right]\right\} \tag{35}$$

These results are shown in Figure 4 for $\sqrt{\overline{\delta^2}} = 0$, 0.125, and 0.250.

3.4 QUADRATIC ILLUMINATION OF A SPHERICAL REFLECTOR

The method of solution used in the above three cases is limited to very small values of $\sqrt{\overline{\delta^2}}$ in order to ensure that $g(\rho) << 1$. A second technique can be used which avoids this limitation by performing a numerical integration of the far-field equation.

Consider phase errors of the form

$$\delta(\rho) = 6\sqrt{\frac{5}{7}}\sqrt{\overline{\delta^2}}\left(\rho^4 - \frac{1}{6}\right) \tag{36}$$

which result from the use of a spherical reflector instead of a paraboloidal reflector, and where

$$\sqrt{\overline{\delta^2}} = \frac{1}{6}\sqrt{\frac{7}{5}}\frac{\pi}{256}\frac{\frac{D}{\lambda}}{\left(\frac{F}{D}\right)^3} \tag{37}$$

where F and D are the focal length and diameter of the reflector, respectively. This relationship applies only to the case where the feed is located at the focal point. The errors can be reduced for a given wavelength and geometry by displacing the feed along the z-axis.

Substituting Eq. (36) and a quadratic illumination into Eq. (3) results in

$$E(u,\phi) = 2a^2\int_0^{2\pi}\int_0^1 (\rho-\rho^3)e^{i\,6\sqrt{5/7}\sqrt{\overline{\delta^2}}(\rho^4-1/6)}e^{iu\rho\cos(\phi-\phi')}d\rho d\phi' \tag{38}$$

This expression can be integrated with respect to ϕ' so that

$$E(u,\phi) = 4\pi a^2 \int_0^1 (\rho-\rho^3) e^{i\, 6\, \sqrt{5/7}\sqrt{\delta^2}(\rho^4-1/6)} J_0(u\rho)\, d\rho \tag{39}$$

which, after expressing the exponential in terms of trigonometric functions, results in

$$\begin{aligned} E(u) = \pi a^2\, 4 \int_0^1 (\rho-\rho^3) J_0(u\rho) \Bigg[& \cos\left(6\sqrt{5/7}\sqrt{\delta^2}\rho^4\right) \cos\left(\sqrt{5/7}\sqrt{\delta^2}\right) \\ & + \sin\left(6\sqrt{5/7}\sqrt{\delta^2}\rho^4\right) \sin\left(\sqrt{5/7}\sqrt{\delta^2}\right) \\ & + i \sin\left(6\sqrt{5/7}\sqrt{\delta^2}\rho^4\right) \sin\left(\sqrt{5/7}\sqrt{\delta^2}\right) \\ & - i \cos\left(6\sqrt{5/7}\sqrt{\delta^2}\right) \cos\left(\sqrt{5/7}\sqrt{\delta^2}\right) \end{aligned} \tag{40}$$

Define two functions

$$\left.\begin{aligned} M(u) &= 4 \int_0^1 (\rho-\rho^3) J_0(u\rho) \cos\left(6\sqrt{5/7}\sqrt{\delta^2}\rho^4\right) d\rho \\ N(u) &= 4 \int_0^1 (\rho-\rho^3) J_0(u\rho) \sin\left(6\sqrt{5/7}\sqrt{\delta^2}\rho 4\right) d\rho \end{aligned}\right\} \tag{41}$$

so that the field expression becomes

$$\begin{aligned} E(u) = A\Big(& M \cos\sqrt{5/7}\sqrt{\delta^2} - N \sin\sqrt{5/7}\sqrt{\delta^2} \\ & + i\, N \cos\sqrt{5/7}\sqrt{\delta^2} - i\, M \sin\sqrt{5/7}\sqrt{\delta^2} \Big) \end{aligned} \tag{42}$$

The gain, according to Eq. (6), is then

$$G(u) = \frac{3\pi A}{\lambda^2}(M^2+N^2) \tag{43}$$

The terms M and N can be evaluated for various values of u by numerical integration. Appendix B includes a program suitable for use in a TI-58 or -59 calculator which was used to obtain the values plotted in Figure 5 for several values of $\sqrt{\overline{\delta^2}}$.

SECTION 4

THE EFFECTS OF SMALL WAVELENGTH ERRORS ON THE SECONDARY PATTERNS OF ANTENNAS WITH CIRCULAR APERTURES

To establish the relative influence of small-scale phase errors, consider the case of uniform illumination and linear phase errors previously considered in Section 2.1. Now, a solution will be obtained for large n. Substituting $f(\rho) = 1$ and $\delta(\rho,\phi') = 2\sqrt{\overline{\delta^2}}\,\rho \cos u\phi'$ into Eq. (2) results in

$$E(u,\phi) = a^2 \int_0^{2\pi}\int_0^1 e^{i\,2\sqrt{\overline{\delta^2}}\,\rho\cos n\phi'} e^{iu\rho\cos(\phi-\phi')}\rho d\rho d\phi' \tag{44}$$

which, after substituting $\alpha = \phi' n$, becomes

$$E(u,\phi) = \frac{a^2}{n}\int_0^{2\pi}\int_0^1 e^{i\,2\sqrt{\overline{\delta^2}}\,\rho\cos\alpha} e^{iu\rho\cos(\phi-\alpha/n)}\rho d\rho d\alpha \tag{45}$$

The intergral over α to a limit at $2n\pi$ can be replaced by the summation of n integrals to a limit at 2π.

$$E(u\phi) = \frac{a^2}{n}\int_0^1 \rho d\rho \sum_{p=1}^{n}\int_0^{2\pi} e^{i\,2\sqrt{\overline{\delta^2}}\,\rho\cos\alpha}$$

$$\times\, e^{(iu\rho\cos\alpha/n\; +\; 2(p-1)\pi/n\,-\,\phi)} d\alpha \tag{46}$$

for large n and $\alpha \leq 2\pi$, $\alpha/n << 1$.

Therefore, the asymptotic approximation is

$$E(u,\phi) \sim \frac{a^2}{n}\int_0^1 \rho d\rho \sum_{p=1}^{n} e^{iu\rho \cos\left(\frac{2p-1}{n}\pi - \phi\right)} \int_0^{2\pi} e^{i\,2\sqrt{\delta^2}\,\rho\cos\alpha} d\alpha \qquad (47)$$

Since

$$\frac{i}{n}\sum_{p=1}^{n} e^{iu\rho\cos\left(\frac{2p-1}{n}\pi-\phi\right)} \cong \frac{1}{2\rho}\int_0^{2\pi} e^{iu\rho\cos(\lambda-\phi)} d\lambda = J_0(u\rho) \qquad (48)$$

then

$$E(u,\phi) \cong 2\pi a^2 \int_0^1 J_0(2\sqrt{\delta^2}\,\rho) J_0(u\rho)\rho d\rho \qquad (49)$$

which, when evaluated, becomes

$$E(u,\phi) \cong 2\pi a^2 \frac{1}{\left(u^2-4\delta^2\right)}\left[u\,J_0(2\sqrt{\delta^2})J_1(u) - 2\sqrt{\delta^2}\,J_0(u)J_1(2\sqrt{\delta^2})\right] \qquad (50)$$

The resulting gain pattern is

$$G(u) \cong \frac{4}{\left(u^2-2\delta^2\right)^2}\left[u\,J_0(2\sqrt{\delta^2})J_1(u) - 2\sqrt{\delta^2}\,J_0(u)J_1(2\sqrt{\delta^2})\right]^2 \qquad (51)$$

The on-axis gain is

$$G(0) \cong \frac{J_1^2(2\sqrt{\delta^2})}{\delta^2} \qquad (52)$$

and the ratio of gain to on-axis gain is

$$\frac{G(u)}{G(0)} \cong \frac{4J^2}{(u^2-4\overline{\delta^2})^2}\left[2\frac{J_0(2\sqrt{\overline{\delta^2}})}{J_1(2\sqrt{\overline{\delta^2}})} - 2\sqrt{\overline{\delta^2}}\,J_0(u)\right]^2 \tag{53}$$

The gain pattern has been numercially evaluated for several values of $\sqrt{\overline{\delta^2}}$ and the results are shown in Figure 6.

SECTION 5

THE EFFECTS OF PHASE ERRORS ON THE SECONDARY PATTERN OF A SQUARE ANTENNA ARRAY

The far-field equation for a square antenna array with side of length L can be written as

$$E(\theta,\phi) = \int_{-L/2}^{L/2}\int_{-L/2}^{L/2} f(\xi,\eta)e^{i[\delta(\xi,\eta)+(2\pi/\lambda)\sin\theta(\xi\cos\phi+\eta\sin\phi)]}d\xi d\eta \tag{54}$$

Consider the aperture to be divided into an N x N array as elemental squares, each one of which is denoted by integers m and n (1,2,3...N). In the elemental square (m,n), let

$$\xi = \xi_m + (2m-1)C - \frac{L}{2}$$

$$\eta = \eta_n + (2n-1)C - \frac{L}{2}$$

where

$$C = \frac{L}{2N}$$

and let f and δ be constant. Then

$$E(\theta,\phi) = \sum_{m=1}^{N}\sum_{n=1}^{N} f_{mn} e^{i\delta_{mn}} e^{-(2\pi i/\lambda)(L/2+C)\sin\theta(\cos\phi+\sin\phi)}$$

$$\times e^{(4\pi iC/\lambda)\sin\theta(m\cos\phi+n\sin\phi)}$$

$$\times \int_{-C}^{C}\int_{-C}^{C} e^{(2\pi i/\lambda)\sin\theta(\xi\cos\phi+\eta\sin\phi)} d\xi d\eta \qquad (55)$$

Integrating and squaring the absolute value yields the power to be

$$|E(\theta,\phi)|^2 = \left[\frac{\sin\left(\frac{2\pi C}{\lambda}\sin\theta\cos\phi\right)\sin\left(\frac{2\pi C}{\lambda}\sin\theta\sin\phi\right)}{\frac{\pi^2}{\lambda^2}\sin^2\theta\cos\phi\sin\phi}\right]^2$$

$$\times \sum_{m=1}^{N}\sum_{n=1}^{N}\sum_{p=1}^{N}\sum_{q=1}^{N} f_{mn} f_{pq} e^{i(\delta_{mn}-\delta_{pq})}$$

$$\times e^{4\pi iC/\lambda \sin\theta[(m-p)\cos\phi+(n-q)\sin\phi]} \qquad (56)$$

5.1 UNIFORM ILLUMINATION AND NO PHASE ERRORS

If $f_{mn} = f$ and $\delta_{mn} = 0$, then

$$|E_0(\theta,\phi)|^2 = \left[\frac{\sin\left(\frac{2\pi C}{\lambda}\sin\theta\cos\phi\right)\sin\left(\frac{2\pi C}{\lambda}\sin\theta\sin\phi\right)}{\frac{\pi^2}{\lambda^2}\sin^2\theta\cos\phi\sin\phi}\right]^2$$

$$\times \left[\frac{\sin\left(\frac{2\pi CN}{\lambda}\sin\theta\cos\phi\right)\sin\left(\frac{2\pi CN}{\lambda}\sin\theta\sin\phi\right)}{\sin\left(\frac{2\pi C}{\lambda}\sin\theta\cos\phi\right)\sin\left(\frac{2\pi C}{\lambda}\sin\theta\sin\phi\right)}\right]^2 \qquad (57)$$

$$|E_0(0,0)|^2 = (4C^2N^2)^2 = L^4 \tag{58}$$

Let the relative power be

$$P(\theta,\phi) = \frac{|E(\theta,\phi)|^2}{|E_0(0,0)|^2} \tag{59}$$

Then

$$P(\theta,\phi) = \frac{1}{L^4}\left[\frac{\sin\left(\frac{2\pi C}{\lambda}\sin\theta\cos\phi\right)\sin\left(\frac{2\pi C}{\lambda}\sin\theta\sin\phi\right)}{\frac{\pi^2}{\lambda^2}\sin^2\theta\cos\phi\sin\phi}\right]^2$$

$$\times\sum_{m=1}^{N}\sum_{n=1}^{N}\sum_{p=1}^{N}\sum_{q=1}^{N} f_{mn}f_{pq}e^{i(\delta_{mn}-\delta_{pq})}e^{(4\pi iC/\lambda)\sin\theta}$$

$$\times\ (m-p)\cos\phi + (n-q)\sin\phi \tag{60}$$

For uniform illumination and $\delta_{mn} = 0$,

$$P_0(\theta,\phi) = \left[\frac{\sin\left(\frac{\pi L}{\lambda}\sin\theta\cos\phi\right)\sin\left(\frac{\pi L}{\lambda}\sin\theta\sin\phi\right)}{\frac{\pi^2L^2}{\lambda^2}\sin^2\theta\cos\phi\sin\phi}\right]^2 \tag{61}$$

For $\phi = 0,\ \pi/4$

$$P_0(\theta,0) = \left[\frac{\sin\left(\frac{\pi 2}{\lambda}\sin\theta\right)}{\frac{\pi L}{\lambda}\sin\theta}\right]^2$$

$$P_0(\theta,\pi/4) = \left[\frac{\sin^2\left(\frac{\pi L}{\sqrt{2}\lambda}\sin\theta\right)}{\frac{\pi^2 L^2}{2\lambda^2}\sin^2\theta}\right]^2 \tag{62}$$

These gain patterns are shown in Figure 7.

5.2 UNIFORM ILLUMINATION AND RANDOM ERRORS

Let δ_{mn} be a random variable and let the illumination be uniform. Then, the expectation of the complex exponential is (see ref. 1)

$$\left\langle e^{i(\delta_{mn}-\delta_{pq})}\right\rangle = \begin{cases} 1 & \text{when } m = p \text{ and } n = q \\ e^{-\sigma_\delta^2} & \text{when } m \neq p \text{ or } n \neq q \end{cases} \tag{63}$$

where σ_δ is the standard deviation of δ, assumed to be uniform. Note that statistical independence is also assumed.

The corresponding expectation of the gain is

$$\left\langle P(\theta,\phi)\right\rangle = P_0(\theta,\phi)e^{-\sigma_\delta^2} + \frac{\left(1-e^{-\sigma_\delta^2}\right)}{N^2}\left[\frac{\sin\left(\frac{2\pi C}{\lambda}\sin\theta\cos\phi\right)\sin\left(\frac{2\pi C}{\lambda}\sin\theta\sin\phi\right)}{\left(\frac{2\pi C}{\lambda}\right)^2\sin^2\theta\cos\phi\sin\phi}\right]^2 \tag{64}$$

The main-lobe gain is

$$G_0(\delta) = P(0,0) = e^{-\sigma_\delta^2} + \frac{1-e^{-\sigma_\delta^2}}{N^2} \tag{65}$$

Define the additional side-lobe gain due to errors as

$$\Delta_{S.L.} = \frac{P(\theta,\phi) - P_0(\theta,\phi)G_0(\delta)}{G_0(\delta)} \tag{66}$$

For the present case, this gives

$$\Delta_{S.L.} = \frac{\frac{1-e^{-\sigma_\delta^2}}{N^2}}{e^{-\sigma_\delta^2} + \frac{1-e^{-\sigma_\delta^2}}{N^2}} \left\{ \frac{\sin\left(\frac{2\pi C}{\lambda} \sin\theta\cos\phi\right)\sin\left(\frac{2\pi C}{\lambda}\sin\theta\sin\phi\right)}{\left(\frac{2\pi C}{\lambda}\right)^2 \sin^2\theta\cos\phi\sin\phi} - P_0(\theta,\phi) \right\} \tag{67}$$

Of course this is zero for $\theta = 0$. If we look at the region of the first side lobe and consider $C \ll L$, then we have

$$\Delta_{S.L.} \simeq \frac{e^{-\sigma_\delta^2} - 1}{N^2} \tag{68}$$

There is a grating side lobe (for example, at $\pi C/\lambda \sin\theta = 3\pi/2$ for $\phi = 0$) but its magnitude is smaller than that above.

5.3 UNIFORM ILLUMINATION: A CHECKERBOARD PATTERN OF PHASE ERRORS

Let

$$\delta_{mn} = \delta, \quad m+n \text{ even}$$

$$= -\delta, \quad m+n \text{ odd}$$

We want to evaluate the summations in Eq. (59) for uniform illumination. First, consider a single summation

$$\sum_{m=1}^{N} e^{i\,mn\,(4\pi iC/\lambda)\sin\theta m\cos\phi} = e^{i\delta(-1)^n} \sum_{m=2,4,6}^{N} e^{(4\pi iC/\lambda)\sin\theta m\cos\phi} + e^{i\delta(-1)^{n+1}} \sum_{m=1,3,5}^{N-1} e^{(4\pi iC/\lambda)\sin\theta m\cos\phi} \tag{69}$$

Note that we have assumed that N is even.

The single summation can be closed to yield

$$e^{i\delta(-1)^n}\left[1+e^{-2i\delta(-1)^n e^{-(4\pi iC/\lambda)\sin\theta\cos\phi}}\right] e^{(N+2)(2\pi iC/\lambda)\sin\theta\cos\phi} \times \frac{\sin\left(\frac{2N\pi C}{\lambda}\sin\theta\cos\phi\right)}{\sin\left(\frac{4\pi C}{\lambda}\sin\theta\cos\phi\right)} \tag{70}$$

The double summation over m and p, after some rearrangement, is

$$\sum_{m=1}^{N}\sum_{p=1}^{N} e^{i(\delta_{mn}-\delta_{pq})} e^{(4\pi iC/\lambda)\sin\theta(m-p)\cos\phi}$$

$$= 2\left[\frac{\sin\left(\frac{\pi L}{\lambda}\sin\theta\cos\phi\right)}{\sin\left(\frac{4\pi C}{\lambda}\sin\theta\cos\phi\right)}\right]^2 \left[\cos a_{nq}\delta + \cos(b_{nq}\delta + 4\pi C/\lambda \sin\theta\cos\phi)\right] \tag{71}$$

where

$a_{nq} = 0$	$b_{nq} = 2$	n even	q even
2	0	n even	q odd
-2	0	n odd	q even
0	-2	n odd	q odd

Now, the sum over n is

$$\sum_{n=1}^{N} e^{i(-1)^n (4\pi iC/\lambda)\sin\theta n\sin\phi}$$

$$= \left[e^{i\delta} + e^{-i\delta} e^{-(4\pi iC/\lambda)\sin\theta\sin\phi}\right] \frac{\sin\left(\frac{\pi L}{\lambda}\sin\theta\sin\phi\right)}{\sin\left(\frac{4\pi C}{\lambda}\sin\theta\sin\phi\right)} \tag{72}$$

So the quadruple summation is

$$\Sigma\Sigma\Sigma\Sigma = \left[\frac{\sin\left(\frac{\pi L}{\lambda}\sin\theta\cos\phi\right)\sin\left(\frac{\pi L}{\lambda}\sin\theta\sin\phi\right)}{\sin\left(\frac{4\pi C}{\lambda}\sin\theta\cos\phi\right)\sin\left(\frac{4\pi C}{\lambda}\sin\theta\sin\phi\right)}\right]^2 |H(\theta,\phi)|^2 \tag{73}$$

where

$$H(\theta,\phi) = \left[e^{i\delta} + e^{-i\delta} e^{-(4\pi iC/\lambda)\sin\theta(\sin\phi+\cos\phi)} + e^{i\delta} e^{-(4\pi iC/\lambda)\sin\theta(\cos\phi+\sin\phi)}\right]$$

So, finally, after extensive rearrangement

$$P(\theta,\phi) = P_0(\theta,\phi)\cos^2\delta\left[1+\tan^2\delta \times \tan^2\left(\frac{2\pi C}{\lambda}\sin\theta\cos\phi\right)\tan^2\left(\frac{2\pi C}{\lambda}\sin\theta\sin\phi\right)\right] \tag{74}$$

The main-lobe gain is

$$G_0(\delta) = \cos^2\delta \tag{75}$$

The increment in relative side-lobe gain is

$$\Delta_{S.L.} = P_0(\theta,\phi)\tan^2\left(\frac{2\pi C}{\lambda}\sin\theta\cos\phi\right)\tan^2\left(\frac{2\pi C}{\lambda}\sin\theta\sin\phi\right)\tan^2\delta \tag{76}$$

This is zero for $\phi = 0$ and $\phi = \pi/2$. For other values of ϕ and for the first side lobe with $L>>C$

$$\Delta_{F.S.L.} = \frac{\sin^2\left(\frac{\pi L}{\lambda} \sin\theta \cos\phi\right)\sin^2\left(\frac{\pi L}{\lambda} \sin\theta \sin\phi\right)}{N^4} \tan^2\delta \tag{77}$$

The location of the first side lobe in the octant $\phi < \pi/4$ is approximately at

$$\frac{\pi L}{\lambda} \sin\theta \cos\phi = \frac{3\pi}{2}$$

So

$$\Delta_{F.S.L.} = \frac{\sin^2\left(\frac{3\pi}{2} \tan\phi\right)}{N^4} \tan^2\delta \tag{78}$$

This is largest at $\phi = \pi/4$. Thus

$$\Delta_{F.S.L.} = \frac{1}{N^4} \tan^2\delta \tag{79}$$

This is fairly small for reasonable δ and $N \geqslant 10$.

There are grating side lobes located, for example, at

$$\frac{2\pi C}{\lambda} \sin\theta \cos\phi = \frac{\pi}{2} \tag{80}$$

At this location

$$\frac{\pi L}{\lambda} \sin\theta \cos\phi = \frac{L\pi}{4C} = \frac{N\pi}{2} \tag{81}$$

Since N is even, $P_0(\theta,\phi) = 0$. Thus we have a indeterminate value for the grating side-lobe gain.

The limit is

$$\lim \frac{2\pi C}{\lambda} \sin\theta \cos\phi = \frac{\pi}{2}\left[\frac{\sin\left(\frac{\pi L}{\lambda} \sin\theta \cos\phi\right)}{\cos^2\left(\frac{\pi C}{\lambda} \sin\theta \cos\phi\right)}\right] \tag{82}$$

$$= N(-1)^{N/2} \tag{83}$$

Therefore

$$\Delta_{G.S.L.} = \frac{16 \sin^2 (N\pi/2 \tan\phi) \tan^2 (\pi/2 \tan\phi) \tan^2 \delta}{N^2\pi^4 \tan^2 \delta} \tag{84}$$

Again, this is maximum for $\tan\phi = 1$ and is

$$\Delta_{G.S.L.} = \frac{16}{\pi^4} \tan^2 \delta \tag{85}$$

which is not small.

$$\phi = \frac{\pi}{4}$$

$$G(\theta,\pi/4) = \left(\frac{\sin Z}{Z}\right)^4 \left[1 - \sin^2 \delta \left(1 - \tan^4 \frac{Z}{N}\right)\right]$$

where

$$Z = \frac{\pi L}{\sqrt{2}\lambda} \sin \theta = \frac{U}{\sqrt{2}} \tag{86}$$

The secondary pattern has been numerically evaluated and the results are displayed in Figure 8.

SECTION 6
CONCLUDING DISCUSSION

The effect of phase errors on main-lobe gain is summarized in Figure 9. The narrow band labeled "random error" applies to both the analysis of Ruze (ref. 1) and the square aperture results of this paper (Eq. 65). The "scallop error" and "periodic checkerboard error" curves are obtained from the large-n and square-aperture analyses herein (Eqs. 52 and 75). The "$1-\delta^2$" approximation was obtained early by Spencer (ref. 5). All the other curves differ little from $e^{-\sqrt{\overline{\delta^2}}}$.

Examination of the preceding beam patterns indicates that the errors affect primarily the magnitude of the main lobe and only secondarily its shape. Therefore, the effect of errors on the main-lobe gain is also interpreted as the effect on main-beam efficiency.

Also shown in Figure 9 are the values of rms phase error that are associated with rms surface errors of a reflector antenna of $\lambda/50$ and $\lambda/16$. Note that $\lambda/16$ is usually considered to be adequate accuracy for point-to-point communication insofar as the aperture size can be increased to achieve the desired gain. However, if high main beam efficiency is desired, then much tighter tolerances are required. Even at $\lambda/50$, which is usually considered to be a highly accurate antenna, the power loss due to errors is 6 percent.

When the influence of errors on the side-lobe gain is considered, the results, as shown in Figure 10, depend strongly on the type of the error. If the error is an "overall" one (spherical aberration, cos 2ϕ, grating side lobes), the relative side-lobe increment is large. This quantity is the growth in side-lobe intensity expressed as a fraction of the degraded main-lobe intensity. Thus, even at a reflector-surface rms error of $\lambda/50$, the growth in side-lobe peak power is only about 20 dB down from that of the main lobe.

Incidentally, the radiation pattern calculated for the "scallop" error shows the side-lobe gain to be decreased by the error. Where the power lost from the main lobe goes is a question - perhaps to the much higher lobes. At any rate, the geometrical error occurring in radial-rib types of antennas do not seem to present problems relative to the near-in side lobes.

The "local" errors produce much lower effects if they are random. Thus, for example, if the "error-area"-to-aperture-area ratio is 10^{-3} (a diameter ratio of 1/30), then the reflector surface can have an rms error of $\lambda/16$ and still have the side-lobe growth to be more than 30 dB down.

REFERENCES

1. Ruze, John: Antenna Tolerance Theory - A Review. Proc. IEEE, vol. 54, pp. 633-640, April 1966.

2. Ruze, John: Physical Limitations on Antennas. Research Laboratory of Electronics, Massachusetts Institute of Technology Technical Report No. 248, 30 October 1952.

3. Influence of Fabrication Tolerances on the Surface Accuracy of Large Antenna Structures. ARC-R-1013, Astro Research Corporation, 22 April 1980.

4. Silver, Samuel: Microwave Antenna Theory and Design. Dover Publications, Inc., New York, New York, 1965.

5. Spencer, R.C.: Paraboloid Diffraction Patterns from the Standpoint of Physical Optics, RL Report T-7, 21 October 1942.

TABLE I. SECONDARY PATTERN CHARACTERISTICS PRODUCED BY A DISTRIBUTION $(1 - r^2)^p$ OVER A CIRCULAR APERTURE WITHOUT PHASE ERRORS

p	G, GAIN FACTOR $\frac{2p + 1}{(p + 1)^2}$	θ, HALF-POWER WIDTH	POSITION OF FIRST ZERO	FIRST SIDE LOBE, dB BELOW PEAK INTENSITY
0	1.00	$1.02 \frac{\lambda}{D}$	$\sin^{-1} \frac{1.22\lambda}{D}$	17.6
1	0.75	$1.27 \frac{\lambda}{D}$	$\sin^{-1} \frac{1.63\lambda}{D}$	24.6
2	0.56	$1.47 \frac{\lambda}{D}$	$\sin^{-1} \frac{2.03\lambda}{D}$	30.6
3	0.44	$1.65 \frac{\lambda}{D}$	$\sin^{-1} \frac{2.42\lambda}{D}$	- - -
4	0.36	$1.81 \frac{\lambda}{D}$	$\sin^{-1} \frac{2.79\lambda}{D}$	- - -

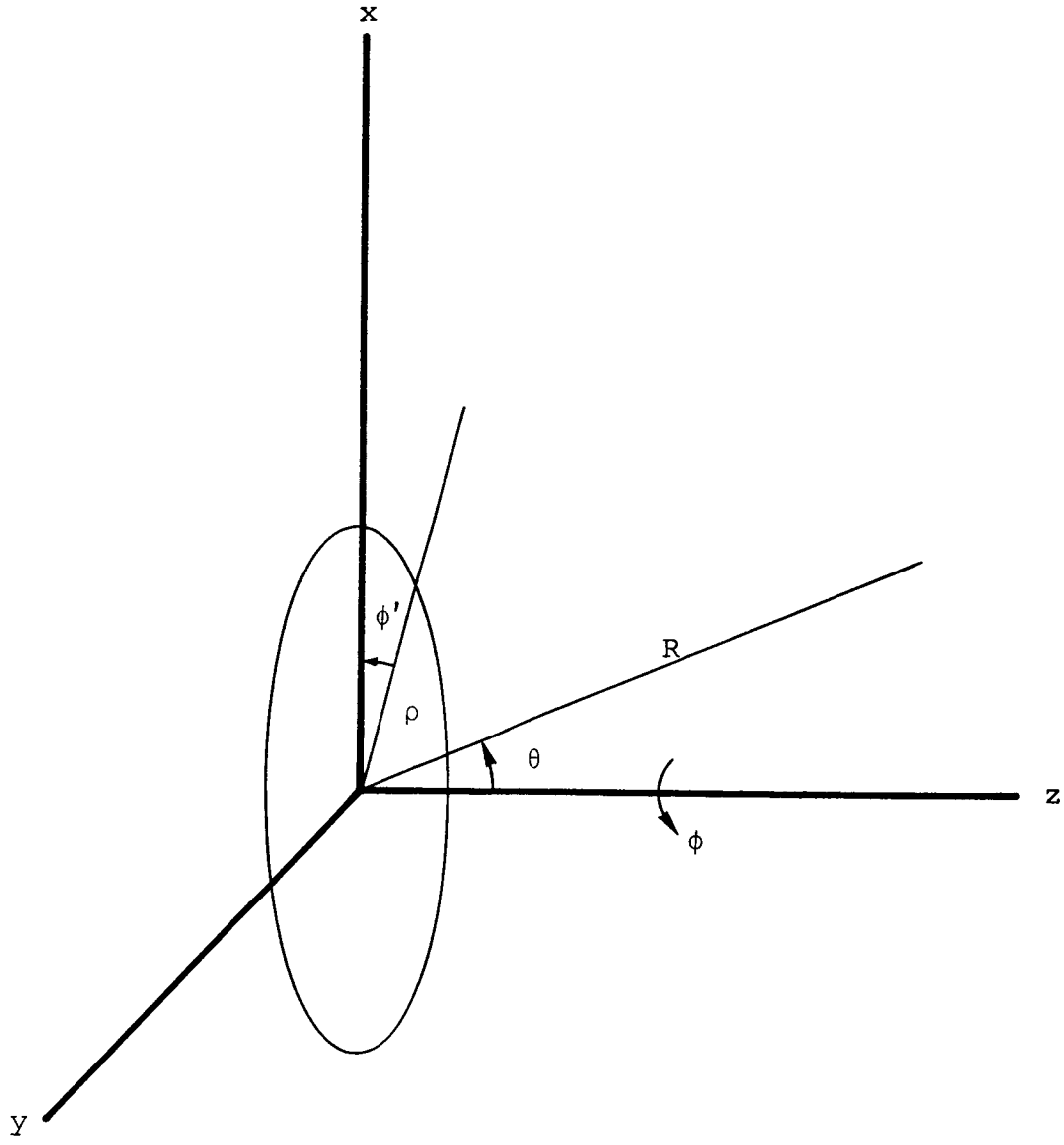


Figure 1. Coordinates of a circular antenna aperture.

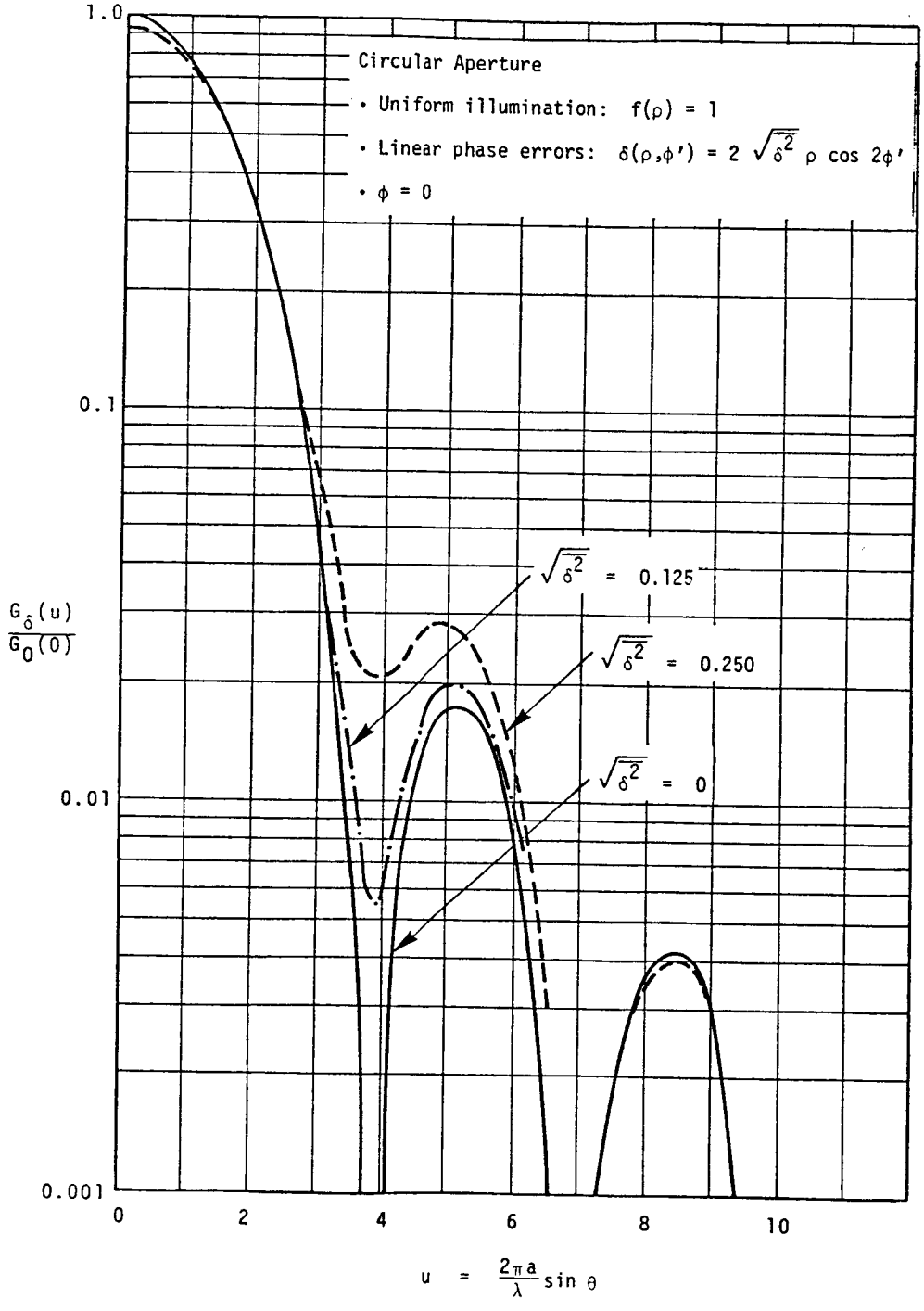


Figure 2. The effect of linear phase errors on the secondary pattern of a uniformly illuminated antenna.

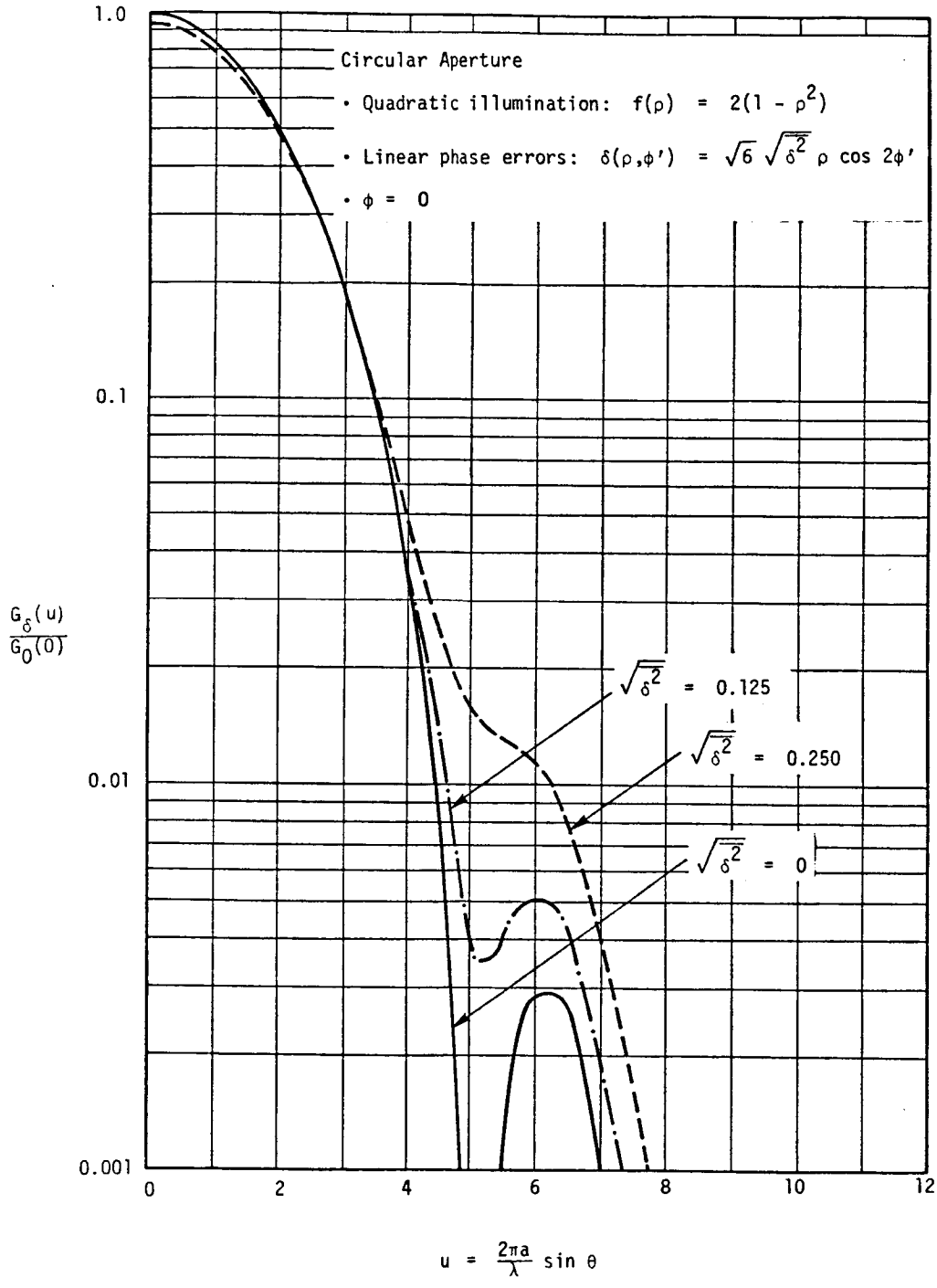


Figure 3. The effect of linear phase errors on the secondary pattern of an antenna with a quadratic illumination.

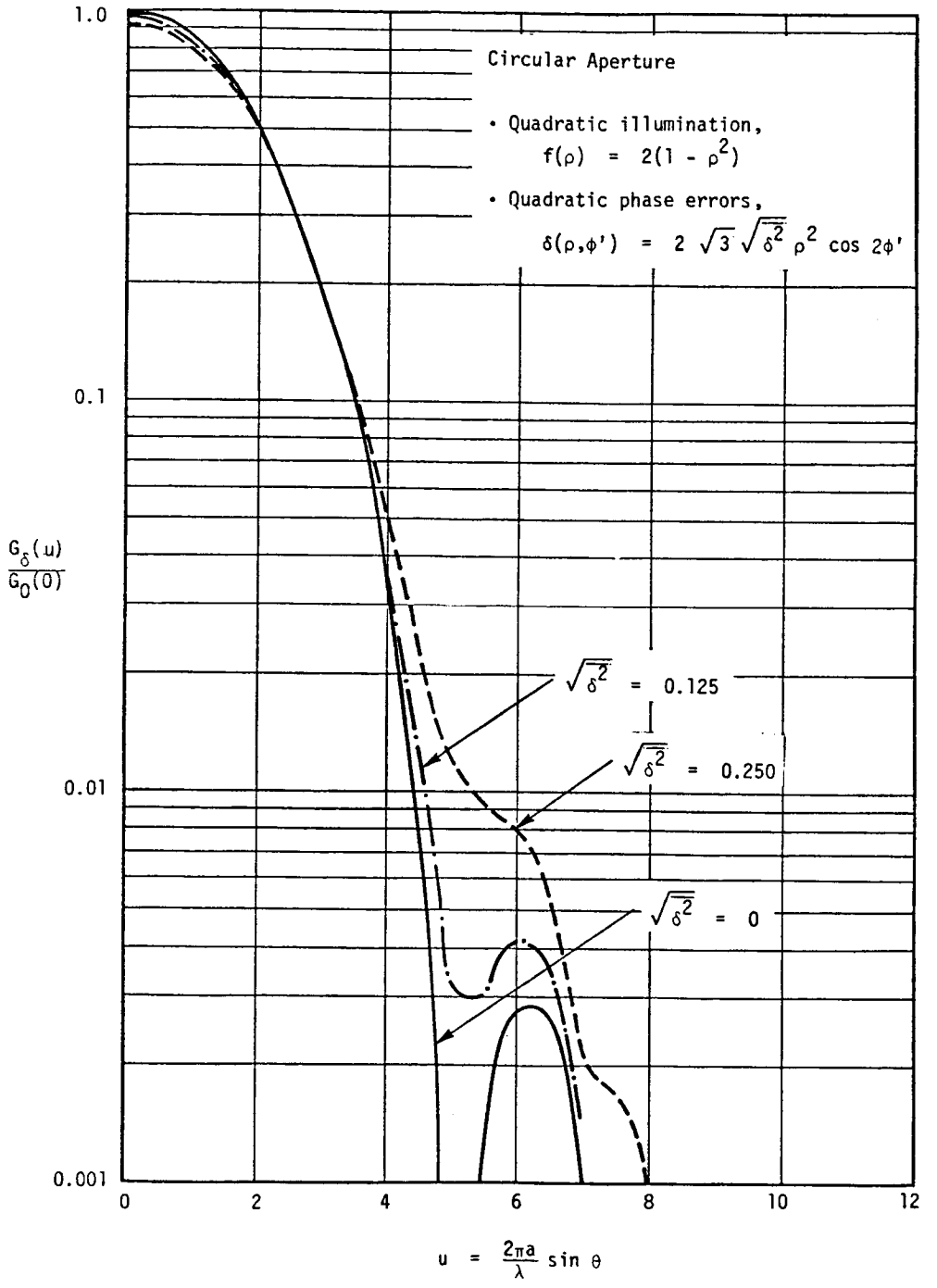


Figure 4. The effect of quadratic phase errors on the secondary pattern of an antenna with quadratic illumination.

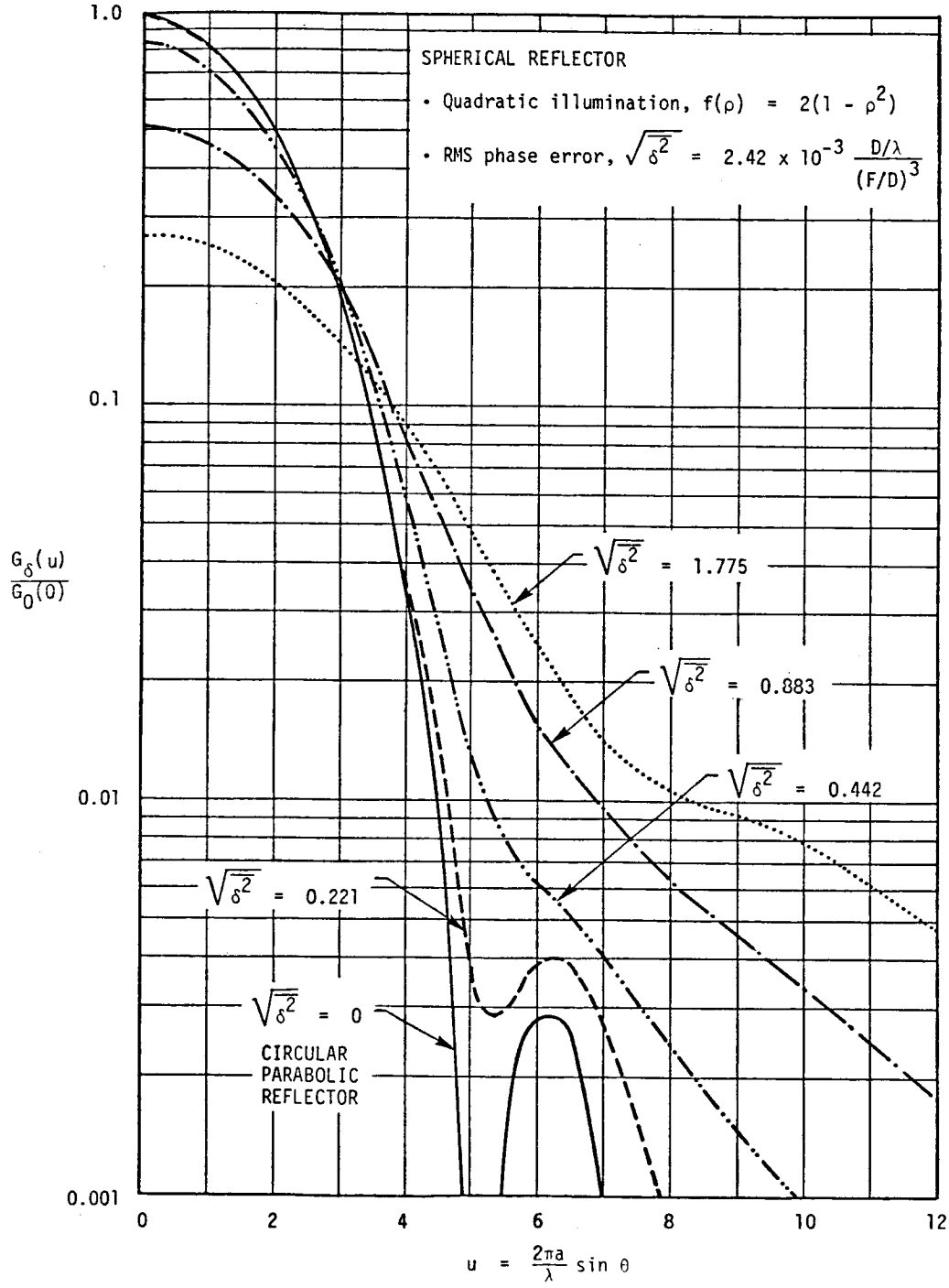


Figure 5. The effect of phase errors on the secondary pattern of a spherical reflector.

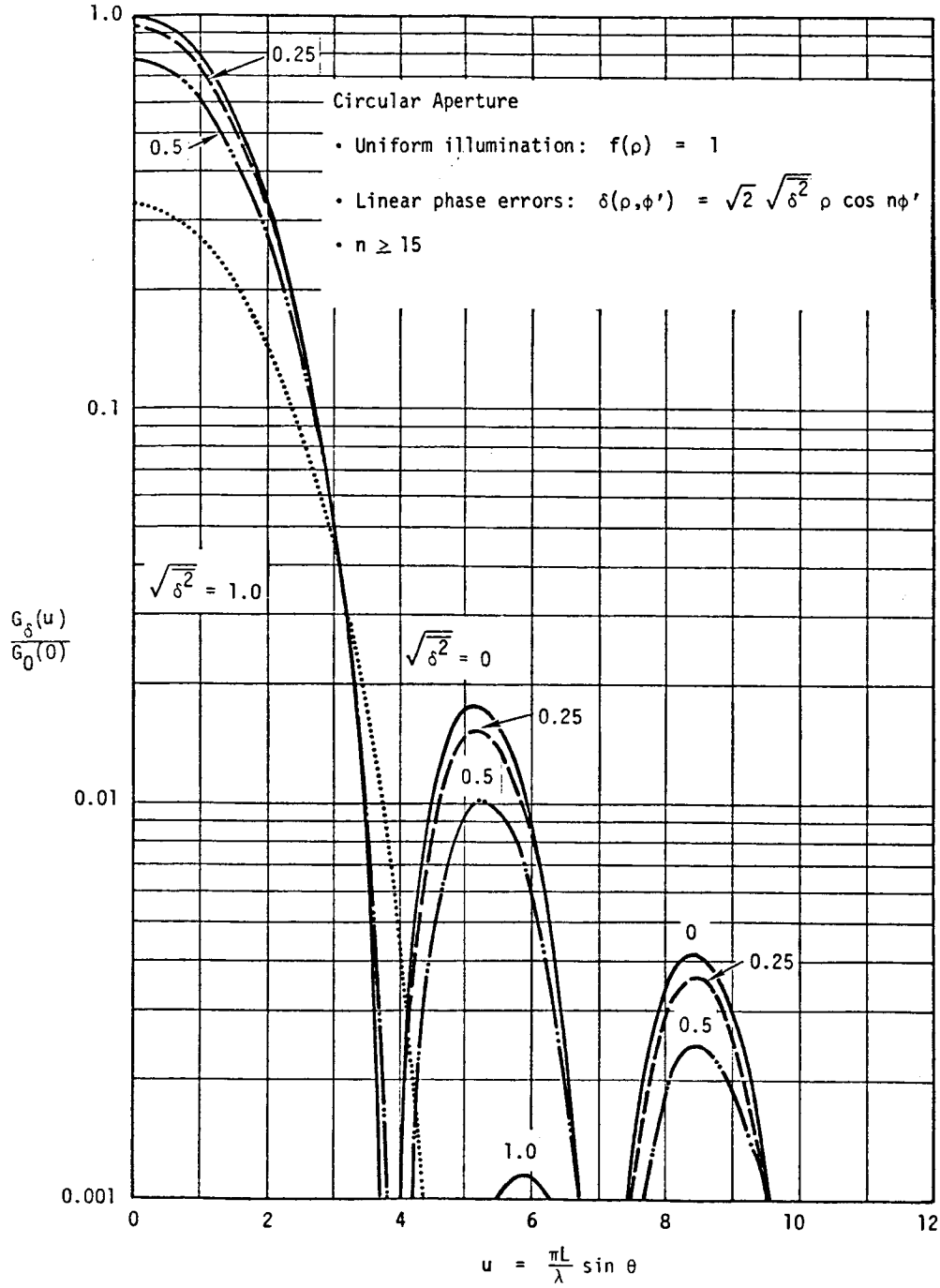


Figure 6. The effect of small-scale linear phase errors on the secondary pattern of a uniformly illuminated antenna.

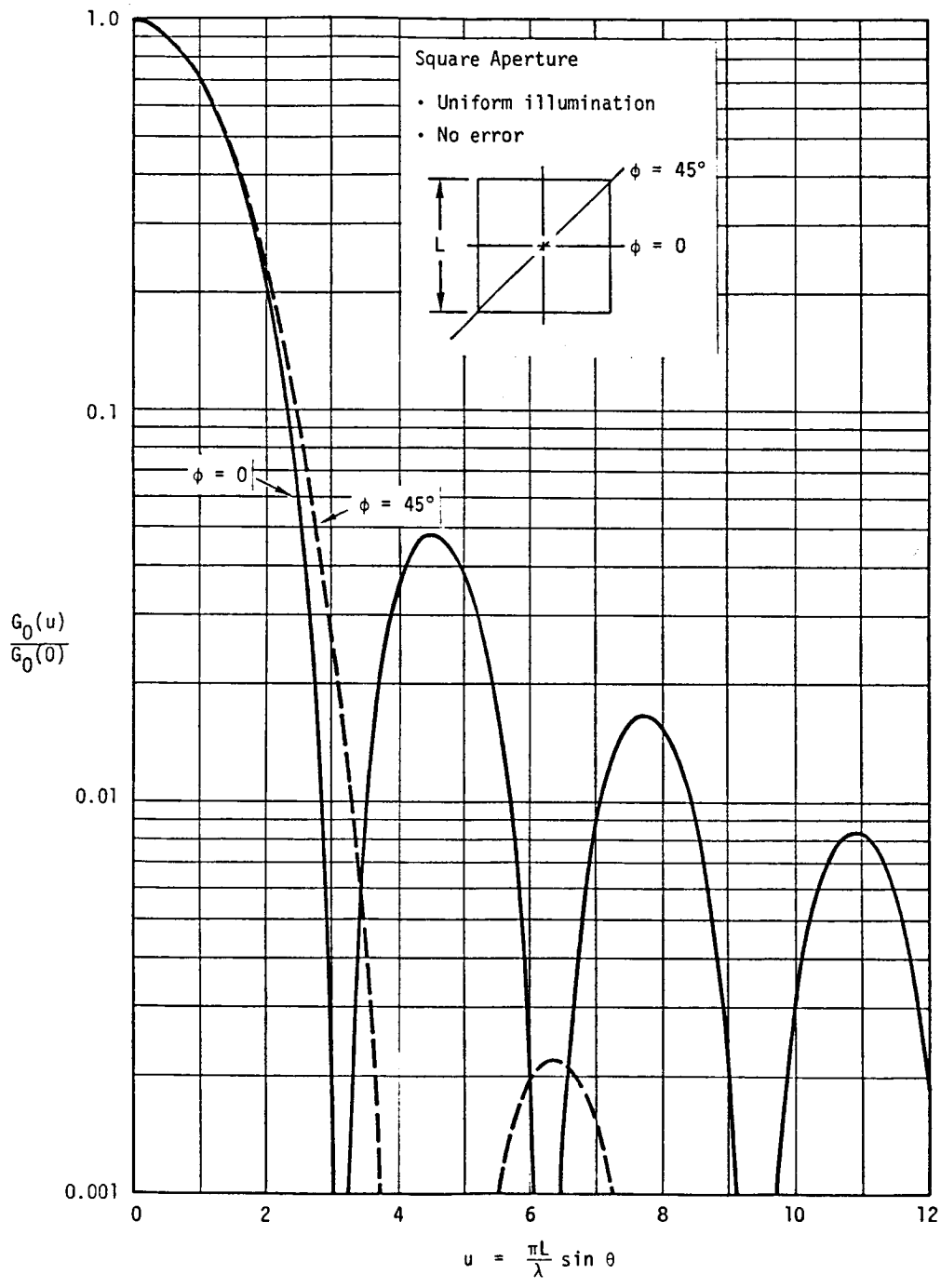


Figure 7. Secondary patterns of a square antenna array without phase errors.

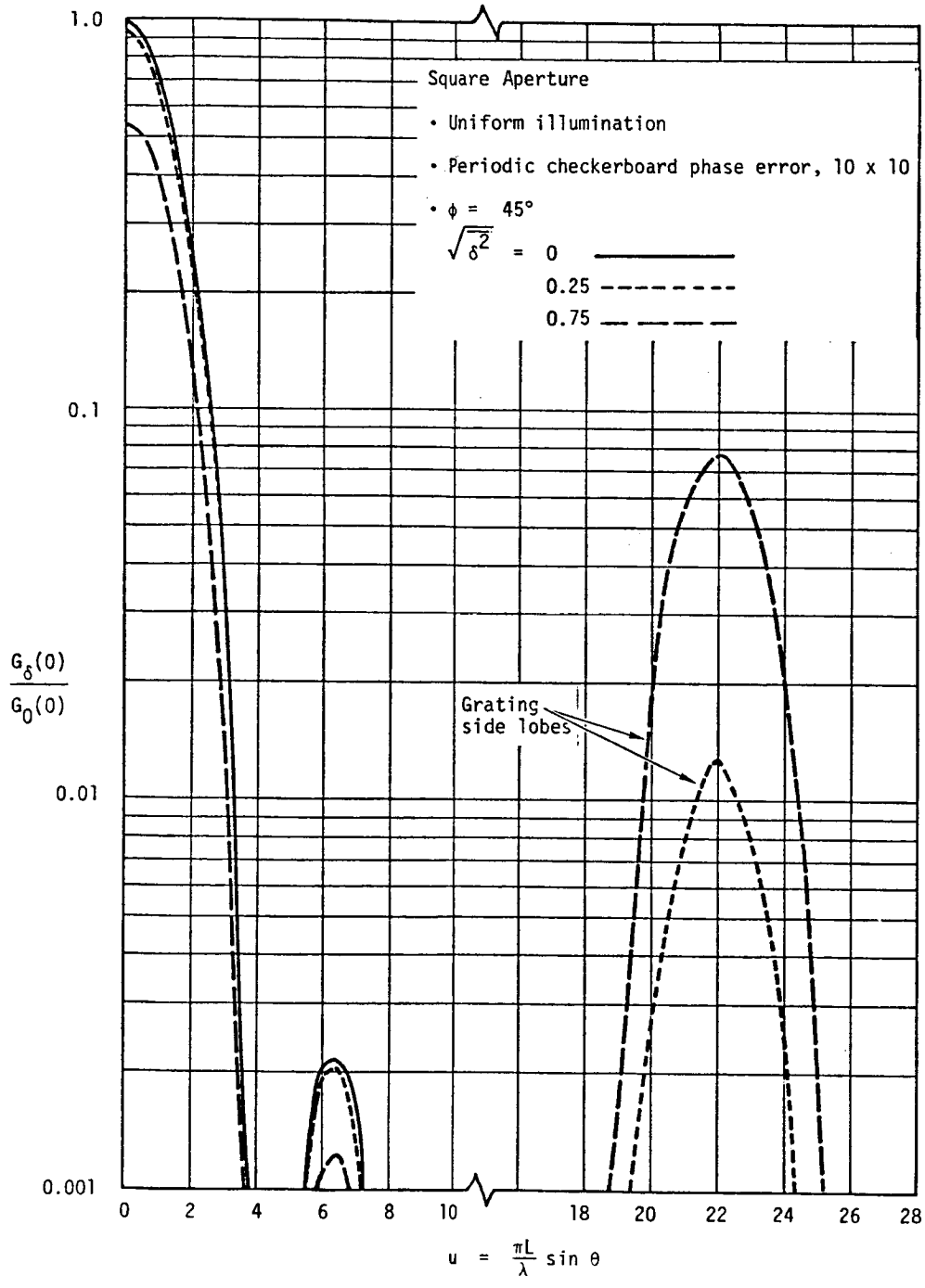


Figure 8. Secondary patterns of a square antenna array with checkerboard phase errors.

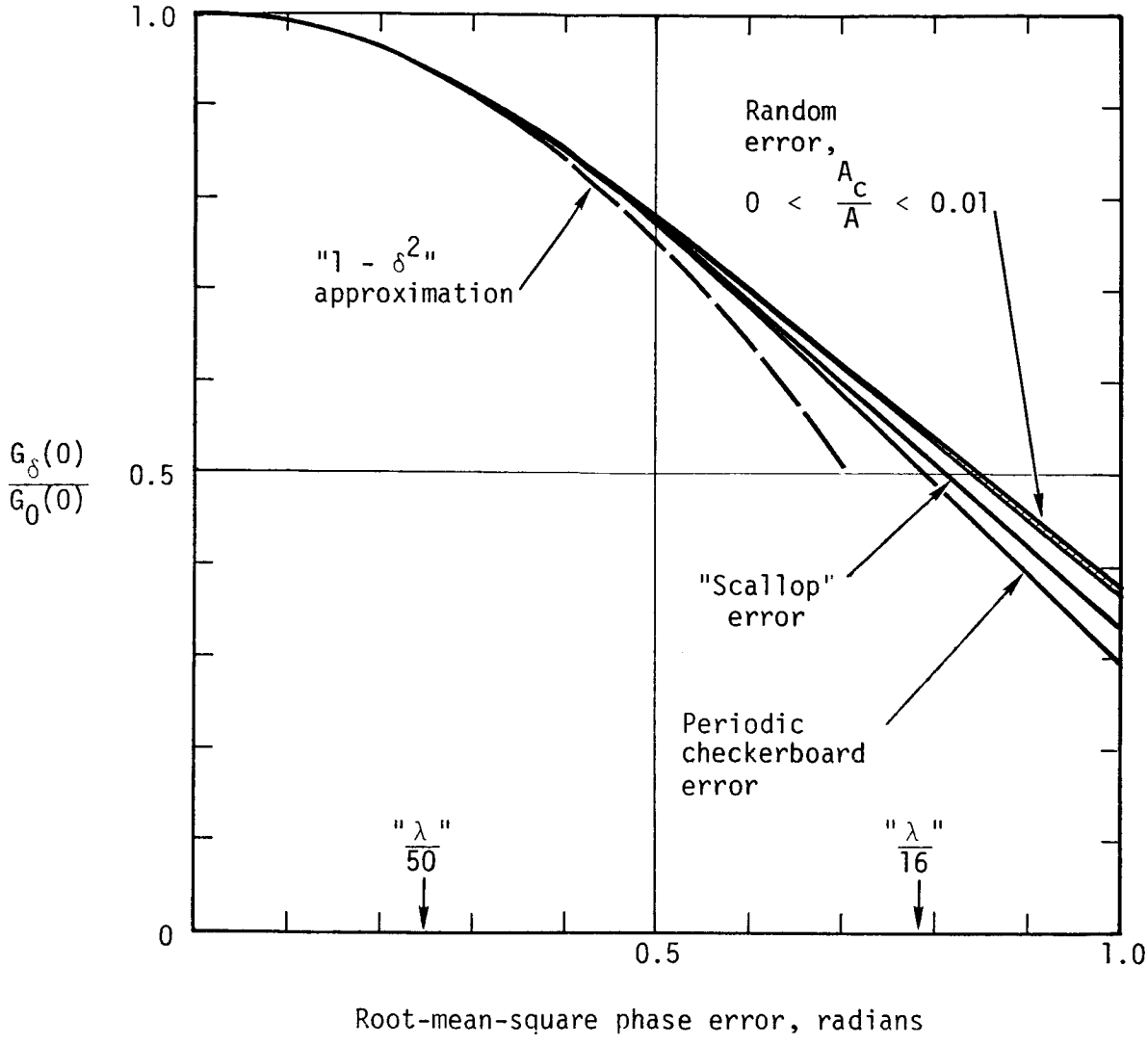


Figure 9. Effect of errors on main-lobe gain.

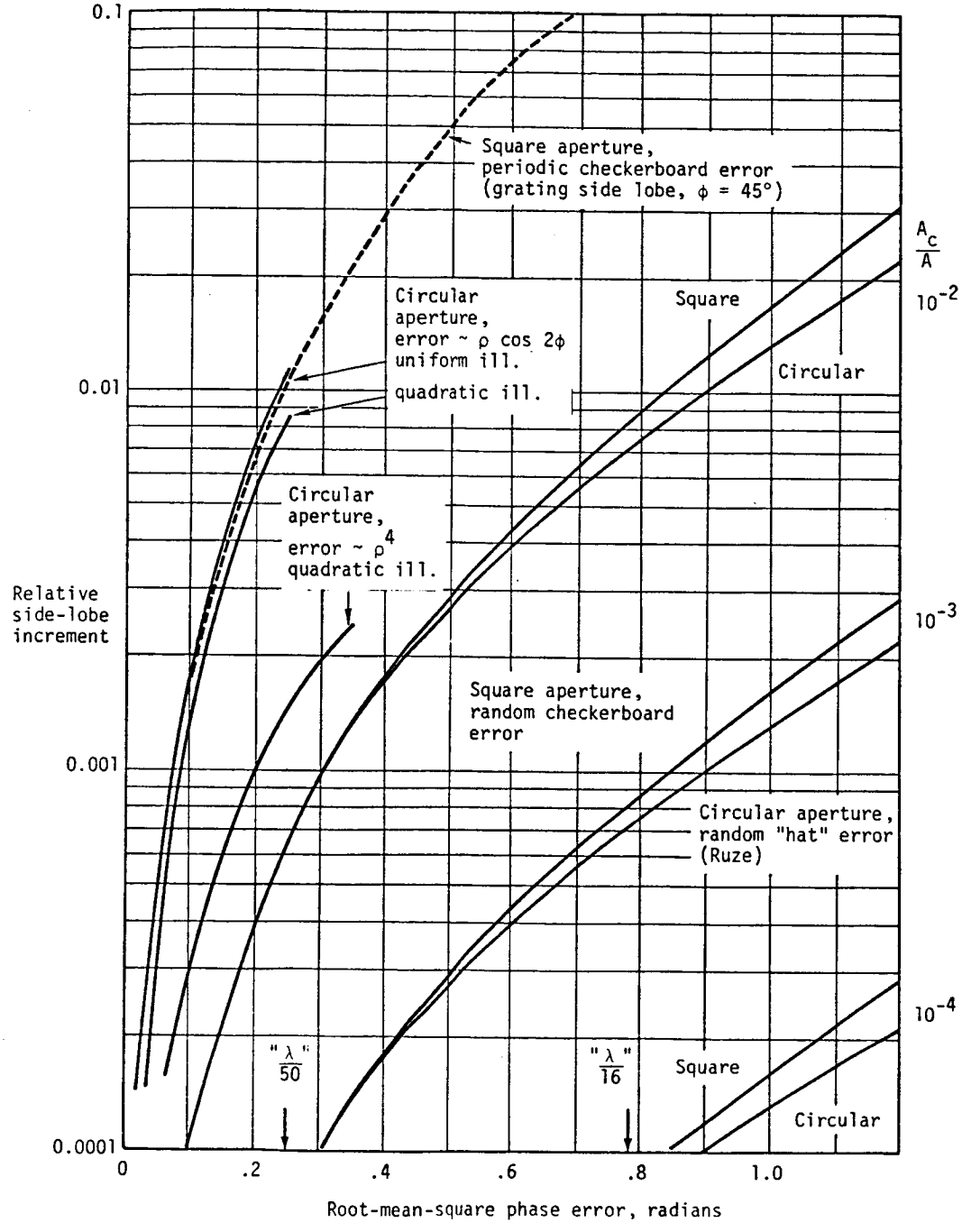


Figure 10. Effect of errors on antenna side lobes.

APPENDIX A
PROGRAM FOR SERIES EXPANSIONS

The following computer program was used to compute the expressions in Eq. (19) in the preceding text. In the present form, it computes F_n. By changing Line 60 of the computer printout to 4, it can be used to compute G_n. In a similar manner, 5 computes H_n, 6 computes I_n, and 8 computes K_n. The ranges of variables are

$$n = 0, 1, 2, 3, 4$$
$$u = 1, \ldots 20$$

For this program, use the following series of keystrokes:

2nd	CMS		
X	STO	06	Stores value for U
X	STO	11	Stores value for n
RST	CLR		
R/S			

Use 2nd FIX 4 the first time.

000	43	RCL
001	01	01
002	65	×
003	01	1
004	08	8
005	00	0
006	95	=
007	39	COS
008	42	STO
009	02	02
010	43	RCL
011	01	01
012	15	E
013	42	STO
014	03	03
015	43	RCL
016	01	01
017	85	+
018	43	RCL
019	11	11
020	95	=
021	15	E
022	42	STO
023	04	04
024	43	RCL
025	06	06
026	55	÷
027	02	2
028	95	=
029	45	Y×
030	53	(
031	43	RCL
032	01	01
033	65	×
034	02	2
035	85	+
036	43	RCL
037	11	11
038	54	)
039	95	=
040	65	×
041	43	RCL
042	02	02
043	55	÷
044	43	RCL
045	03	03
046	55	÷
047	43	RCL
048	04	04
049	95	=

050	42	STO
051	05	05
052	43	RCL
053	01	01
054	65	×
055	02	2
056	85	+
057	43	RCL
058	11	11
059	85	+
060	03	3
061	95	=
062	42	STO
063	07	07
064	43	RCL
065	05	05
066	55	÷
067	43	RCL
068	07	07
069	95	=
070	44	SUM
071	08	08
072	43	RCL
073	05	05
074	55	÷
075	53	(
076	43	RCL
077	07	07
078	85	+
079	02	2
080	54	)
081	95	=
082	44	SUM
083	09	09
084	43	RCL
085	05	05
086	55	÷
087	53	(
088	43	RCL
089	07	07
090	85	+
091	04	4
092	54	)
093	95	=
094	44	SUM
095	10	10
096	01	1
097	44	SUM
098	01	01
099	01	1

100	00	0
101	52	EE
102	05	5
103	94	+/-
104	32	X:T
105	43	RCL
106	05	05
107	50	I×I
108	77	GE
109	00	00
110	00	00
111	25	CLR
112	43	RCL
113	11	11
114	99	PRT
115	43	RCL
116	06	06
117	99	PRT
118	43	RCL
119	08	08
120	99	PRT
121	43	RCL
122	09	09
123	99	PRT
124	43	RCL
125	10	10
126	99	PRT
127	98	ADV
128	93	.
129	91	R/S
130	81	RST
131	04	4
132	02	2
133	02	2
134	04	4
135	01	1
136	00	0
137	00	0
138	00	0
139	00	0
140	69	DP
141	04	04
142	43	RCL
143	09	09
144	69	DP
145	06	06
146	06	6
147	04	4
148	02	2
149	00	0

150	00	0
151	00	0
152	00	0
153	00	0
154	00	0
155	00	0
156	00	0
157	00	0
158	00	0
159	00	0
160	00	0
161	00	0
162	00	0
163	00	0
164	00	0
165	00	0
166	00	0
167	00	0
168	00	0
169	00	0
170	00	0
171	00	0
172	00	0
173	00	0
174	00	0
175	00	0
176	00	0
177	00	0
178	00	0
179	00	0
180	76	LBL
181	15	E
182	42	STO
183	00	00
184	29	CP
185	67	EQ
186	11	A
187	76	LBL
188	12	B
189	43	RCL
190	00	00
191	65	×
192	97	DSZ
193	00	00
194	12	B
195	76	LBL
196	11	A
197	01	1
198	95	=
199	92	RTN

APPENDIX B
PROGRAM FOR M AND N

The following computer program expresses the integrands of the expressions for M(u) and N(u) in Eq. (41) of the preceding text. By using Label A, this program can be called up as part of a library program for numerical integration (using Simpson's rule). Changing the cosine term to a sine term in Step 014 relates the program to the integral for N(u) instead of M(u). The digit 4 in front of each integral has been included to simplify the ensuing computations.

```
000   76 LBL
001   16 A'
002   70 RAD
003   68 NOP
004   53  (
005   42 STO
006   06  06
007   45 Y^x
008   04  4
009   54  )
010   65  ×
011   43 RCL
012   12  12
013   54  )
014   39 COS
015   65  ×
016   43 RCL
017   06  06
018   65  ×
019   04  4
020   65  ×
021   53  (
022   01  1
023   75  -
024   43 RCL
025   06  06
026   33 X²
027   54  )
028   54  )
029   42 STO
030   07  07
031   01  1
032   42 STO
033   08  08
034   42 STO
035   13  13
036   00  0
037   42 STO
038   10  10
039   53  (
040   53  (
041   43 RCL
042   13  13
043   65  ×
044   01  1
045   94  +/-
046   54  )
047   55  ÷
048   53  (
049   53  (
050   43 RCL
051   10  10
052   85  +
053   01  1
054   54  )
055   33 X²
056   54  )
057   65  ×
058   53  (
059   53  (
060   53  (
061   43 RCL
062   11  11
063   65  ×
064   43 RCL
065   06  06
066   54  )
067   55  ÷
068   02  2
069   54  )
070   33 X²
071   54  )
072   54  )
073   44 SUM
074   08  08
075   42 STO
076   13  13
077   50 I×I
078   32 X↕T
079   01  1
080   52 EE
081   04  4
082   94  +/-
083   77  GE
084   00  00
085   94  94
086   00  0
087   32 X↕T
088   01  1
089   44 SUM
090   10  10
091   61 GTO
092   00  00
093   39  39
094   53  (
095   43 RCL
096   08  08
097   65  ×
098   43 RCL
099   07  07
100   54  )
101   92 RTN
```

CHAPTER 3

DEPLOYMENT OF FOLDED FOIL SURFACES

by

Karl Knapp and Charles S. MacGillivray

CHAPTER 3

TABLE OF CONTENTS

SECTION 1: INTRODUCTION 163

SECTION 2: ANALYSIS OF ALTERNATING PARALLEL FOLDS 164

SECTION 3: EXPERIMENTAL TESTS 167

3.1 Tests on an Aluminum Foil Strip with Alternating Parallel Folds 167

3.2 Tests on a Square Foil Surface with Folds in Two Directions 168

SECTION 4: CONCLUSIONS 169

REFERENCES 170

APPENDIX A: TESTS ON ALUMINIM FOIL STRIPS WITH ALTERNATING PARALLEL FOLDS 178

APPENDIX B: TEST ON A SQUARE FOIL SURFACE WITH FOLDS IN TWO DIRECTIONS 199

LIST OF FIGURES

Figure 1. Alternating parallel creases in a film or foil . . . 171

Figure 2. Membrane tension required to flatten creased film 172

Figure 3. Test sample under load 173

Figure 4. Extension of folded foil section under tension . . . 174

Figure 5. Fold height of folded foil under tension 175

Figure 6. Deployment of a foil surface folded in two directions 176

Figure 7. Deployment of a foil surface folded in two directions 177

SECTION 1
INTRODUCTION

The successful development of any structure depends largely on the identification of the critical or primary loads and other requirements on which the design is based. The future promises large structures which must be deployed, erected, assembled, or fabricated in space. For such structures, which will not be required to face the launch environment, the primary design requirements will be derived from the space-flight environment and will deal with phenomena as primary criteria which have been considered as only secondary in the past. The design of such genuine "space" structures will require a solid foundation of critical criteria.

This chapter deals with a preliminary investigation of the tensions required to flatten metallized films or thin metal foils after they have been packaged in a folded condition.

Metallized films and thin metallic foils are candidate materials for the surfaces of a variety of large space structures. The reflecting metal surface is usually required for solar or radio frequency reflectors where a smooth surface is desired for best performance. Normally, the material must be folded in the launch package and then deployed in space. It is of particular interest to determine the tension required to pull the material sufficiently flat for the mission.

Astro Research Corporation has investigated previously the shortening effect of transverse folds in tapes (see ref. 1). A simplified model of a material with alternating folds in one direction is examined here. Also, experimental results on metal foil samples with both two- and three-dimensional folds are presented.

SECTION 2
ANALYSIS OF ALTERNATING PARALLEL FOLDS

Consider a length of material of thickness t with alternating parallel folds under a tension N as shown in Figure 1. Let s be the distance along the surface perpendicular to the folds and 2b the spacing between folds. Then for a unit width ℓ the moment on the film is

$$M = Nw\ell \tag{1}$$

and the curvature is given by

$$\frac{d\theta}{ds} = \frac{M}{EI} \tag{2}$$

where

$$\cos\theta = \frac{dw}{ds} \tag{3}$$

Substituting Eqs. (1) and (3) into Eq. (2) gives

$$\cos\theta \cdot d\theta = -\frac{N\ell}{EI} wdw \tag{4}$$

For tensions where the surface is nearly flat

$$\theta = \frac{\pi}{2} \text{ at } z = 0,\ w = 0$$

Integrating Eq. (4), we get

$$\int_{\pi/2}^{\theta} \cos\theta \cdot d\theta = -\frac{N\ell}{EI} \int_{0}^{w_0} wdw \tag{5}$$

which results in

$$1 - \sin\theta = \frac{N\ell}{EI}\frac{w^2}{2} \tag{6}$$

or

$$w = \sqrt{\frac{2EI}{N\ell}(1 - \sin\theta)}$$

Calculating the root mean square displacement gives

$$\sqrt{\overline{w^2}} = \left(\frac{2}{b}\int_0^{b/2} w^2 dz\right)^{1/2} \tag{7}$$

Substituting Eq. (6) and the following

$$dz = \frac{\sin\theta}{\cos\theta}\,dw$$

$$dw = -\frac{\sqrt{\frac{2EI}{N\ell}}\,d(\sin\theta)}{\sqrt{1 - \sin\theta}}$$

into Eq. (7) results in

$$\sqrt{\overline{w^2}} = \left[-\frac{2}{b}\int_1^{\sin\theta_0}\left(\frac{2EI}{N\ell}\right)^{3/2}\frac{(1 - \sin\theta)^{1/2}\sin\theta\,d(\sin\theta)}{(1 - \sin^2\theta)^{1/2}}\right] \tag{8}$$

Letting $y = \sin\theta$ we get

$$\sqrt{\overline{w^2}} = \left[\frac{2}{b}\int_{\sin\theta}^{1}\left(\frac{2EI}{N\ell}\right)^{3/2}\frac{y\,dy}{\sqrt{1 + y}}\right]^{1/2} \tag{9}$$

This integral is listed in most tables of integrals as

$$\frac{\sqrt{\overline{w^2}}}{b} = 2\left(\frac{2EI}{b^2 N\ell}\right)^{3/4}\left[\frac{(2)^{3/2} - (1+\sin\theta_0)^{3/2}}{3} - \sqrt{2} + \sqrt{1+\sin\theta_0}\right]^{1/2} \tag{10}$$

Numerical results have been calculated and plotted in Figure 2.

The half angle θ_0 at each fold is also influenced by the tension on the material. Normally, this angle is established by the maximum tension that has been applied. If the fold behaves like a plastic hinge, then from ref. 1 we find that

$$M_0 = \frac{\sigma y t^2}{4}\ell = Nw_0\ell \tag{11}$$

where σy is the material yield stress.

Evaluating w_0 by Eq. (6) and substituting the result into Eq. (11) results in

$$\frac{\sigma y t^2}{4} = -N\ell\sqrt{\frac{2EI}{N\ell}(1-\sin\theta_0)} \tag{12}$$

or solving for θ_0 we obtain

$$\theta_0 = \sin^{-1}\left(1 - \frac{3}{8}\frac{\sigma_y^2 t}{NE}\right) \tag{13}$$

Unfortunately, the model is not useful for a work-hardening material such as aluminum.

SECTION 3
EXPERIMENTAL TESTS

3.1 TESTS ON AN ALUMINUM FOIL STRIP WITH ALTERNATING PARALLEL FOLDS

Recognizing that the analysis provided limited understanding of the tensions required to flatten a creased aluminum foil, three tests were conducted on creased aluminum foil samples. The specifications of the test samples were:

Aluminum	Reynolds Wrap broiling foil
Thickness	2.54×10^{-5} m
Width	0.10 m
Length	1.20 m
Length of folded section .	1.00 m
Fold spacing	0.020 m

The samples were tested on a horizontal table dusted with talc to reduce friction. Tension was applied by dead weights via a string and pulley system. The length of the folded section, the height of the folds, and the half angle at the folds were measured under increasing load. A photograph of a test sample under load is shown in Figure 3. Results of these tests are shown in Figures 4 and 5. The test data has been included in Appendix A.

The fold angle θ_0 at the tip of each fold proved to be very difficult to measure even with the load removed from the foil strip. And, because of the work hardening characteristic of the aluminum, this angle cannot be predicted by analysis. However, Eq. (6) has been plotted along with experimental data in Figure 5 for an assumed constant θ_0 of 60°. The experimental measurements of fold height shown on Figure 5 are somewhat ambiguous since at small loads the measurement represents $2w_0$, and at high loads the measurement is closer to w_0.

3.2 TESTS ON A SQUARE FOIL SURFACE WITH FOLDS IN TWO DIRECTIONS

A second series of tests was conducted on a square foil sample with the following dimensions:

Thickness	2.54×10^{-5} m
Sides	0.457 m
Fold spacing	0.020 m

Arcs were cut in each edge of the foil, removing about 10 percent of the area, and nylon cord catenaries were attached. The film was folded and packaged using the scheme shown in the photographs of Appendix B. Known loads were applied to the catenaries in small increasing increments. The expansion of the film and average fold height were measured, and the radius of the catenary was estimated for each condition. Photographs of the expanding foil and test data are included in Appendix B. Results of the tests are shown in Figures 6 and 7.

SECTION 4
CONCLUSIONS

This preliminary investigation has shown that the effects of work hardening at creases in folded aluminum foil require very high tensions in order to flatten the film in the region of the creases. Plastic effects also defeat the usefulness of analytical predictions. Fortunately, there are alternate surfaces available for both optical and radio frequency applications that large eliminate the difficulty associated with deploying foils. Optical surfaces can use polymer film coated with very thin layers of metal, minimizing the problems associated with foils and reducing the mass per unit area as well. Knit meshes are available for radio frequency reflector surfaces which, if they are tensioned, perform well and eliminate creasing in the packaged condition.

Initially this preliminary study was viewed as a means of developing a model to predict the behavior of metallized films as well as metal foils. However, the difficulty experienced in predicting the behavior of the "plastic hinge" at each crease, and in measuring the fold angles experimentally, eliminated any possibility of extending the results. It appears that to establish the loads required to flatten metallized films, tests must be conducted on the specific coated film material. Plastic effects also occur when metallized film is creased, and although the problems may be smaller than those experienced with foil, serious consideration should be given to packaging techniques which avoid folding or which minimize the number of folds.

REFERENCES

1. MacNeal, R.H.; and Robbins, W.M., Jr.: Tensile Properties of a Tape with a Transverse Crease. ARC-R-241, Astro Research Corporation, 1 November 1965.

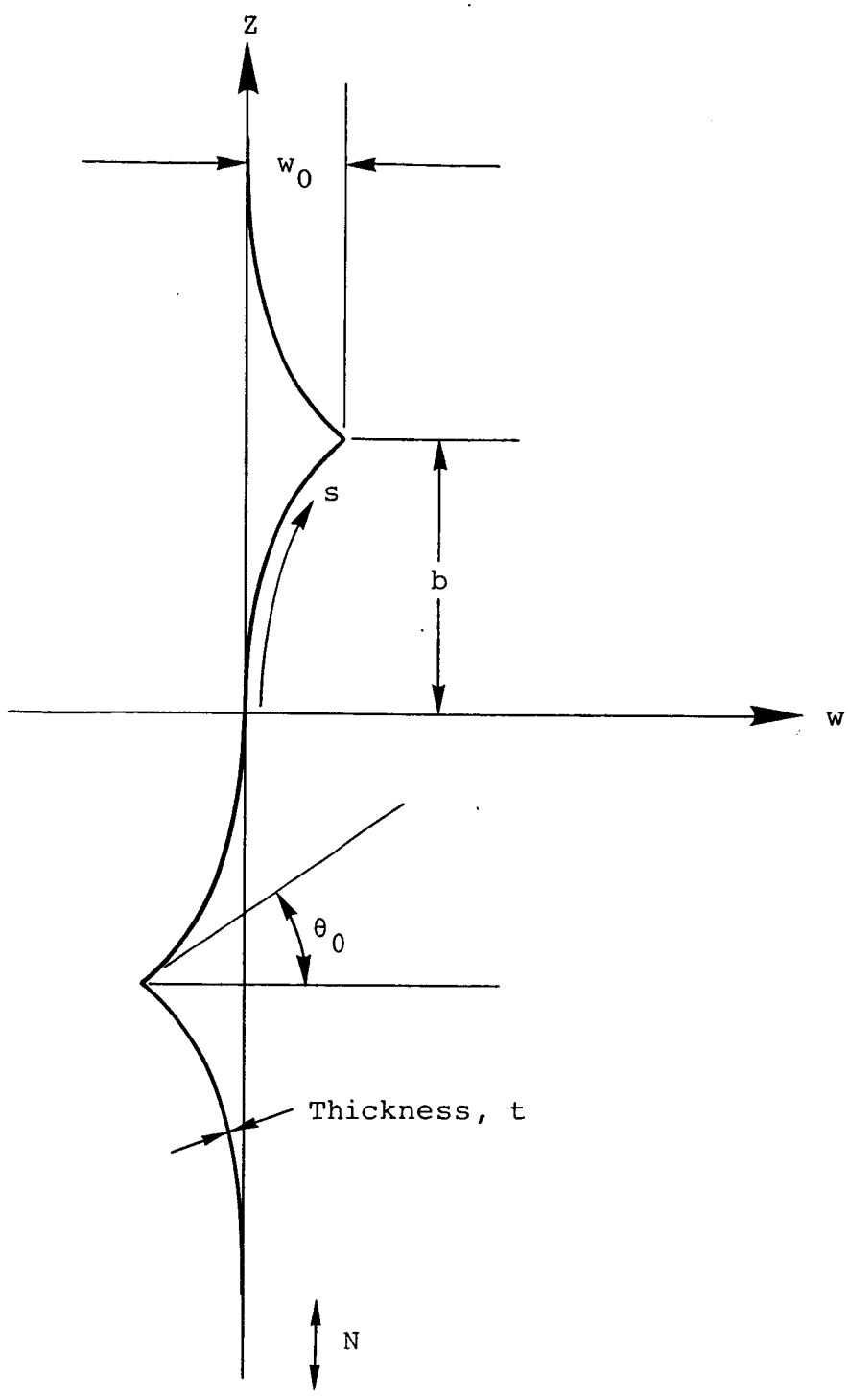


Figure 1. Alternating parallel creases in a film or foil.

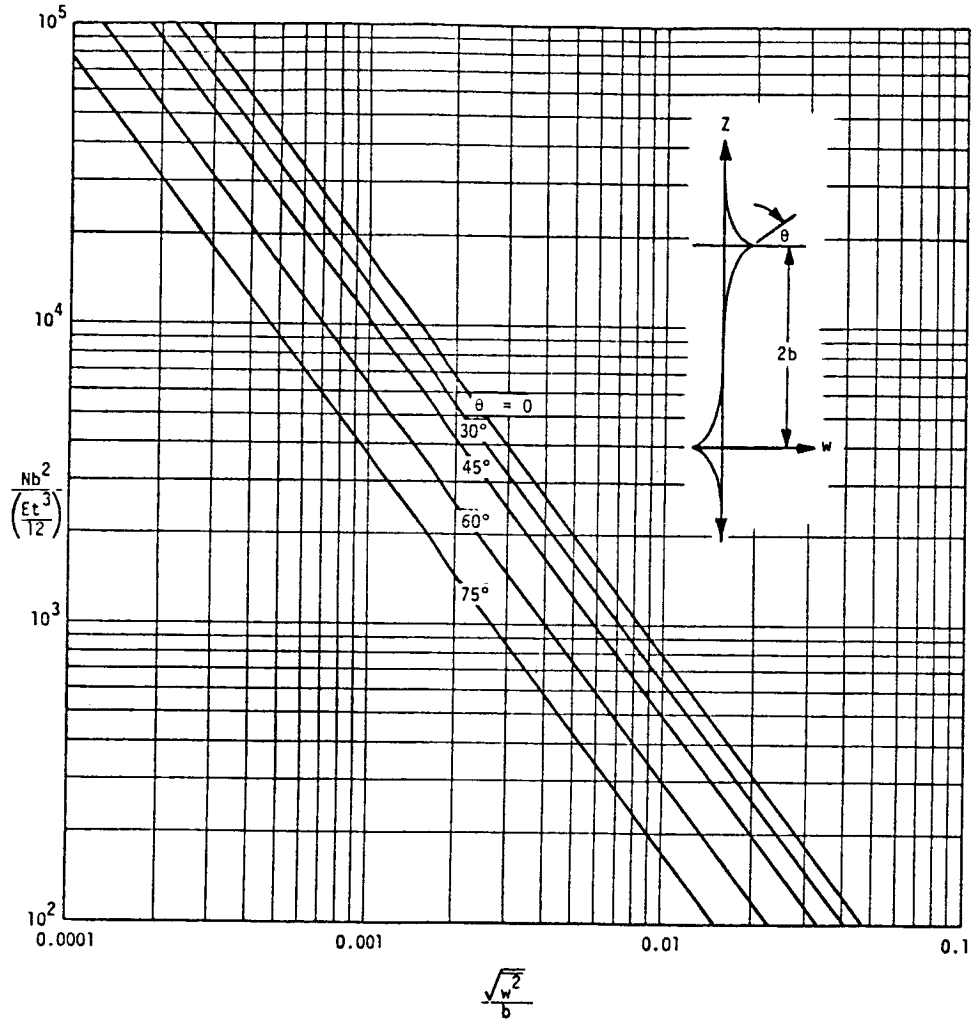


Figure 2. Membrane tension required to flatten creased film.

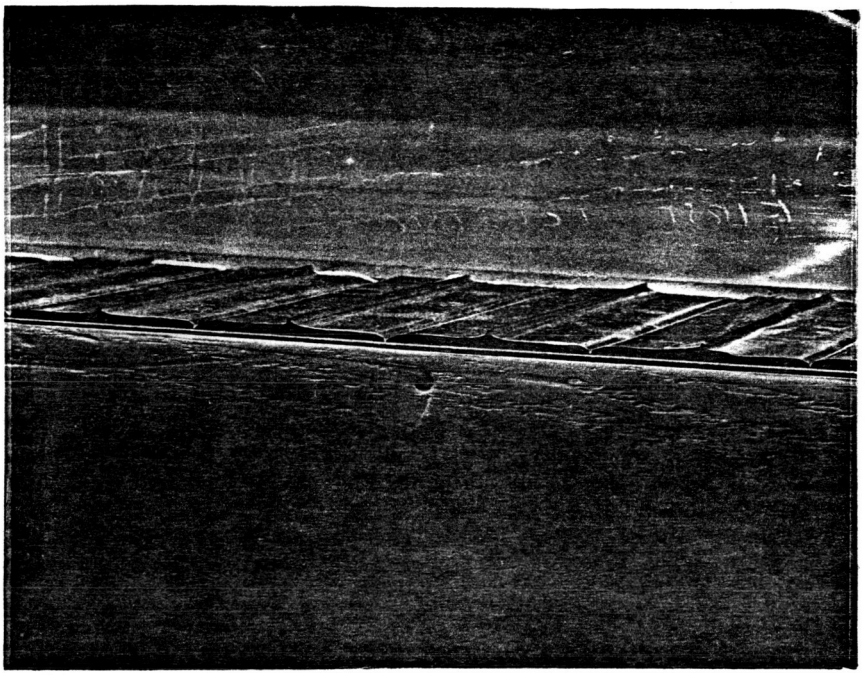


Figure 3. Test sample under load.

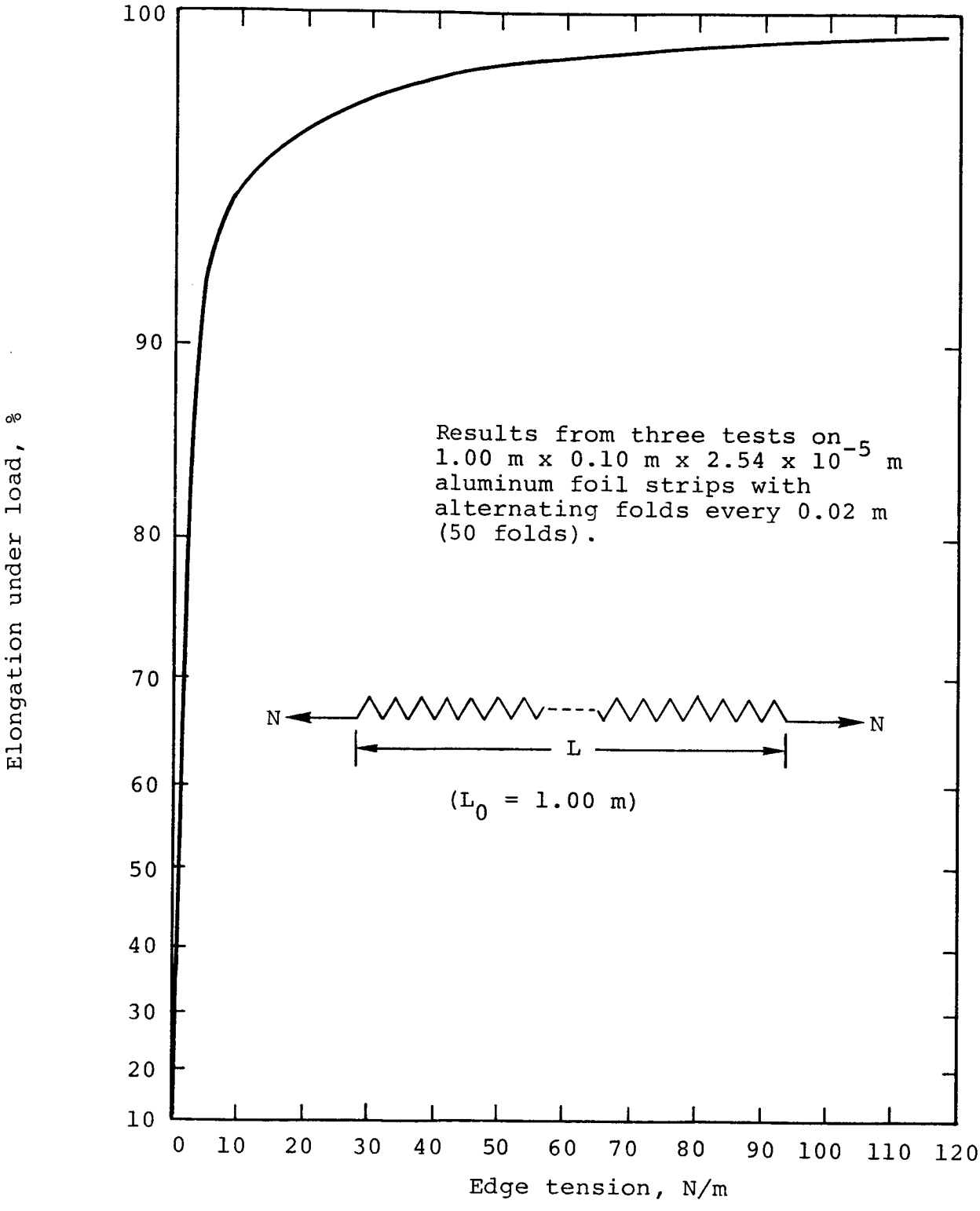


Figure 4. Extension of folded foil section under tension.

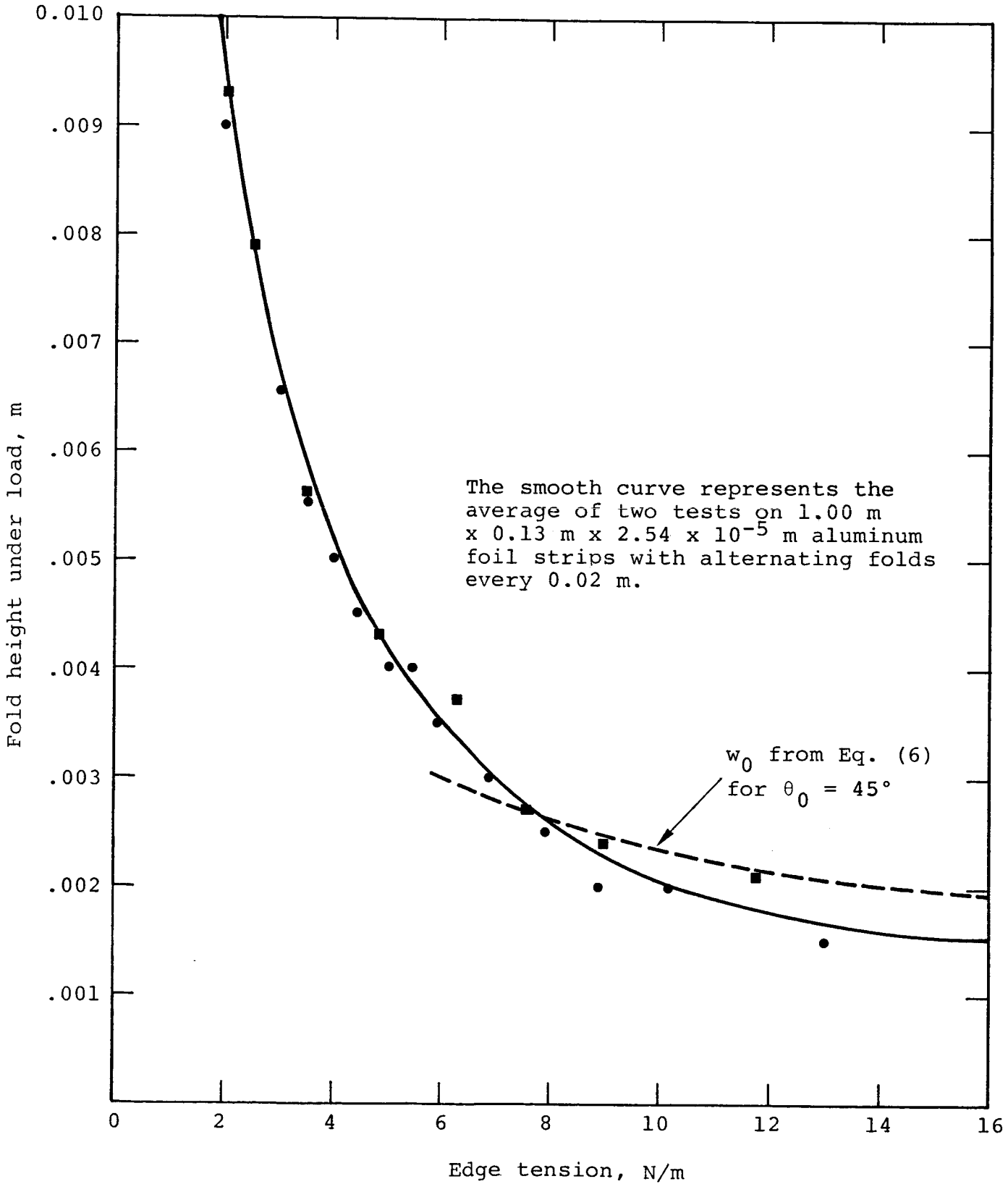


Figure 5. Fold height of folded foil under tension.

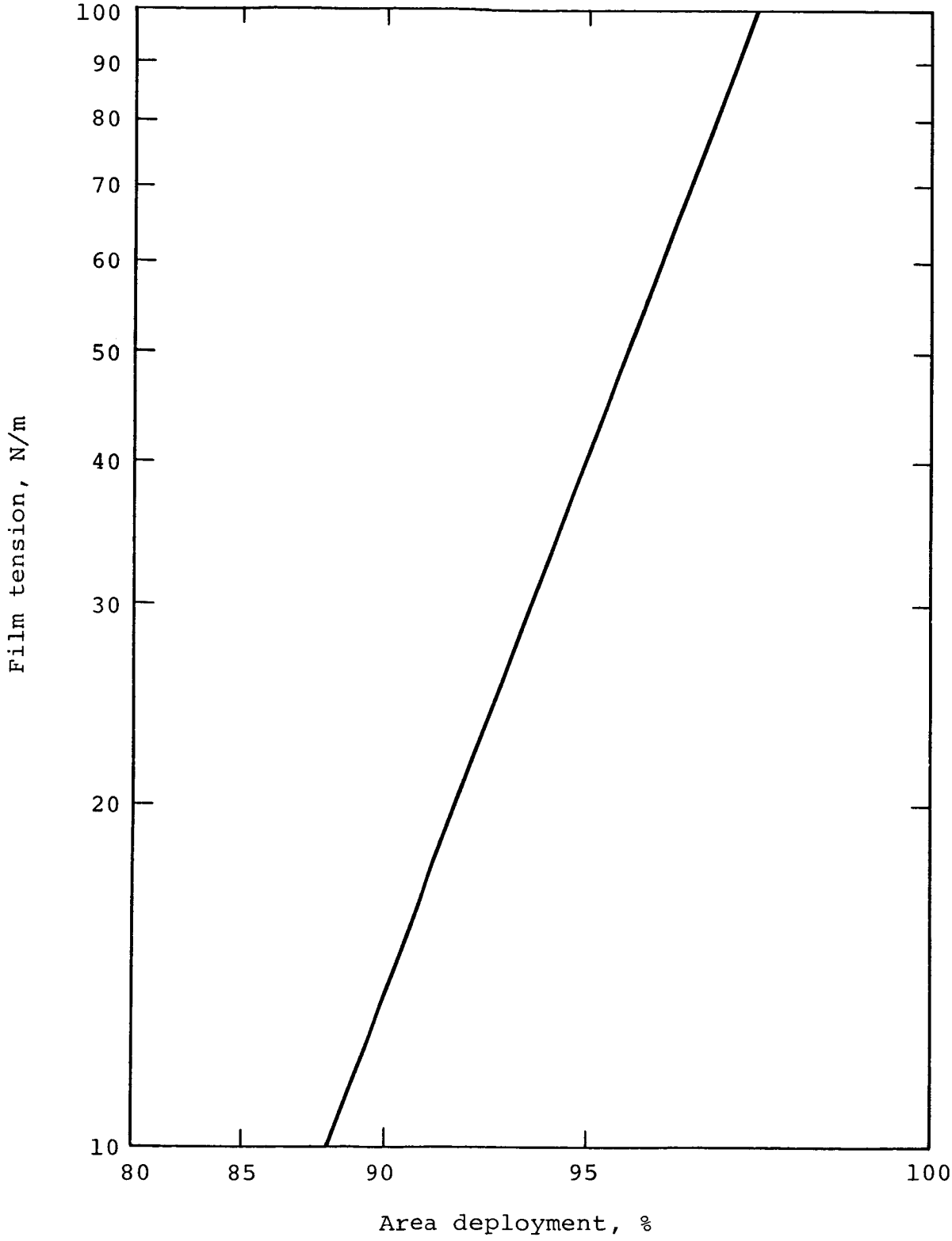


Figure 6. Deployment of a foil surface folded in two directions.

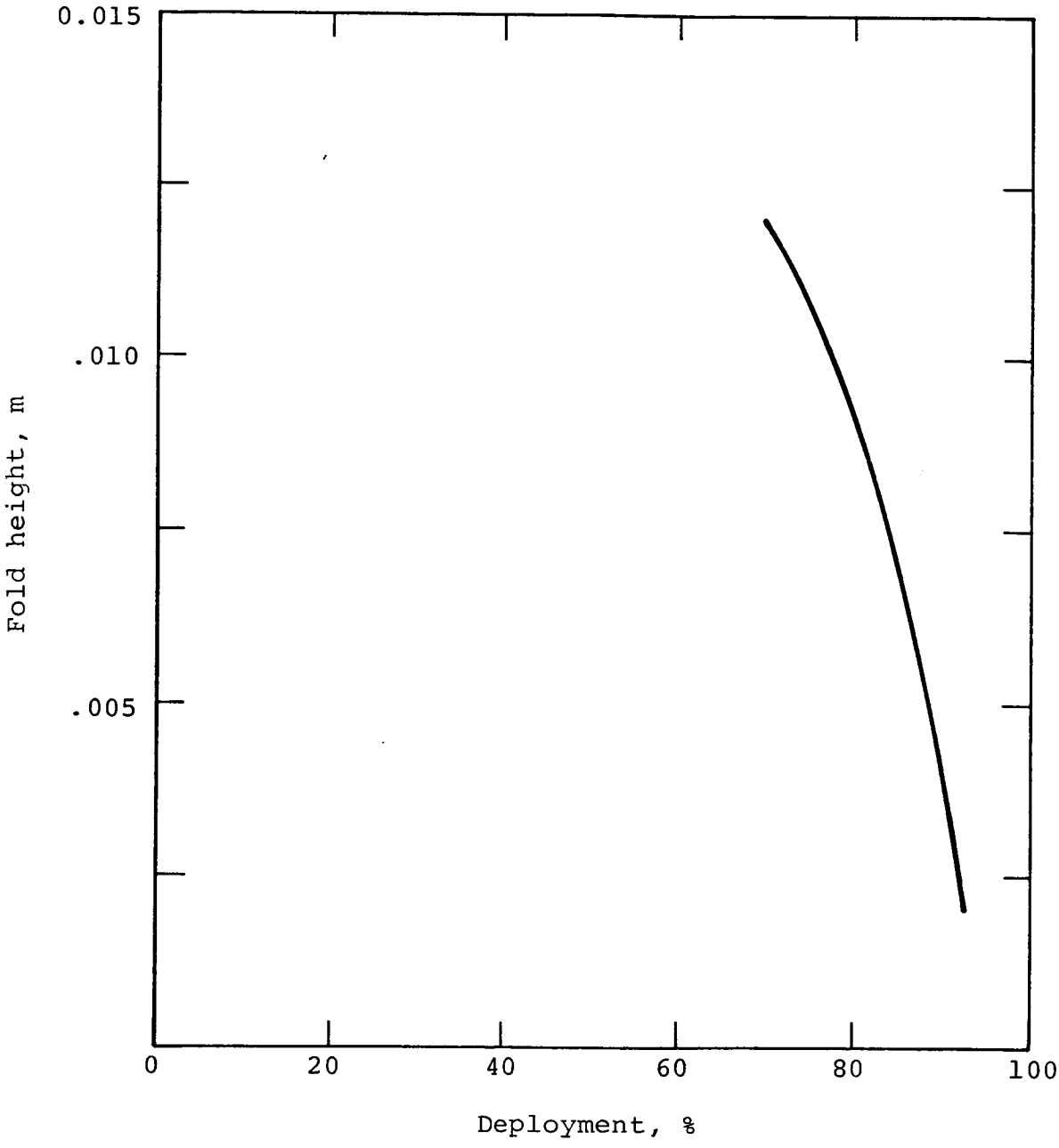


Figure 7. Deployment of a foil surface folded in two directions.

APPENDIX A

TESTS ON ALUMINUM FOIL STRIPS WITH ALTERNATING PARALLEL FOLDS

Three identical tests were performed on two separate occasions to study the effects folds have on deploying or unfolding a folded foil surface. The test consisted of a strip of aluminum foil 0.1-m wide and 1.2-m long. A series of 50 2-cm-wide folds were made in the center leaving 0.1 m at both ends for handling purposes (see Figures A-1 and A-2). After all 50 folds were accurately made, the folded strip was placed in a vise and the folds set. The test was performed on a flat Formica table top dusted with talc powder to reduce friction. One end of the strip was firmly fixed by masking tape and the opposite end had a large paper clip anchor folded and applied so as to distribute the applied tension load evenly over the width of the strip (see Figures A-1 and A-3). The loads were applied to a weight hanger on a string which ran over a pulley to the anchor on the aluminum strip. The length measured was from the first fold to the last fold. At each load case, the load was gently applied and the table top vibrated so as to allow the strip to overcome any friction in the system and extend to an equilibrium point. The length was measured and recorded as the loaded extension (see Table A-1). The load was then removed and the table vibrated to allow the strip to contract. The length, fold height, and fold angle were measured and recorded under load-relieved values (see Table A-1).

In the first test, starting at about Load Case No. 19 or 20 and continuing on all subsequent load cases, an interesting phenomenon occurred when the load was removed. The folds, instead of retracting in the manner it was originally folded, folded in the opposite direction (see Figures A-4 and A-5). Unfortunately, it was not noticed until Load Case No. 21. This phenomenon probably accounts for the anomaly at the bottom of the percent relative

contraction versus percent elongation (loaded) graph shown in Figure A-6. After Load Case No. 24, a roller was used to flatten the foil to remove any remaining creases. This measured length was found to be approximately 0.0005 m shorter than the original value.

The recorded data was used to calculate the load (in Newtons), the percent extension (loaded), the percent relative contraction, percent extension (loaded) squared, and the effective load. These results are shown in Table A-2. Figures A-6 and A-7 provide a graphic presentation of selected data.

Two additional tests were performed which were identical to the first 1-D loading aluminum foil fold test. The test was repeated in order to obtain additional data not recorded during the first test and to check repeatability of the test.

The test setup (see Figure A-3) and procedure were identical to the original test. A new strip of aluminum foil was prepared in order to avoid any possible strain-hardening effects of the first strip on the data.

At each load case, the weight was gently lowered and the strip allowed to extend to an equilibrium point. The table was vibrated to allow the strip to overcome any friction. The loaded extension (first to last fold), fold height, and angle were measured and recorded (see Tables A-3 and A-4 and Figures A-4, and A-8 through A-11). The load was then removed and the strip allowed to contract. Again, the table was vibrated. The load-relieved extension, fold height, and angle were measured and recorded (see Tables A-5 and A-6).

At Load Case No. 8, it was found that the data needed on the fold angle was that of the fold tip and not that of the sides as was being recorded (see Figure 1 in main text). From Load Case No. 9 and on, the fold tip angle was recorded as noted with the data (see Tables A-4 and A-6).

While lowering the weight at Load Case No. 15, the weight was accidentally dropped and pulled the strip further than the static load would have. Subsequently, the weight was increased to where the load extended the strip beyond the dynamic extension. As a result, the data at several loads previously planned for were not obtained. The test was continued as normal from then on. The recorded data was used to calculate the effective load, the percent extension (loaded), the average fold angle (loaded), and the average fold height (loaded) (see Table A-7). As a result of these two abnormalities, it was decided to repeat the test. The same foil strip was refolded and tested again (see Table A-8).

In the second test, five preselected random folds were used to obtain data on the fold height and angle. It was originally hoped to obtain better representative data. Though the five folds did not necessarily represent an average of the 50 folds, some were very irregular and uneven. As a result, in the third test the fold height was the average of all the folds and the fold angle was obtained from that fold which best approaches the average fold angle (see Table A-8). In addition, the load-relieved fold height and fold angle were not recorded as was done in the second test because they were not needed. The recorded data was used to calculate the effective load and percent extension (loaded) (see Table A-9). Figure A-12 shows the fold height graphed against the percent extension at the last 10 percent of deployment using data obtained from the third test.

TABLE A-1. Al STRIP, 1-D LOADING, FIRST TEST, RECORDED DATA: LOAD, LOADED EXTENSION, AND LOAD RELIEVED EXTENSION ANGLE AND HEIGHT

LOAD CASE	LOAD WEIGHT (g)	LOADED EXTENSION (m)	LOAD RELIEVED EXTENSION (m)	LOAD RELIEVED	
				ANGLE (°)	HEIGHT (m)
1	0	0.0095	0.0095	---	0.020
2	1.91	0.1200	0.0350	---	0.020
3	3.83	0.1980	0.0525	4	0.020
4	5.74	0.2920	0.0935	6	0.020
5	7.65	0.3845	0.1385	7	0.020
6	9.56	0.4890	0.2360	15	0.0195
7	11.48	0.6585	0.4185	29	0.0195
8	13.39	0.7745	0.5570	36	0.0150
9	15.30	0.7925	0.6175	43	0.0145
10	17.21	0.8130	0.6535	48	0.0140
11	19.13	0.8300	0.6780	50	0.0135
12	21.04	0.8635	0.7480	57	0.0115
13	22.95	0.8695	0.7540	60	0.0105
14	29.01	0.8885	0.7865	63	0.0095
15	42.72	0.9170	0.8465	68	0.0080
16	56.43	0.9320	0.8880	72	0.0070
17	70.14	0.9410	0.9095	75	0.0065
18	97.56	0.9530	0.9385	85	0.0055
19	152.40	0.9660	0.9585	88	0.0035
20	256.43	0.9770	0.9685	88	0.0025
21	407.24	0.9845	0.9735	89	0.0015
22	607.24	0.9895	0.9765	*	0.0010
23	1107.24	0.9945	0.9815	*	*
24	1542.24	0.9965	0.9860	*	*

*Data not measurable for this case.

TABLE A-2. Al STRIP, 1-D LOADING, FIRST TEST, CALCULATED FROM DATA: LOAD, PERCENT EXTENSION (LOADED), PERCENT RELATIVE CONTRACTION, PERCENT EXTENSION (LOADED) SQUARED, AND EFFECTIVE LOAD

LOAD CASE	LOAD (N)	EXTENSION (LOADED)* (%)	RELATIVE CONTRACTION (%)	EFFECTIVE LOAD (N/m)	EXTENSION (LOADED) SQUARED (%)
1	0.0187	0.95	0.0	0.0	0.009
2	0.0187	12.00	70.83	0.187	1.44
3	0.0376	19.80	73.48	0.376	3.92
4	0.0563	29.20	67.98	0.565	8.53
5	0.0750	38.45	63.98	0.750	14.78
6	0.0938	48.90	51.74	0.940	23.91
7	0.113	65.85	36.45	1.130	43.36
8	0.131	77.45	28.08	1.310	59.99
9	0.150	79.25	22.08	1.50	62.81
10	0.169	81.30	19.62	1.69	66.10
11	0.188	83.00	18.31	1.88	68.89
12	0.206	86.35	13.38	2.06	74.56
13	0.225	86.95	13.28	2.25	75.60
14	0.285	88.85	11.48	2.85	78.94
15	0.419	91.70	7.69	4.19	84.09
16	0.553	93.20	4.72	5.55	86.86
17	0.688	94.10	3.35	6.90	88.55
18	0.957	95.30	1.52	9.55	90.82
19	1.49	96.60	0.75	14.9	93.32
20	2.51	97.70	0.85	25.1	95.45
21	3.99	98.45	1.12	39.9	96.92
22	5.96	98.95	1.31	59.6	97.91
23	10.9	99.45	1.31	109	98.90
24	15.1	99.65	1.05	151	99.30

*L_F = 0.9995 m (measurement taken after foil was rolled flat)

TABLE A-3. Al STRIP, 1-D LOADING, SECOND TEST, RECORDED DATA: LOAD, LOADED EXTENSION, AND FOLD HEIGHT (LOADED)

LOAD CASE	LOAD (g)	LOADED EXTENSION (m)	FOLD HEIGHT (LOADED) (m) (five random folds)				
			FOLD #3	FOLD #15	FOLD #25	FOLD #29	FOLD #43
1	2.1	0.042	0.0205	0.020	0.020	0.020	0.020
2	3.8	0.125	0.021	0.0195	0.0195	0.020	0.0195
3	5.5	0.208	0.020	0.0195	0.0195	0.0195	0.0195
4	10.5	0.504	0.017	0.0175	0.017	0.0175	0.017
5	15.6	0.735	0.0125	0.0130	0.012	0.0125	0.0125
6	20.6	0.846	0.009	0.010	0.009	0.009	0.0095
7	25.6	0.872	0.0075	0.0085	0.0075	0.008	0.008
8	35.6	0.907	0.0055	0.0060	0.0055	0.0055	0.0055
9	49.6	0.932	0.005	0.0045	0.0040	0.004	0.004
10	63.8	0.942	0.004	0.0035	0.003	0.0035	0.003
11	77.9	0.951	0.0035	0.002	0.0025	0.0025	0.0025
12	92.0	0.955	0.0035	0.002	0.0020	0.002	0.0025
13	120.3	0.961	0.003	0.002	0.0015	0.0015	0.0025
14	162.9	0.967	0.0025	0.002	0.001	0.001	0.0015
15	653.2	0.991	0.0005	0.001	0.0005	0.0005	0.001
16	1524.6	0.994	*	*	*	*	*
17	2386.3	0.998	*	*	*	*	*

*Too small to measure.

TABLE A-4. Al STRIP, 1-D LOADING, SECOND TEST, RECORDED DATA: FOLD ANGLE (LOADED)

LOAD CASE	FOLD ANGLE (LOADED) (°) (five random folds)				
	FOLD #3	FOLD #15	FOLD #25	FOLD #29	FOLD #43
1	0.0	0.0	0.0	0.0	0.0
2	15	8	10	9	0.0
3	16	8	10	9	8
4	40	32	34	33	35
5	60	55	60	60	60
6	72	70	75	76	73
7	80	75	78	77	75
8	85	82	85	85	82
9	23	0	37	30	10
10	25	30	30	30	15
11	25	35	30	30	20
12	25	40	32	30	20
13	28	43	35	30	20
14	28	50	45	30	25
15	60	75	75	45	68
16	65	80	90	85	80
17	90	90	90	90	90

Note: Load Cases 1 through 8 show average angle; Load Cases 9 through 17 show tip angle. Estimated accuracy ±5°.

TABLE A-5. Al STRIP, 1-D LOADING, SECOND TEST, RECORDED DATA: LOAD RELIEVED EXTENSION AND FOLD HEIGHT (LOAD RELIEVED)

LOAD CASE	LOAD RELIEVED EXTENSION (m)	FOLD HEIGHT (LOAD RELIEVED) (m) (five random folds)				
		FOLD #3	FOLD #15	FOLD #25	FOLD #29	FOLD #43
1	0.017	0.020	0.020	0.020	0.020	0.020
2	0.027	0.020	0.020	0.020	0.020	0.020
3	0.047	0.020	0.020	0.0195	0.0195	0.0195
4	0.254	0.0195	0.019	0.019	0.019	0.0195
5	0.521	0.016	0.0165	0.016	0.017	0.017
6	0.711	0.013	0.0135	0.0135	0.0135	0.013
7	0.760	0.012	0.0125	0.0125	0.013	0.0125
8	0.854	0.0115	0.006	0.010	0.0105	0.010
9	0.897	0.010	0.008	0.0065	0.009	0.008
10	0.924	0.009	0.0025	0.0055	0.0055	0.006
11	0.930	0.0085	0.0025	0.005	0.0065	0.0055
12	0.938	0.008	0.0025	0.004	0.0055	0.004
13	0.948	0.0075	0.0025	0.003	0.0045	0.003
14	0.956	0.0005	0.001	0.001	0.0005	0.0005
15	0.983	*	0.0005	0.0005	*	*
16	0.983	*	0.0005	*	*	*
17	0.987	*	*	*	*	*
18	0.9995†	*	*	*	*	*

*Data not measurable for this case
†Measurement taken after foil was rolled flat.

TABLE A-6. Al STRIP, 1-D LOADING, SECOND TEST, RECORDED DATA: FOLD ANGLE (LOAD RELIEVED)

LOAD CASE	FOLD ANGLE (LOAD RELIEVED) (°) (five random folds)				
	FOLD #3	FOLD #15	FOLD #25	FOLD #29	FOLD #43
1	0.0	0.0	0.0	0.0	0.0
2	0.0	4	0.0	5	2
3	2	4	0.0	6	4
4	20	14	15	15	16
5	42	40	40	38	35
6	55	55	58	58	60
7	62	55	60	62	60
8	68	73	68	65	65
9	15	5	10	30	5
10	17	40	30	30	10
11	20	40	30	30	15
12	20	40	30	30	15
13	20	42	32	30	17
14	40	60	55	50	45
15	60	68	65	50	60
16	65	70	90	50	65
17	90	90	90	90	90

Note: Load Cases 1 through 8 show average angle; Load Cases 9 through 17 show tip angle. Estimated accuracy ±5°.

TABLE A-7. Al STRIP, 1-D LOADING, SECOND TEST, CALCULATED FROM DATA: EFFECTIVE LOAD, PERCENT EXTENSION (LOADED), AVERAGE FOLD ANGLE (LOADED), AND AVERAGE FOLD HEIGHT (LOADED).

LOAD CASE	EFFECTIVE LOAD (N/m)	EXTENSION (LOADED) (%)	AVERAGE FOLD ANGLE (LOADED) (°)	AVERAGE FOLD HEIGHT (LOADED) (m)
1	0.21	4.2	0.0	0.020
2	0.37	12.5	8	0.020
3	0.54	20.8	10	0.0195
4	1.03	50.4	35	0.017
5	1.53	73.5	60	0.0125
6	2.02	84.6	73	0.0095
7	2.51	87.2	77	0.008
8	3.49	90.7	84	0.0055
9	4.86	93.2	20	0.0045
10	6.26	94.2	26	0.0035
11	7.64	95.1	28	0.0025
12	9.02	95.5	29	0.0025
13	11.80	96.1	31	0.002
14	15.98	96.7	53	0.0015
15	64.06	99.1	65	0.001
16	149.52	99.4	80	<0.0005
17	234.02	99.8	⩽90	<0.0005

Note: Load Cases 1 through 8 show average angle; Load Cases 9 through 17 show tip angle. Estimated accuracy ±5°.

TABLE A-8. Al STRIP, 1-D LOADING, THIRD TEST, RECORDED DATA: LOAD, LOADED EXTENSION, FOLD ANGLE (LOADED), FOLD HEIGHT (LOADED), AND LOAD RELIEVED EXTENSION.

LOAD CASE	LOAD (g)	LOADED EXTENSION (m)	FOLD ANGLE (LOADED) (°)	FOLD HEIGHT (LOADED) (m)	LOAD RELIEVED EXTENSION (m)
1	10.5	0.482	4	0.017	0.263
2	20.5	0.835	7	0.009	0.664
3	30.5	0.889	8	0.0065	0.772
4	35.5	0.903	9	0.0055	0.803
5	40.4	0.914	9	0.005	0.827
6	45.3	0.925	12	0.0045	0.856
7	50.3	0.930	15	0.004	0.868
8	55.2	0.935	15	0.004	0.884
9	60.1	0.939	17	0.0035	0.893
10	70.1	0.944	20	0.003	0.907
11	80.1	0.949	22	0.0025	0.922
12	90.1	0.953	22	0.002	0.930
13	104.2	0.957	25	0.002	0.941
14	132.6	0.962	28	0.0015	0.950
15	175.2	0.968	30	0.001	0.960
16	237.0	0.975	35	0.0005	0.968
17	308.9	0.980	45	0.0005	0.973
18	422.6	0.985	50	<0.0005	0.977
19	536.2	0.989	60	<0.0005	0.979
20	763.4	0.992	60	<0.0005	0.981
21	1199.4	0.995	67	<0.0005	0.985
22	1628.1	0.997	67	<0.0005	0.989
23	2057.2	0.9975	80	<0.0005	0.992
24	2489.3	0.998	85	<0.0005	0.992
25	4978.6	0.9985	~90	<0.0005	0.993

TABLE A-9. Al STRIP, 1-D LOADING, THIRD TEST, CALCULATED FROM DATA: EFFECTIVE LOAD AND PERCENT EXTENSION (LOADED)

LOAD CASE	EFFECTIVE LOAD (N/m)	EXTENSION (LOADED) (%)
1	1.03	48.2
2	2.01	83.5
3	2.99	88.9
4	3.48	90.3
5	3.96	91.4
6	4.44	92.5
7	4.93	93.0
8	5.41	93.5
9	5.89	93.9
10	6.87	94.4
11	7.86	94.9
12	8.84	95.3
13	10.22	95.7
14	13.00	96.2
15	17.18	96.8
16	23.24	97.5
17	30.29	98.0
18	41.44	98.5
19	52.59	98.9
20	74.87	99.2
21	117.63	99.5
22	159.67	99.7
23	201.75	99.75
24	244.13	99.8
25	488.25	99.85

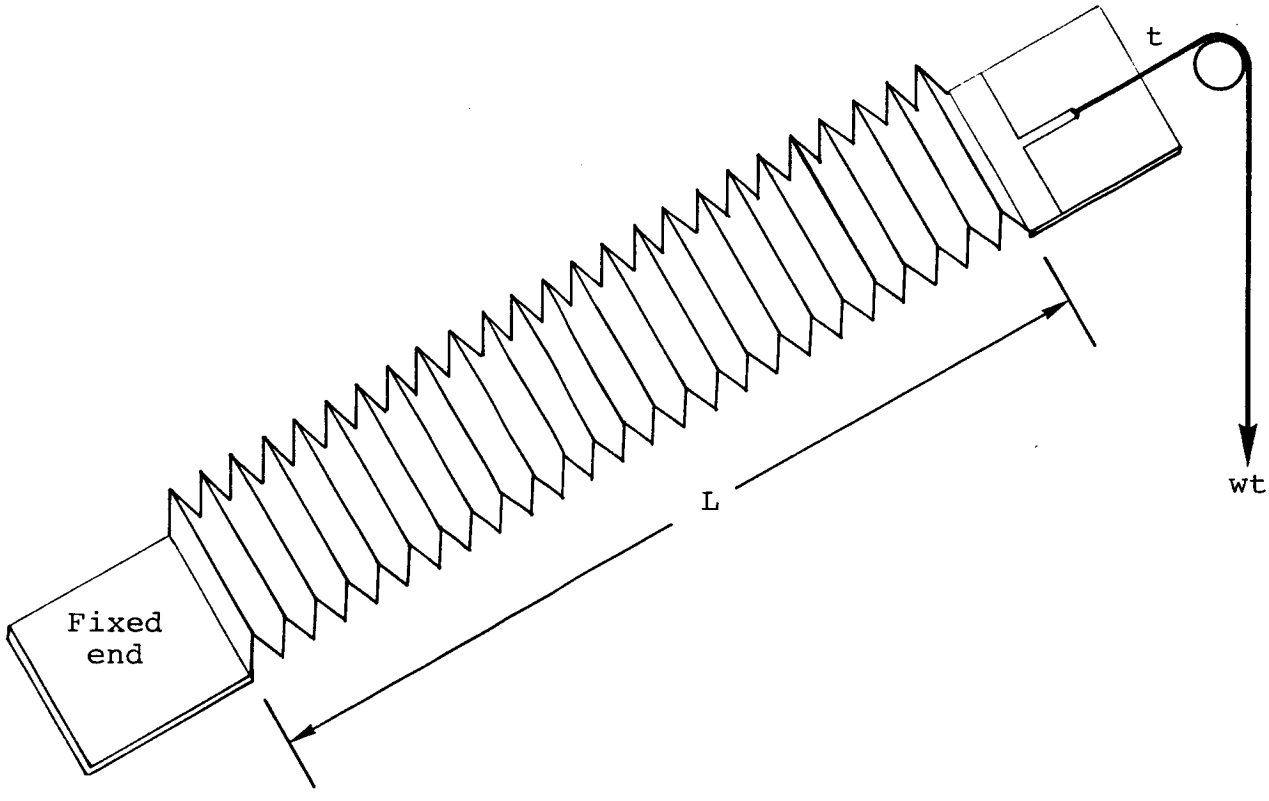


Figure A-1. Test setup and aluminum strip specifications.

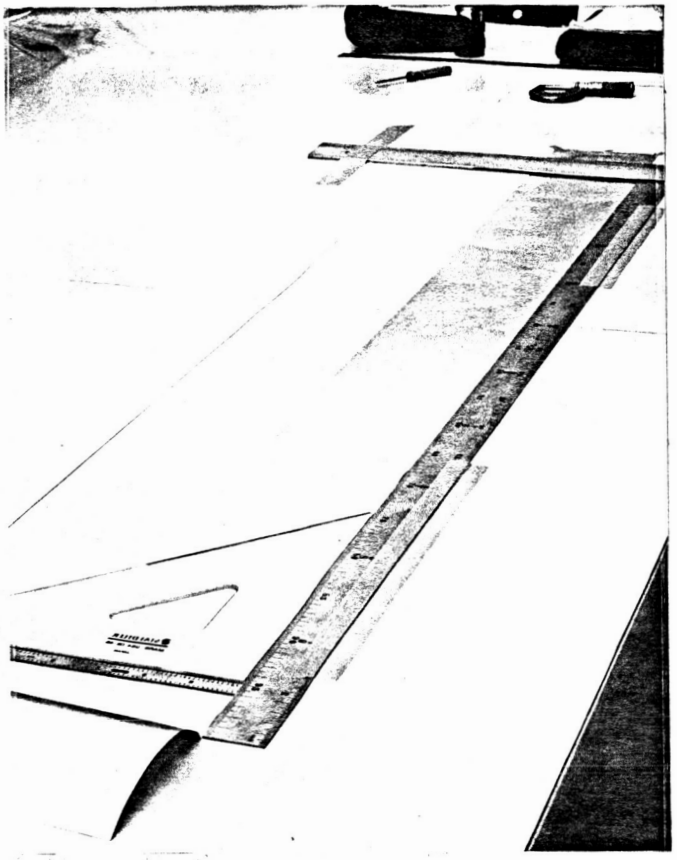


Figure A-2. Setting folding guides in aluminum strip.

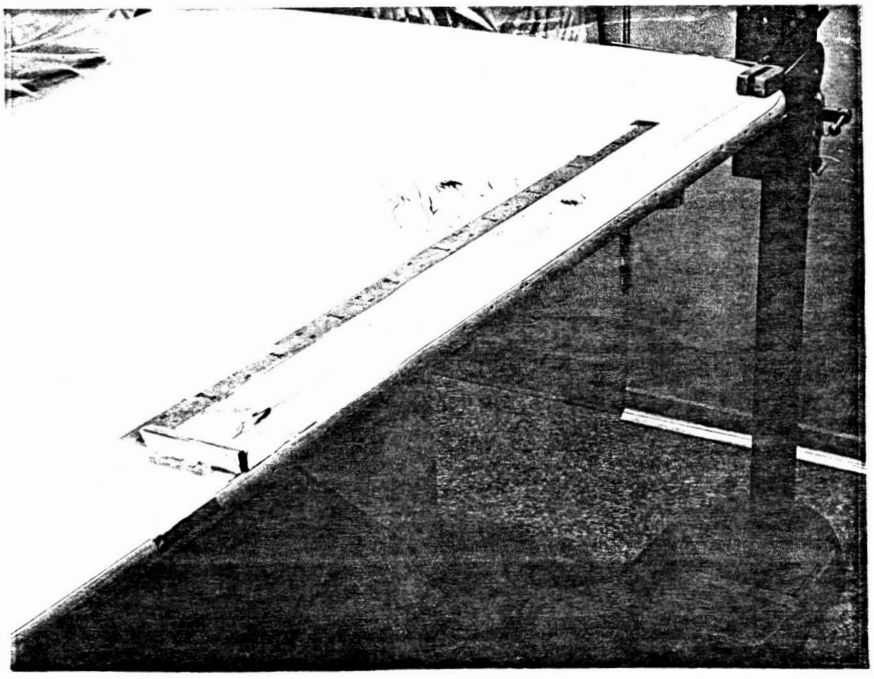


Figure A-3. Test setup, no load.

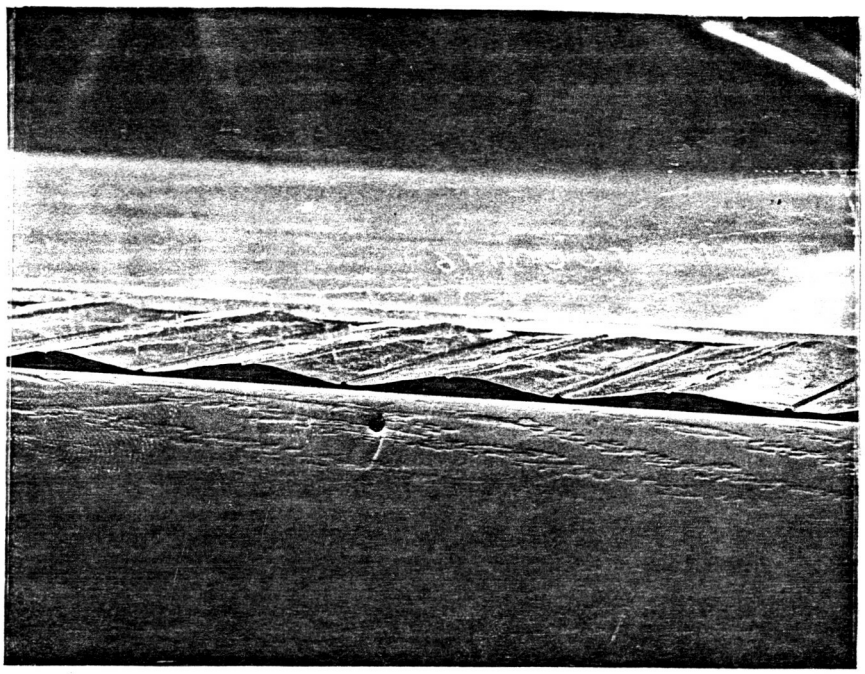


Figure A-4. Load Case No. 14 (load relieved) (note reverse retraction) (Test No. 2).

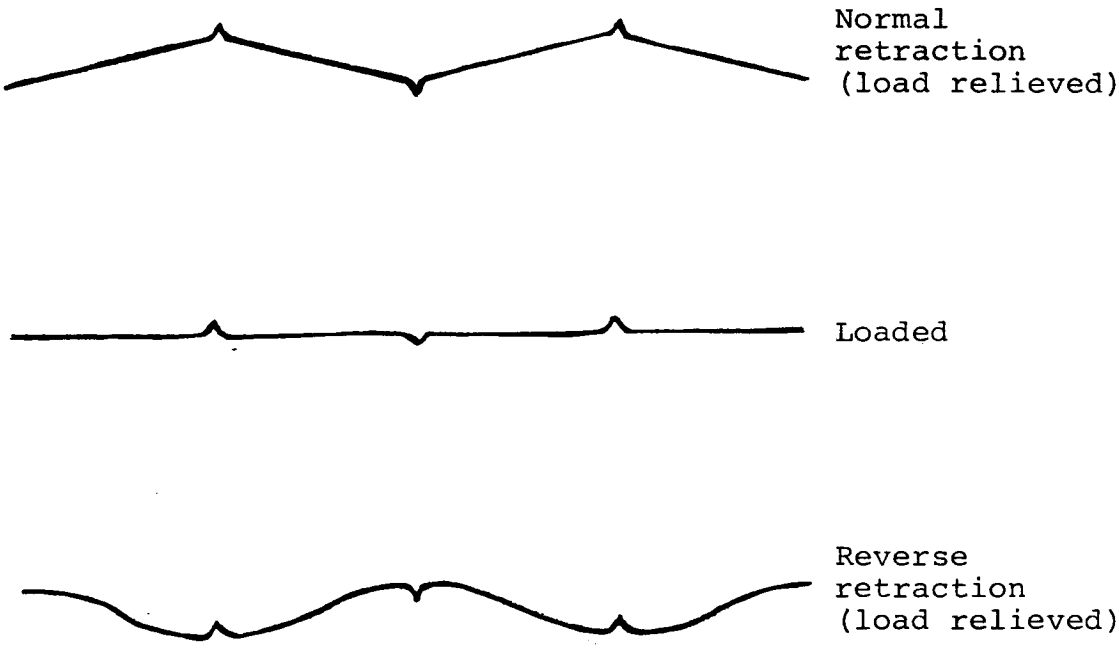


Figure A-5. Illustration of reverse retraction which occurred at high loads when load relieved (see also Figure A-4).

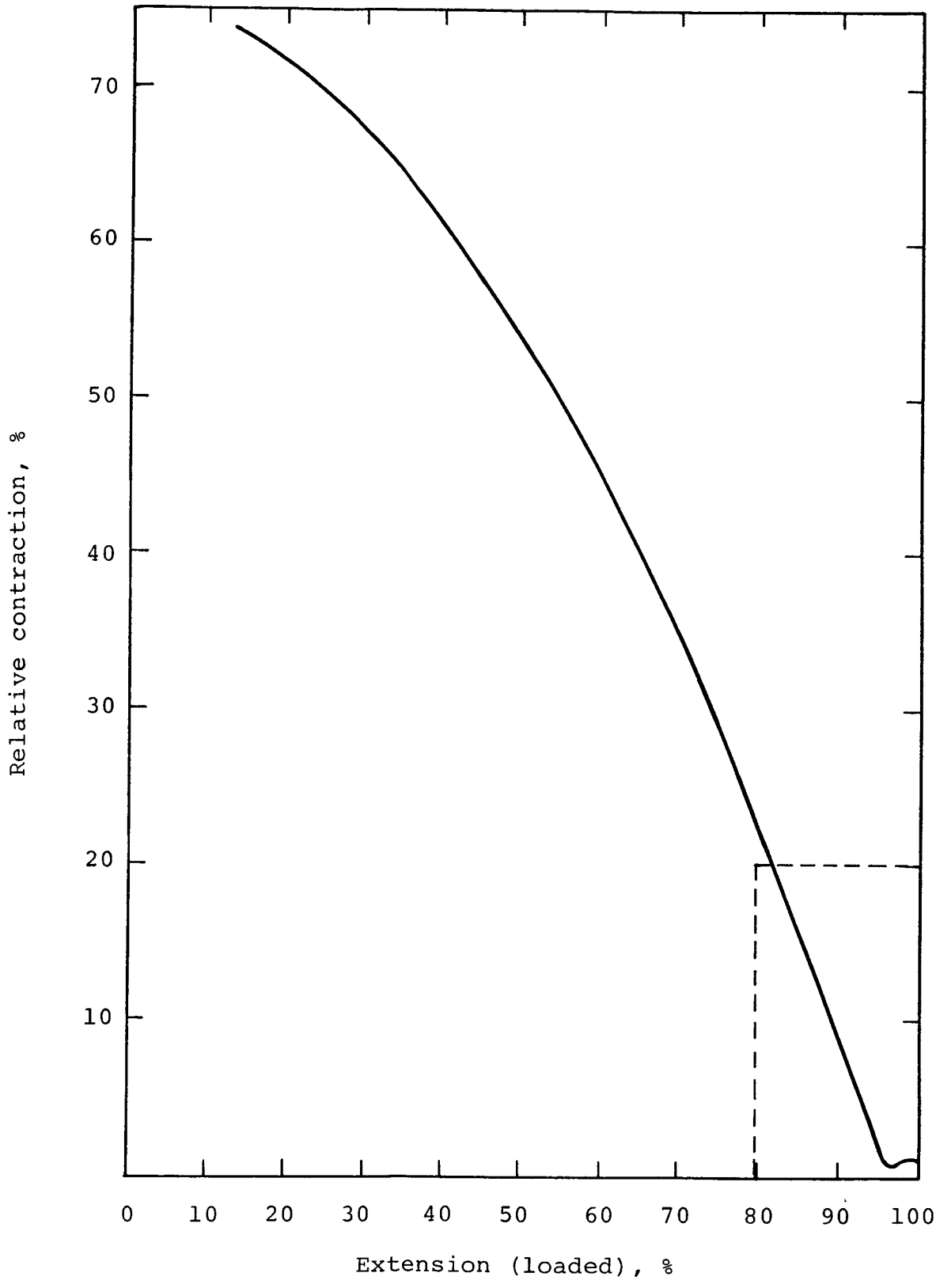


Figure A-6. Percent relative contraction vs. percent extension (loaded)(from data of first test).

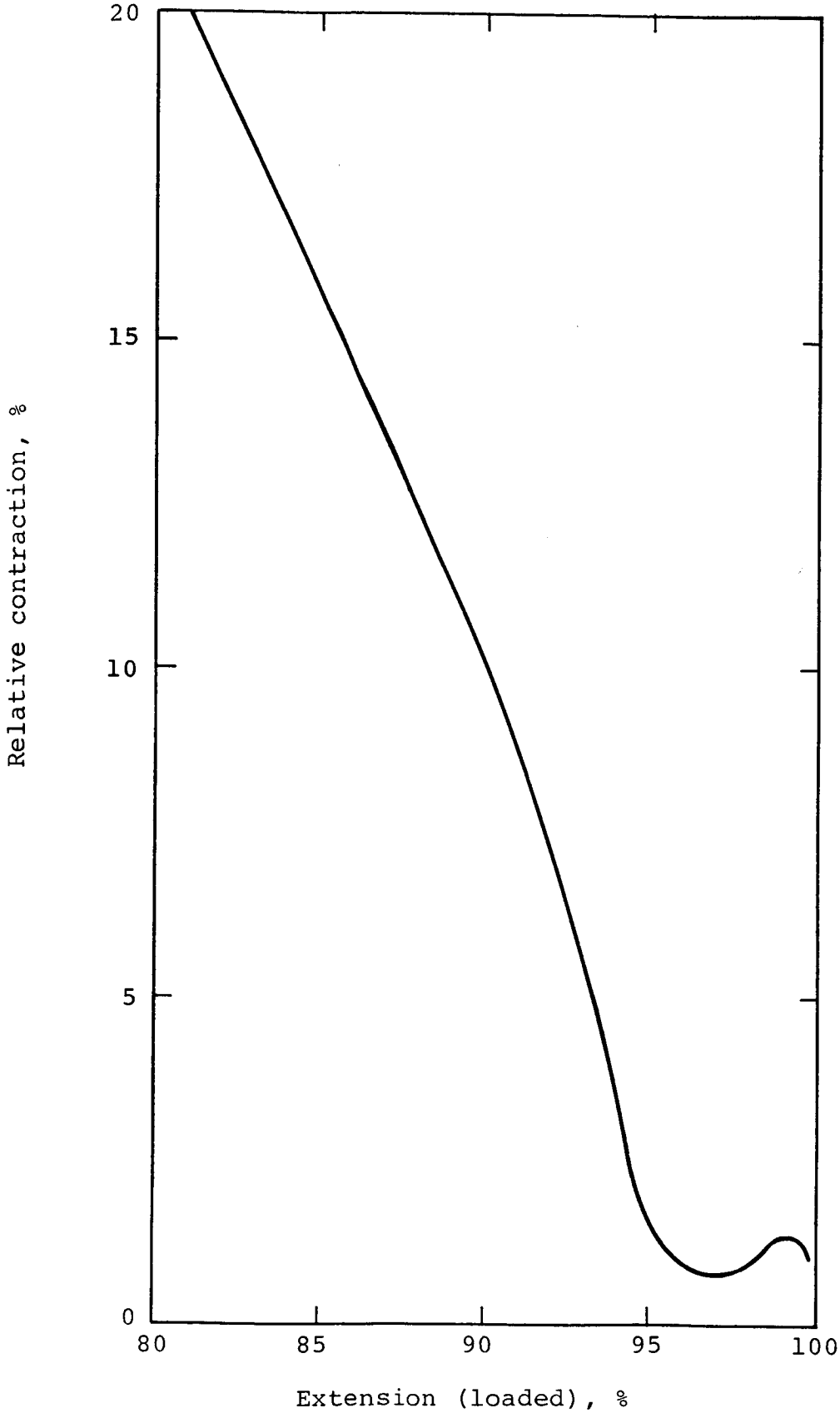


Figure A-7. Percent relative contraction vs. percent extension (loaded) (from data of first test).

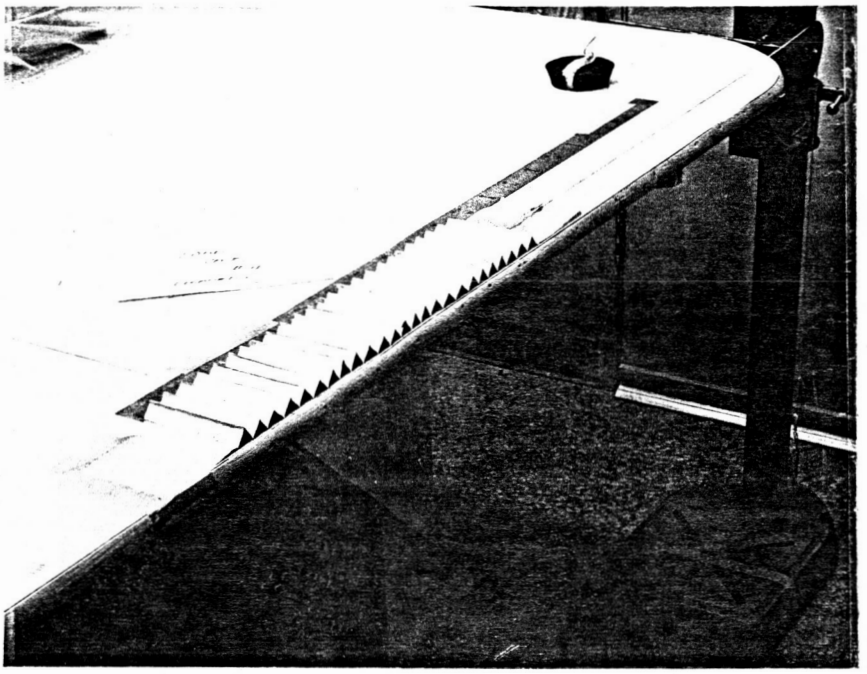


Figure A-8. Load Case No. 4 (loaded) (Test No. 2).

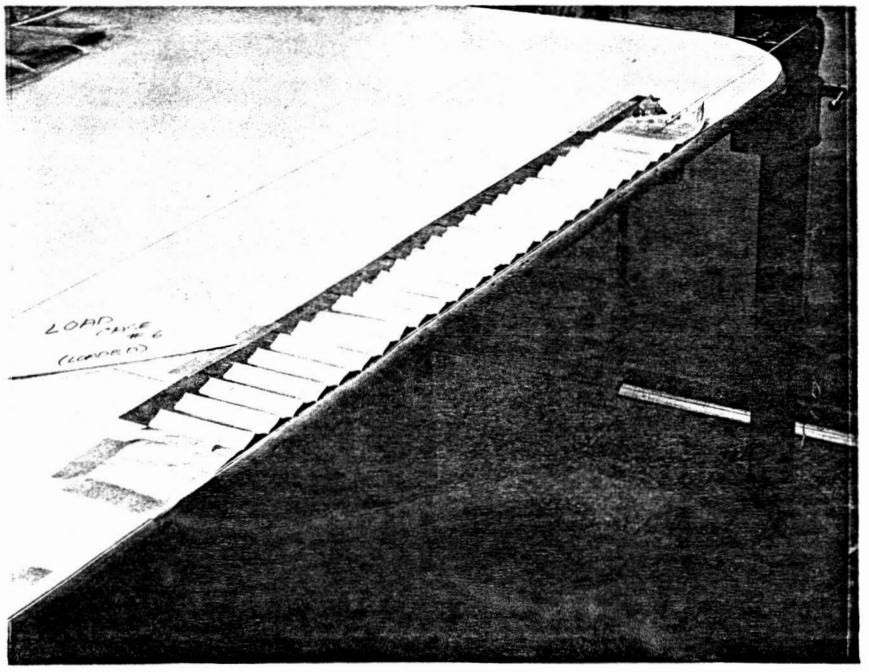


Figure A-9. Load Case No. 6 (loaded) (Test No. 2).

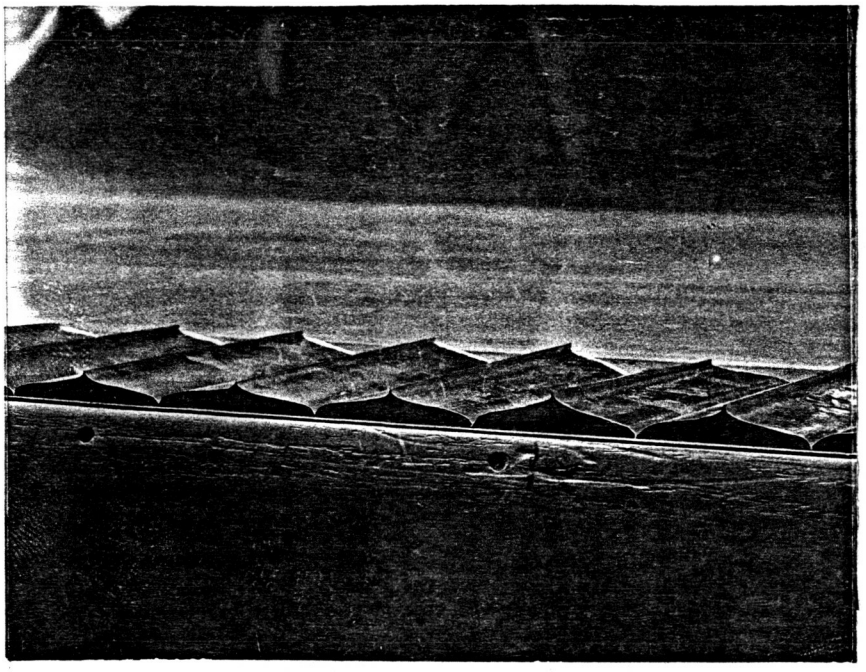


Figure A-10. Load Case No. 7 (loaded). (Test No. 2).

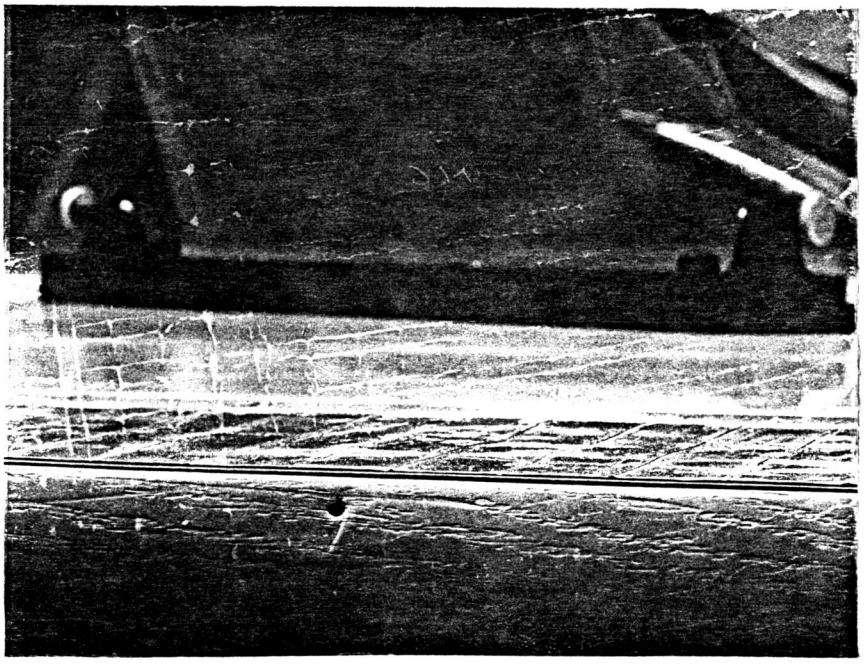


Figure A-11. Load Case No. 15 (loaded). (Test No. 2).

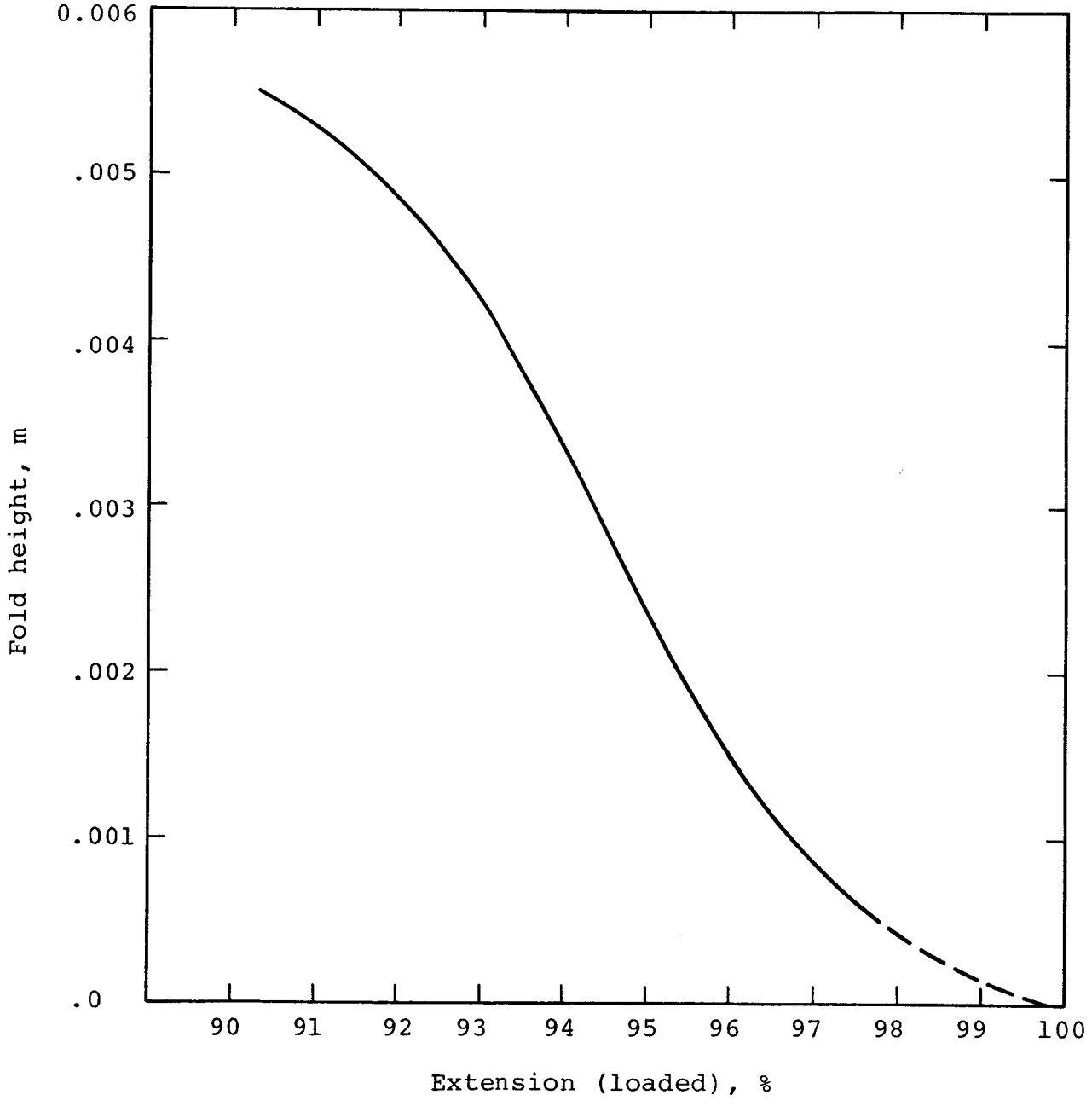


Figure A-12. Fold height vs. percent extension (loaded) (from data of third test).

APPENDIX B

TEST ON A SQUARE FOIL SURFACE WITH FOLDS IN TWO DIRECTIONS

The test sample used in these 2-D loading tests consisted of a square sheet of aluminum foil with 18.0-inch-long sides. The material is of the same type used in the 1-D loading tests (see Appendix A). From this square, catenaries were cut in each side so the total area removed was 10 percent of the area of the original square (see Figure B-1). A series of 0.25-inch-wide mylar tabs were fixed 2.0 cm apart on each of the four catenaries and a nylon cord was threaded through the tabs (see Figures B-2 and B-3). A sleeve made of glass tape was wrapped around the two cords at each corner in order to keep the cords parallel to the catenaries at the corners.

The manner in which the foil was folded was designed to best approach a typical folding pattern used in an actual application. The goal was to obtain a high-density, stowed package and a deployment with no or little angular momentum being generated. This folding method will work equally well with a triangular surface. The folding guides were measured and creased by folding the square into a quarter section and then folding that over a straight edge. The folds were spaced 2.0 cm apart creating 10 folds between the center and the edge. Once the folding guides were made and the surface unfolded back into a square, the foil was folded as shown in Figures B-4 through B-7).

The loads were applied to the catenaries by way of the cords. The final stowed configuration was placed on a table with a pulley at each corner over which the cords passed connected to weight hangers (see Figure B-8). For each load case, a small increment of weight was applied to the cords and the table was vibrated to remove any friction with the foil sheet or in the pulleys. After the foil had reached an equilibrium point, the length between

the center and each of the corners was measured (see Table B-1) and a tracing of the outer perimeter of the surface was made. From this tracing, a planimeter was used to find the deployed area. From the data in Table B-1, the load, average length, and percent total length deployment were calculated (see Table B-2).

Upon initial loading, the "arms" unrolled to most of their full length before the main body of the foil surface unfolded (see Figures B-9 and B-10). Beginning with Load Case No. 7, the foil surface had taken a shape so that an approximate radius of the sides could be obtained (see Figures B-11 through B-16). Using the radius and the segment height, the area of the segment could be calculated. From this, the deployed surface area is found and averaged with the area using the planimeter (see Table B-3).

After the final load case, No. 17, a roller was used to flatten the foil to remove any remaining creases and a tracing was made.

A second test was performed which was similar to the first 2-D loading test to obtain information on fold/wrinkle height not recorded during the first test. The test setup was similar to that used in the first test except larger pulleys with ball bearings were used and the test was performed on the surface table (see Figure B-17). The original sheet of aluminum foil was refurbished by replacing about 25 torn tabs and three out of the four corners. Before folding, the foil sheet was rolled flat, but still contained some 0.005-inch-high wrinkles from its previous use. The sheet showed signs of wear and as a result it was not possible to load it to the higher loads used in the first test.

At each load case, the weights were gently applied and the distance from each corner to the center measured and recorded (see Table B-4). To measure the fold/wrinkle height, a platform measuring 5.45 inches by 4.45 inches was set at a height such that when placed under the sheet it slightly pushed it up. This height was accurately measured. The platform was placed between two corners with one edge along the side of the sheet. A clear plexiglass disc was placed on the foil sheet above the platform. The

height was measured at two points 1 inch to either side of center and 2.75 inches in from the side. The thickness of the disc was subtracted and the height recorded (see Table B-5). This was performed at two opposite quadrants (see Figure B-18).

While folding the sheet, it was decided not to coil up the four "arms" at the last stage of folding (see Figures B-6 and B-7). This was done in order to reduce wear and tear. As a result of this, while deploying the surface, an opposing fold pattern developed perpendicular to each side. The coiling would have allowed the foil surface to deploy without creating the opposing fold pattern. The opposing folds were removed by hand and the test was continued.

It was originally intended to use the center-to-corner length to correlate the percent of deployment. Though the length shows little correlation to the load when comparing it to the first test, it was decided to use the load to calculate the percent of deployment (see Table B-6). A possible explanation of this abnormality with the length is that the corners are not the natural corners of the aluminum foil sheet. The corners are made with mystic Kapton tape.

TABLE B-1. SQUARE FOIL SURFACE, 2-D LOADING, RECORDED DATA: TENSION LOAD AND CENTER-TO-CORNER LENGTH

LOAD CASE	TENSION LOAD, 2T (g)	CENTER-TO-CORNER LENGTH (in.)			
		L_1	L_2	L_3	L_4
1	0.0	2.2	2.5	2.3	2.0
2	5.5	2.4	2.65	2.3	2.0
3	19.8	2.7	2.8	2.6	2.15
4	48.4	3.45	3.2	3.95	3.6
5	77.0	5.1	5.75	6.5	4.4
6	132.2	7.45	8.4	8.2	7.95
7	245.6	10.0	9.9	10.05	10.25
8	359.0	10.85	10.8	11.0	11.05
9	472.4	11.45	11.4	11.3	11.4
10	699.2	11.7	11.75	11.5	11.6
11	926.0	11.8	11.85	11.55	11.65
12	1358.3	11.95	11.95	11.70	11.80
13	2265	12.05	12.15	11.85	11.90
14	4607	12.1	12.3	12.0	12.1
15	6875	12.15	12.5	12.1	12.2
16	9140	12.2	12.5	12.25	12.25
17	18210	12.25	12.75	12.6	12.45

TABLE B-2. SQUARE FOIL SURFACE, 2-D LOADING, CALCULATED DATA: LOAD, AVERAGE LENGTH, AND PERCENT TOTAL LENGTH DEPLOYMENT

LOAD CASE	LOAD, 2T		AVERAGE LENGTH, L_{AVG} (in.)	DEPLOYMENT LENGTH (% total)
	GRAMS	NEWTONS		
1	0.0	0.0	2.25	17.67
2	5.5	0.054	2.34	18.38
3	19.8	0.194	2.56	20.11
4	48.4	0.475	3.55	27.89
5	77.0	0.755	5.44	42.73
6	132.2	1.297	8.00	62.84
7	245.6	2.409	10.05	78.95
8	359.0	3.521	10.93	85.86
9	472.4	4.633	11.39	89.47
10	699.2	6.857	11.64	91.44
11	926.0	9.081	11.71	91.99
12	1358.3	13.321	11.85	93.09
13	2265	22.21	11.99	94.19
14	4600	45.11	12.13	95.29
15	6875	67.4	12.24	96.15
16	9150	89.7	12.30	96.62
17	18200	178.5	12.51	98.27
			12.54*	
			12.73**	

*Measurement taken after foil was rolled flat.
**Original length before test.

TABLE B-3. SQUARE FOIL SURFACE, 2-D LOADING, CALCULATED FROM DATA: EFFECTIVE LOAD, AREA, RADIUS, AND PERCENT TOTAL AREA DEPLOYMENT

LOAD CASE	EFFECTIVE LOAD, N = T/R (N/m)	AREA (in^2)	RADIUS (in.)	AREA DEPLOYMENT (% total)
1	n/a	n/a	n/a	n/a
2	n/a	2.39	n/a	0.82
3	n/a	2.69	n/a	0.93
4	n/a	2.26	n/a	0.79
5	n/a	3.01	n/a	1.03
6	n/a	14.82	n/a	5.08
7	5.50	54.95	8.61	18.83
8	6.51	93.2	10.65	31.96
9	6.44	142.3	14.17	48.80
10	5.27	209.1	25.6	71.71
11	6.00	222.5	29.8	76.30
12	6.64	240.4	39.5	82.44
13	9.02	255.7	48.5	87.69
14	10.23	264.7	54.7	90.78
15	23.52	270.5	56.5	92.76
16	32.05	274.2	55.1	94.03
17	63.08	281.0	55.7	96.36
		287.4*	58.91*	98.56*
		291.6**	60.19**	100.0**

*Measurement taken after foil was rolled flat.
**Original length before test.

TABLE B-4. SQUARE FOIL SURFACE, 2-D LOADING, FOLD/WRINKLE HEIGHT TEST, RECORDED DATA: TENSION LOAD AND CENTER-TO-CORNER LENGTH.

LOAD CASE	TENSION LOAD, 2T (g)	CENTER-TO-CORNER LENGTH (in.)			
		L_1	L_2	L_3	L_4
1	680.4	12.15	12.45	12.25	12.00
2	1247.4	12.25	12.55	12.45	12.20
3	2827	12.35	12.70	12.45	12.25
4	4536	12.40	12.60	12.50	12.60
5	6804	12.35	12.75	12.50	12.75

TABLE B-5. SQUARE FOIL SURFACE, 2-D LOADING, FOLD/WRINKLE HEIGHT TEST, RECORDED DATA: FOLD/WRINKLE HEIGHT

LOAD CASE	FOLD/WRINKLE HEIGHT (in.)			
	QUADRANT BETWEEN 1 AND 2		QUADRANT BETWEEN 3 AND 4	
	h_1	h_2	h_3	h_4
1	0.433	0.561	0.446	0.511
2	0.376	0.366	0.266	0.408
3	0.178	0.131	0.236	0.274
4	0.138	0.111	0.134	0.133
5	0.100	0.080	0.081	0.074

TABLE B-6. SQUARE FOIL SURFACE, 2-D LOADING, FOLD/WRINKLE HEIGHT TEST, CALCULATED FROM DATA: TENSION LOAD, AVERAGE LENGTH, AVERAGE FOLD/WRINKLE HEIGHT, PERCENT TOTAL AREA DEPLOYMENT BASED ON LOAD AND EFFECTIVE LOAD.

LOAD CASE	TENSION LOAD, 2T		AVG LENGTH, L_{AVG}		AVG HEIGHT, h_{AVG}		AREA DEPLOYMENT* (% total)	EFFECTIVE LOAD (N/m)
	GRAMS	NEWTONS	INCH	METER	INCH	METER		
1	680.4	6.67	12.21	0.3101	0.49	0.012	69.8	5.37
2	1247.4	12.23	12.36	0.3140	0.35	0.0089	80.9	6.48
3	2827	27.72	12.44	0.3160	0.20	0.0051	88.4	10.76
4	4536	44.48	12.53	0.3183	0.13	0.0033	90.7	16.03
5	6804	66.73	12.54	0.3185	0.08	0.0020	92.7	23.29

*Based on load

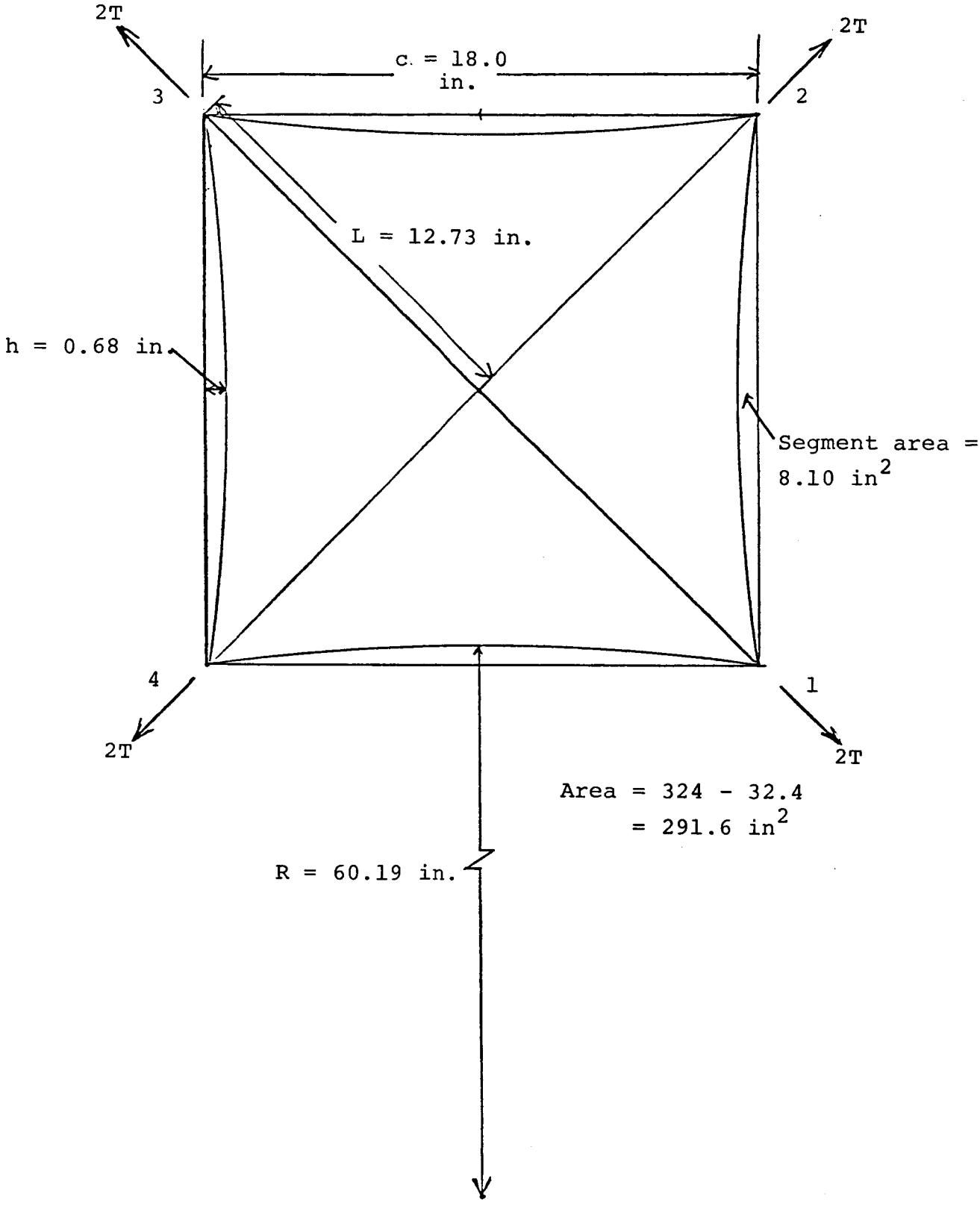


Figure B-1. Foil surface dimensions and loading pattern.

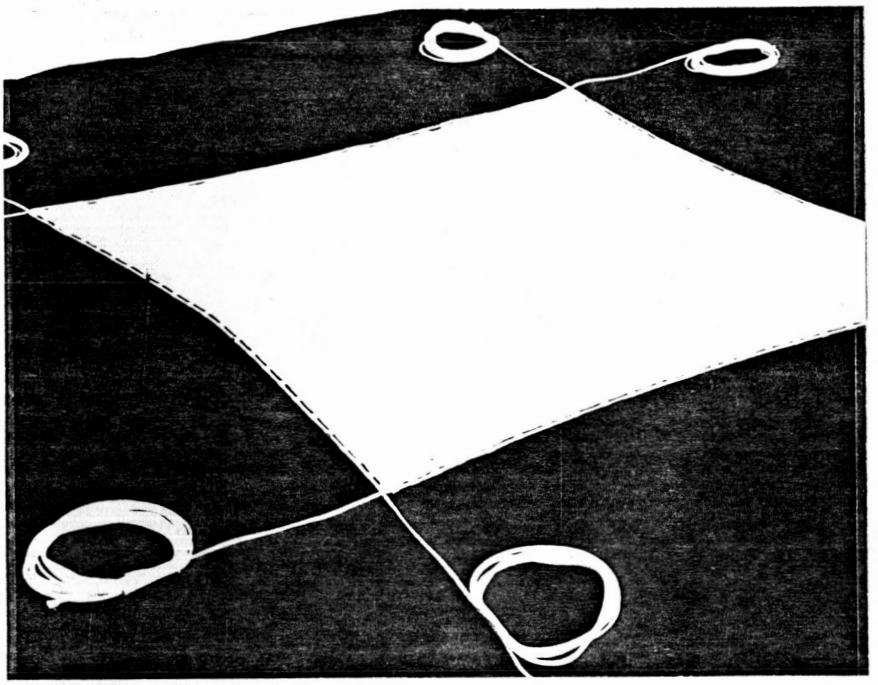


Figure B-2. Foil surface ready for folding.

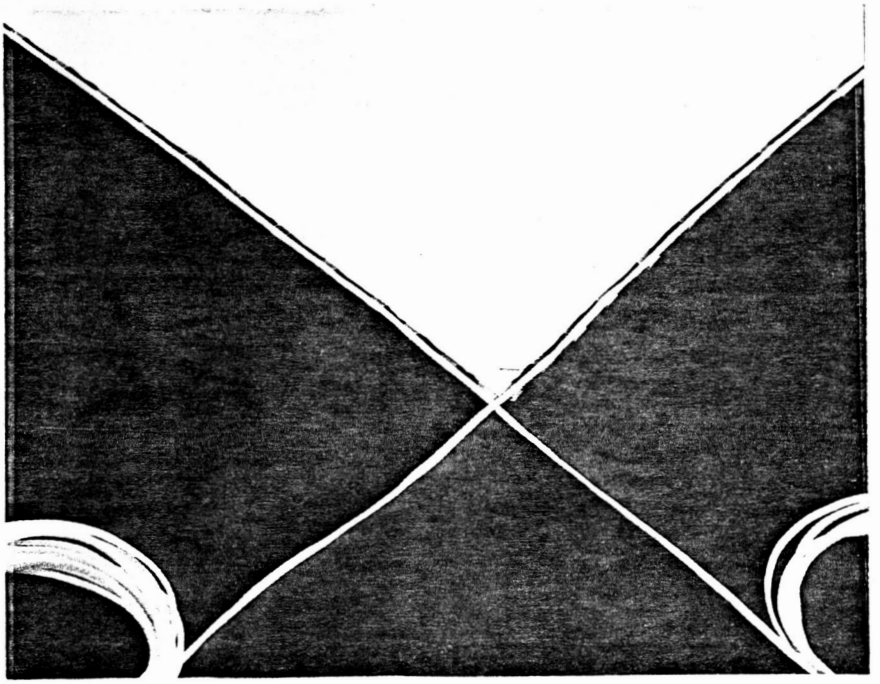


Figure B-3. Detail of tabs and corner.

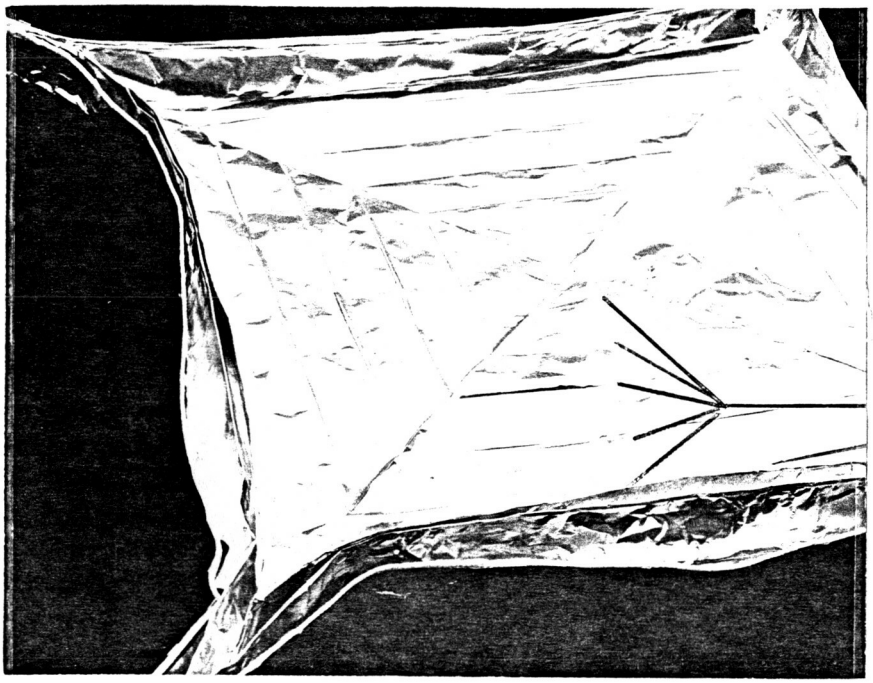


Figure B-4. Foil surface being folded (note 2.0-cm-wide folding guides).

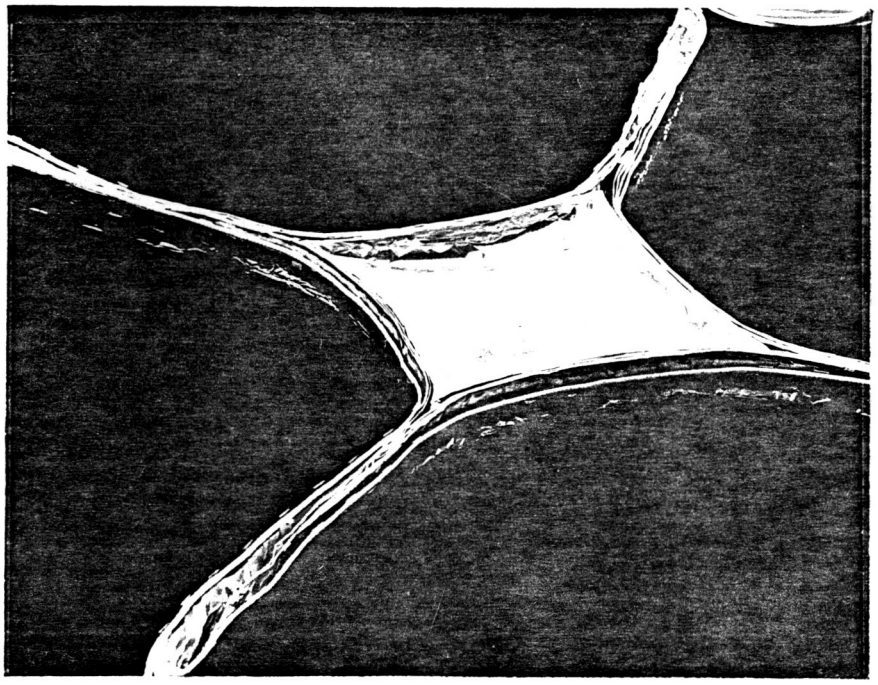


Figure B-5. Foil surface being folded.

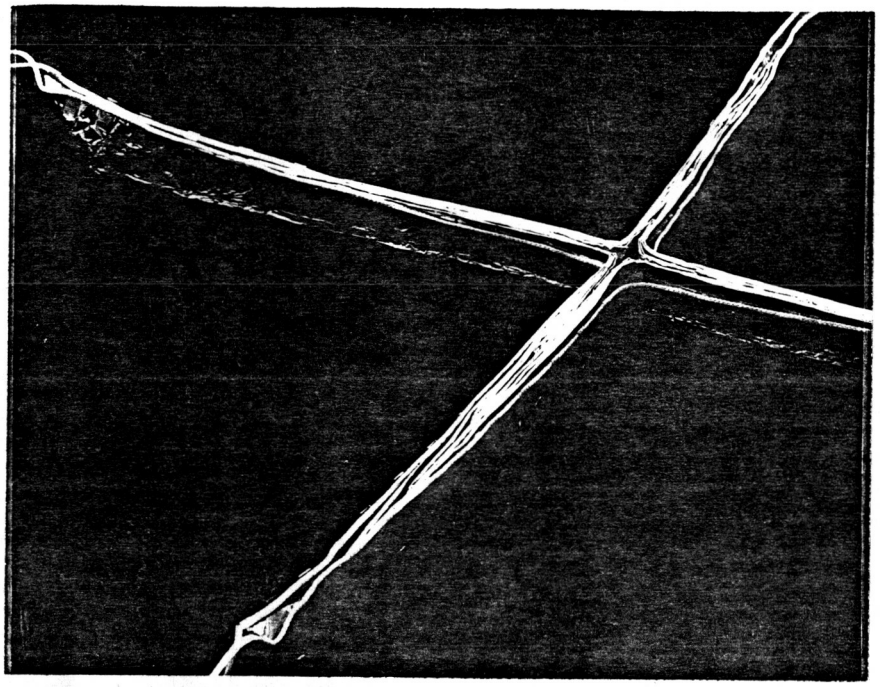


Figure B-6. Final folding before folds set and "arms" coiled.

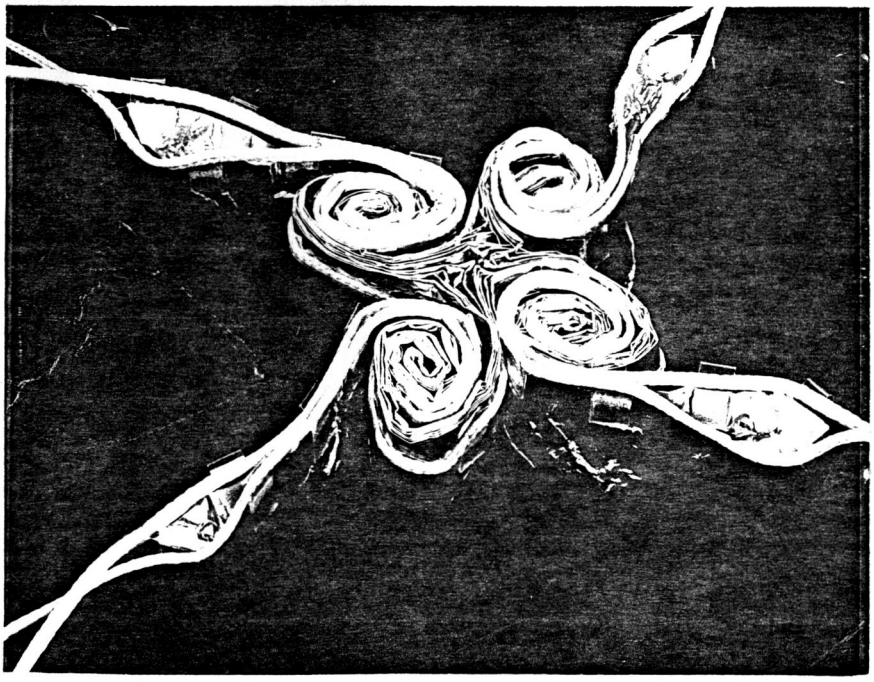


Figure B-7. Final stowed configuration.

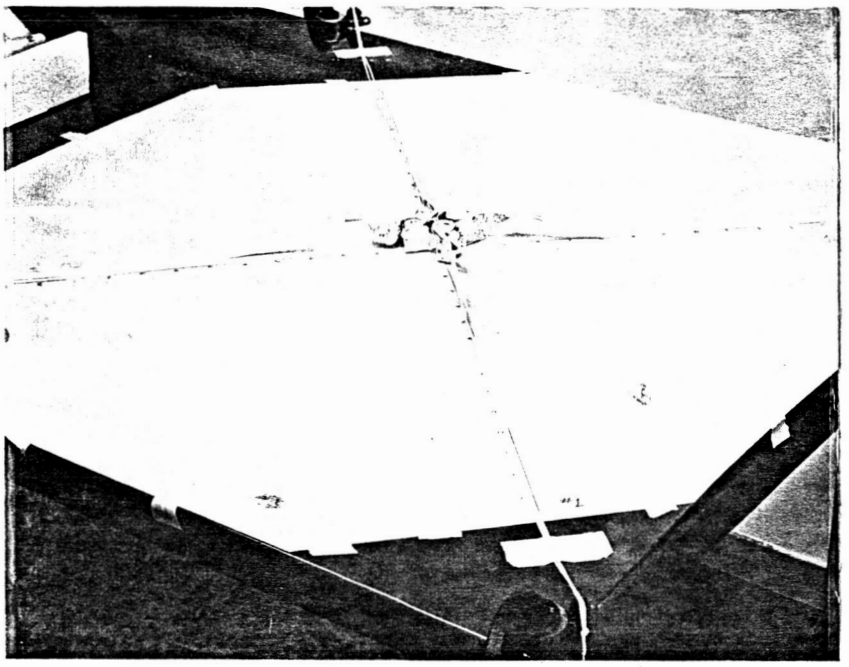


Figure B-8. Test setup, no load.

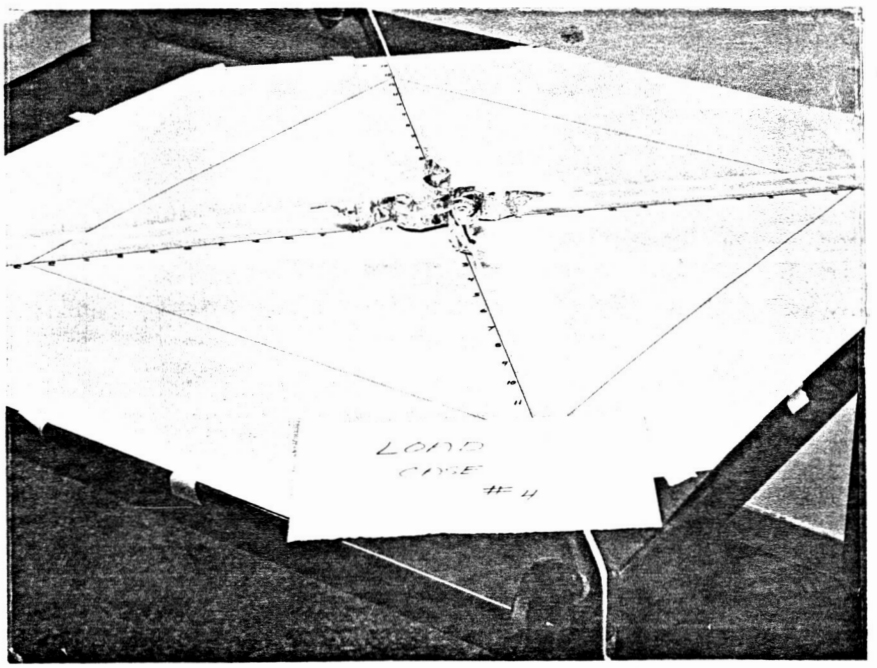


Figure B-9. Load Case No. 4.

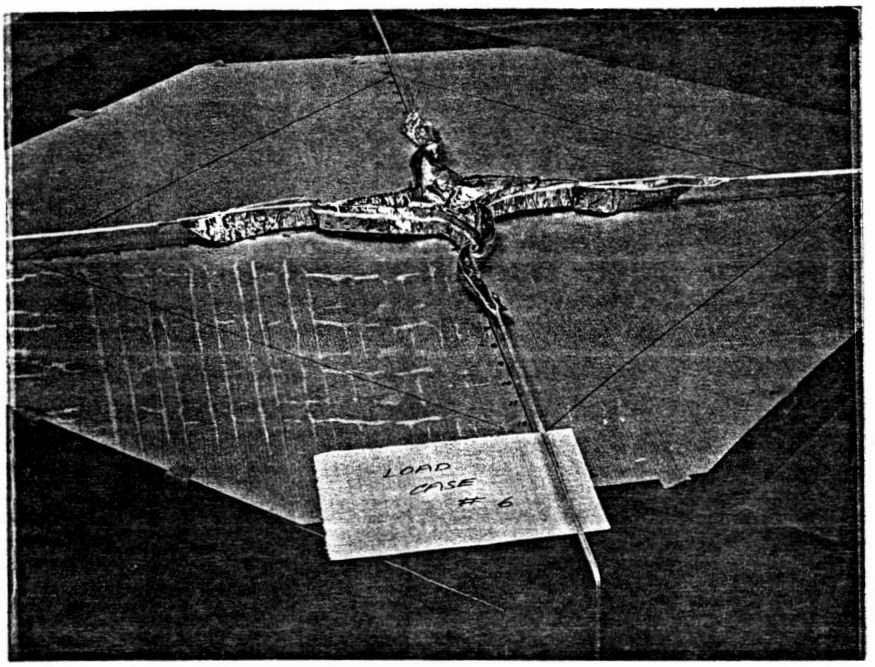


Figure B-10. Load Case No. 6.

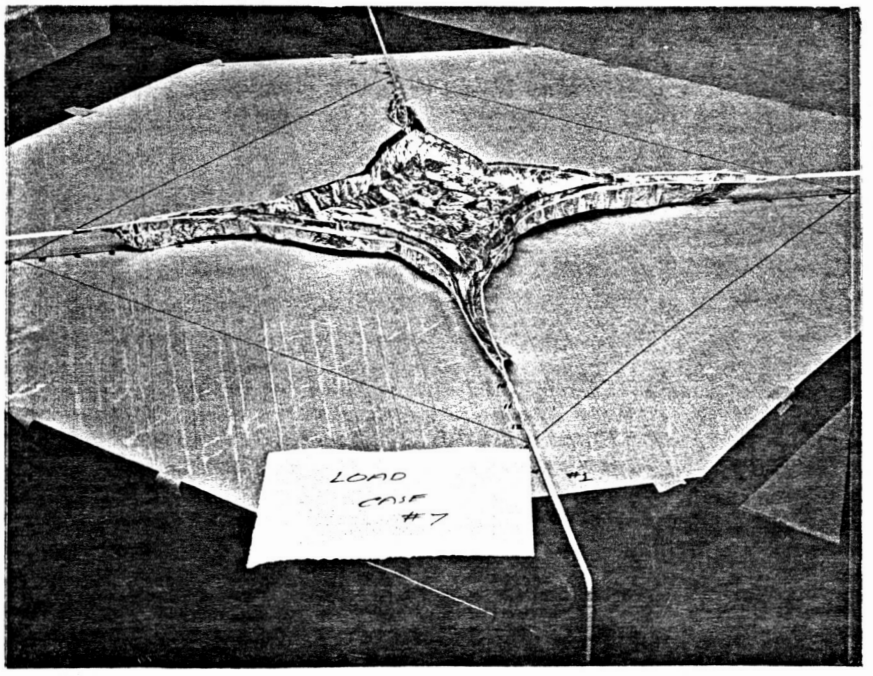


Figure B-11. Load Case No. 7.

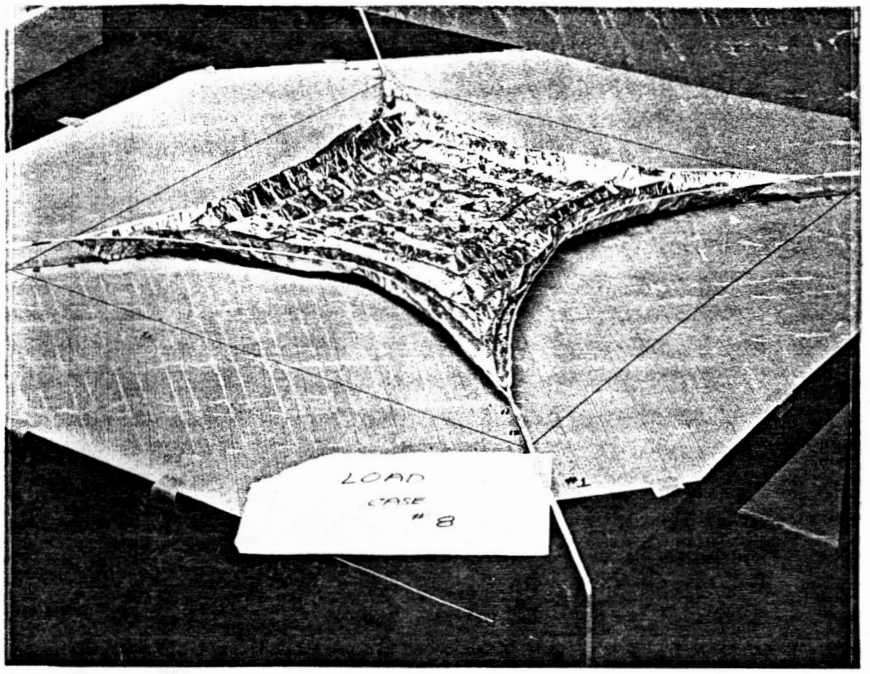


Figure B-12. Load Case No. 8.

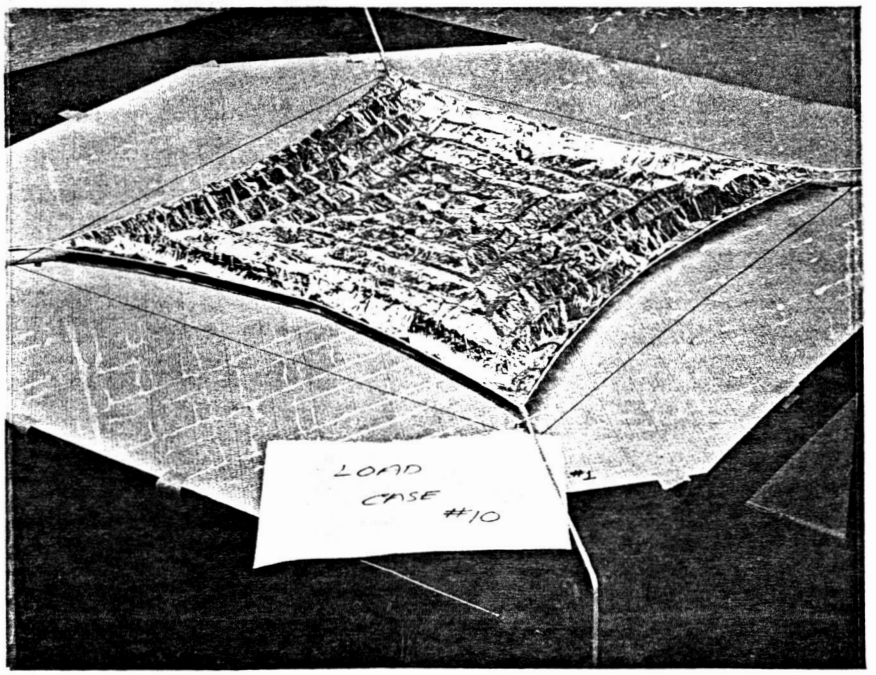


Figure B-13. Load Case No. 10.

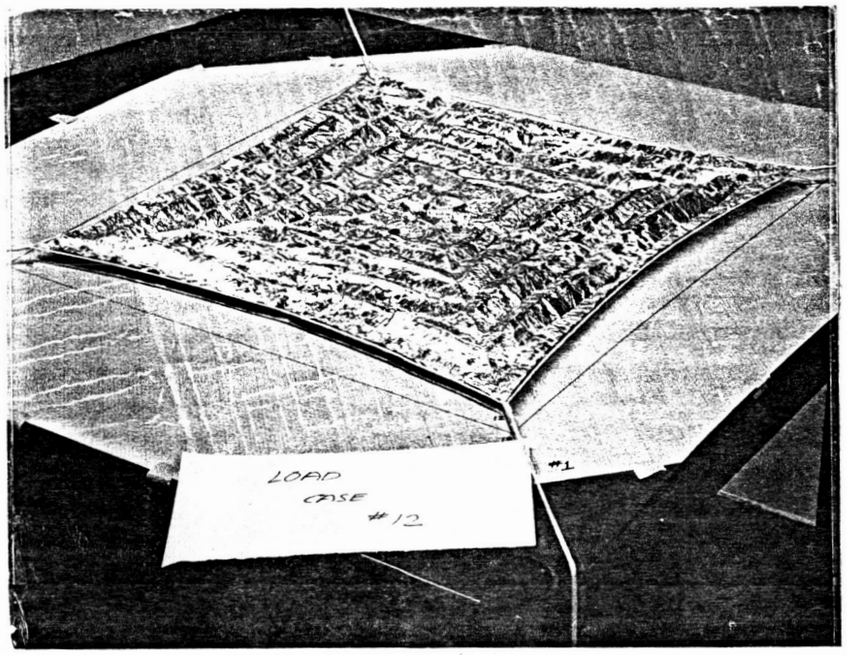


Figure B-14. Load Case No. 12.

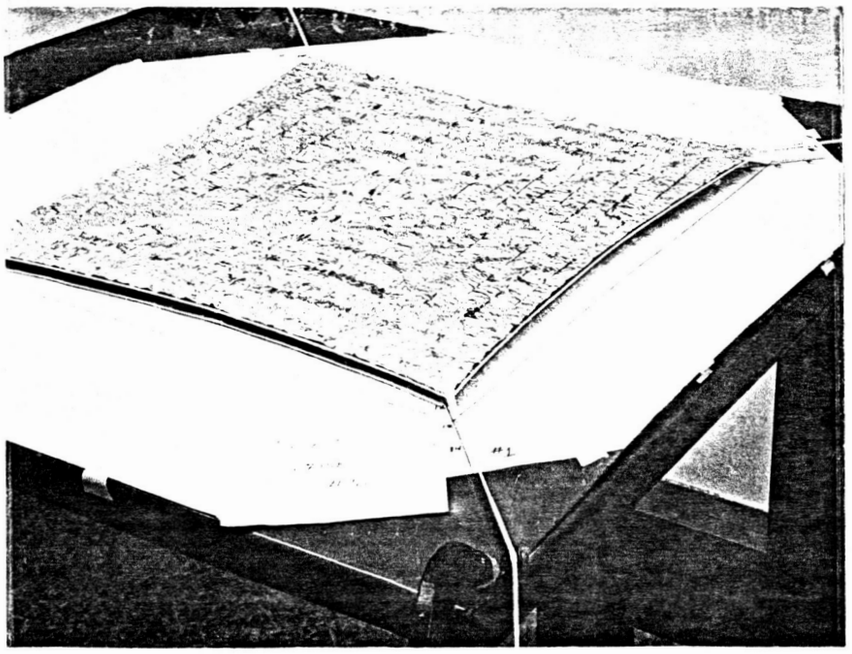


Figure B-15. Load Case No. 16.

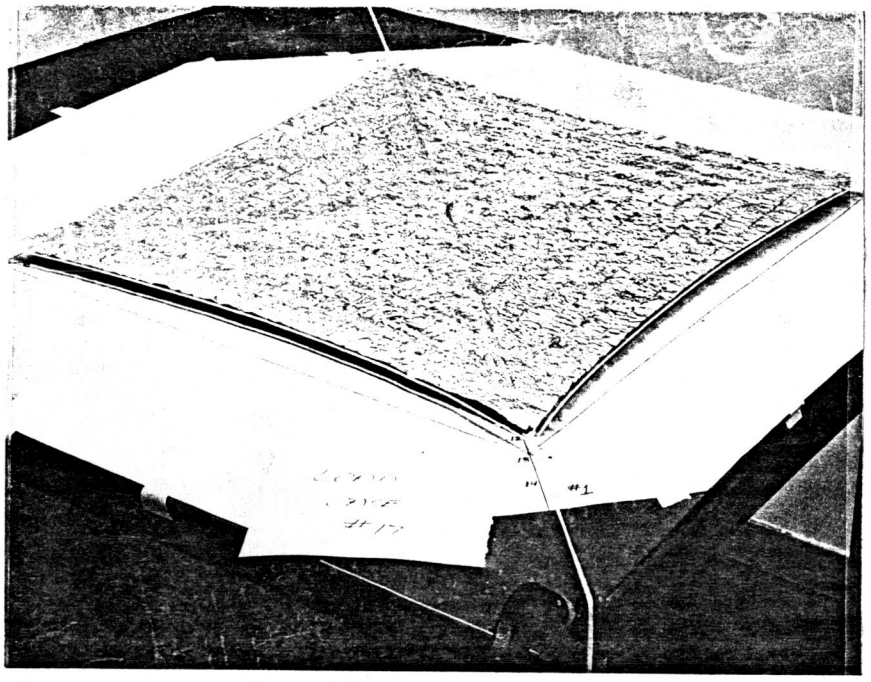


Figure B-16. Load Case No. 17.

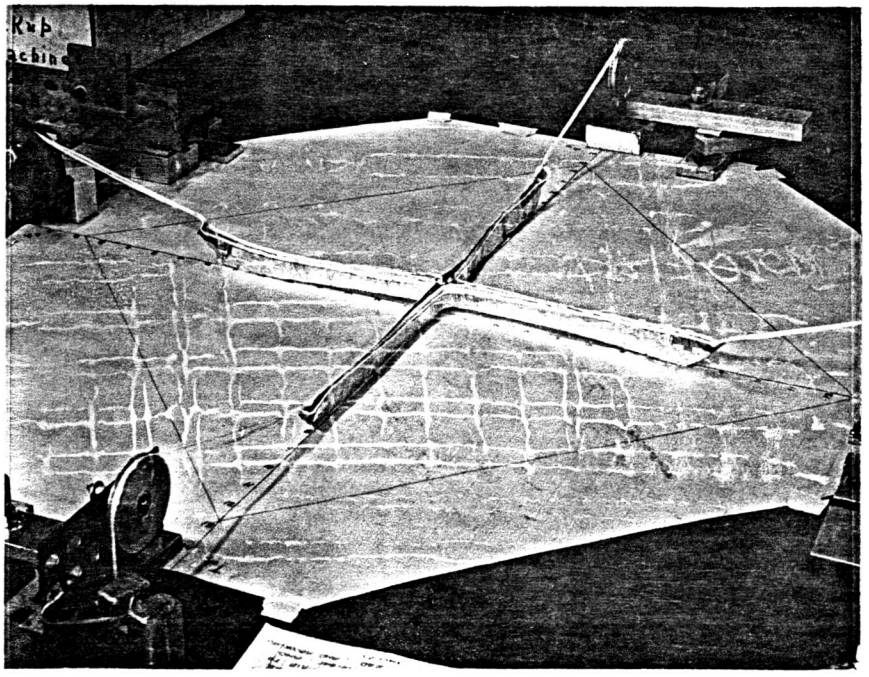


Figure B-17. Fold/wrinkle height test setup.

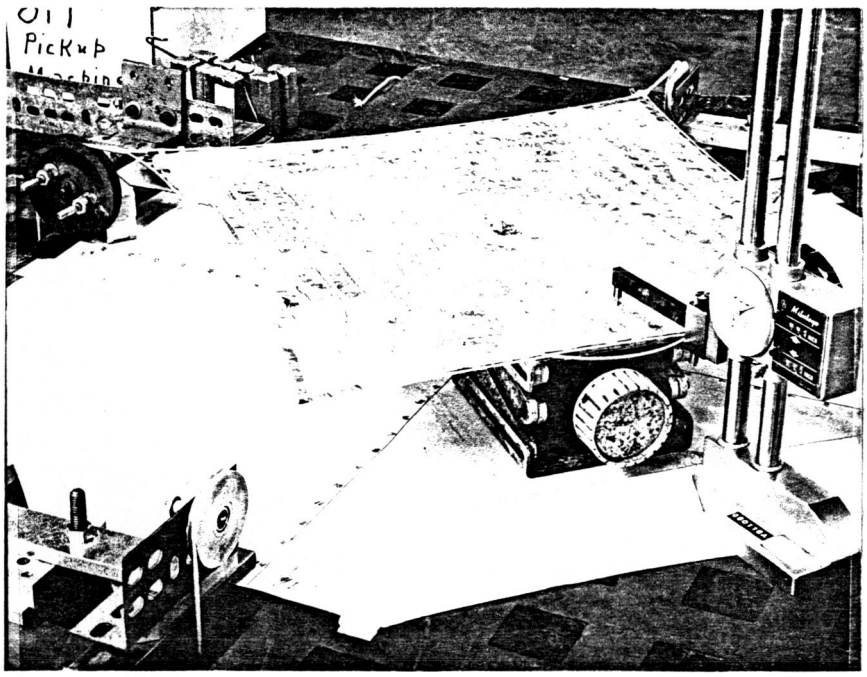


Figure B-18. Fold/wrinkle height measurement arrangement.

CHAPTER 4

METEOROID DAMAGE TO ROD-TYPE STRUCTURAL ELEMENTS

by

John M. Hedgepeth

TABLE OF CONTENTS

INTRODUCTION 222

METEOROID STATISTICS 222

Flux 223
Hits on a Long Cylinder 224

FRACTURES BY THE "SWEPT-AREA" CRITERION 226

APPLICATION TO EARTH ORBIT 229

REFERENCES 231

INTRODUCTION

Large space structures are likely to be built up from many rod-type structural elements. While the change of meteoroid damage to any particular element is very small, the chance of damage somewhere in the structure may be appreciable because of the large total length of the elements. Little is known of the meteoroid damage characteristics of linear elements besides the early treatment in Reference 1. No experimental data exist at present. This report contains further theoretical study of the problem.

METEOROID STATISTICS

Let n(m) be the density function per unit volume for meteoroids of mass m and let the velocity components of each meteoroid be random variables with Gaussian statistics. Let the probability distribution function be denoted as

$$f(\vec{v}) = \frac{n(m)}{\left(\frac{2\pi}{3} U^2\right)^{3/2}} e^{-3\left(v_x^2+v_y^2+v_z^2\right)/2U^2} \tag{1}$$

where U is the rms velocity magnitude. Note that we have assumed stationarity and isotropy.

The expected number of meteoroids in a volume S with a mass between m and m+dm and velocity components in the intervals (v_x, v_x+dv_x), (v_y, v_y+dv_y), (v_z, v_z+dv_z) is

$$dq = Sf(\vec{V})\ dm\ dv_x dv_y dv_z$$

which can also be written as

$$dq = Sf(\vec{v})\ dm\ V^2 \sin\theta\ dV d\theta d\phi \tag{2}$$

where we have set

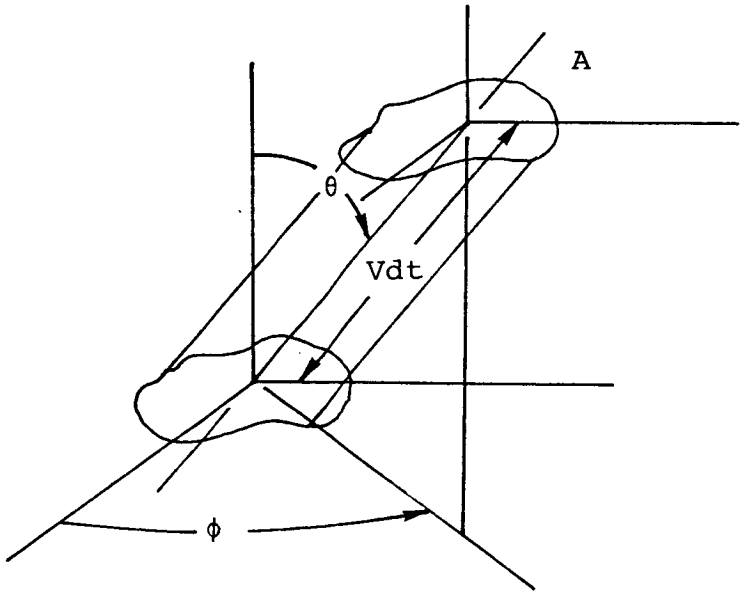
$$v_x = V \sin\theta \cos\theta$$
$$v_y = V \sin\theta \sin\theta$$
$$v_z = V \cos\theta$$

Note

$$v_x^2 + v_y^2 + v_z^2 = V^2$$

Flux

Consider the area A in the x-y plane. We would like to determine the number of meteoroids of mass between m and m+dm with flow through the area A from one side per unit time.



Select the lower side as the one through which the meteoroids are passing. Then all the meteoroids in the cylindrical volume shown above that have spherical-coordinate velocity components of V, θ, and ϕ pass through the area A in the unit time. Thus the total

rate of flow from all directions coming from below is

$$\frac{d\dot{Q}}{dm} = \int_0^{\infty} \int_0^{\pi/2} \int_0^{2\pi} AV \cos\theta \, f(\vec{V}) \sin\theta \, V^2 \, d\theta d\phi dV \tag{3}$$

Substituting from Eq. (1) and performing the integrations yields

$$\frac{d\dot{Q}}{dm} = \frac{n(m)U}{\sqrt{6\pi}} A \tag{4}$$

Let $N(m)$ be the number density of meteoroids of mass m or greater so that

$$N(m) = \int_m^{\infty} n(m)dm$$

Let $\Phi(m)$ be the number flux per unit area from one side of meteoroids with mass greater than or equal to m. Then

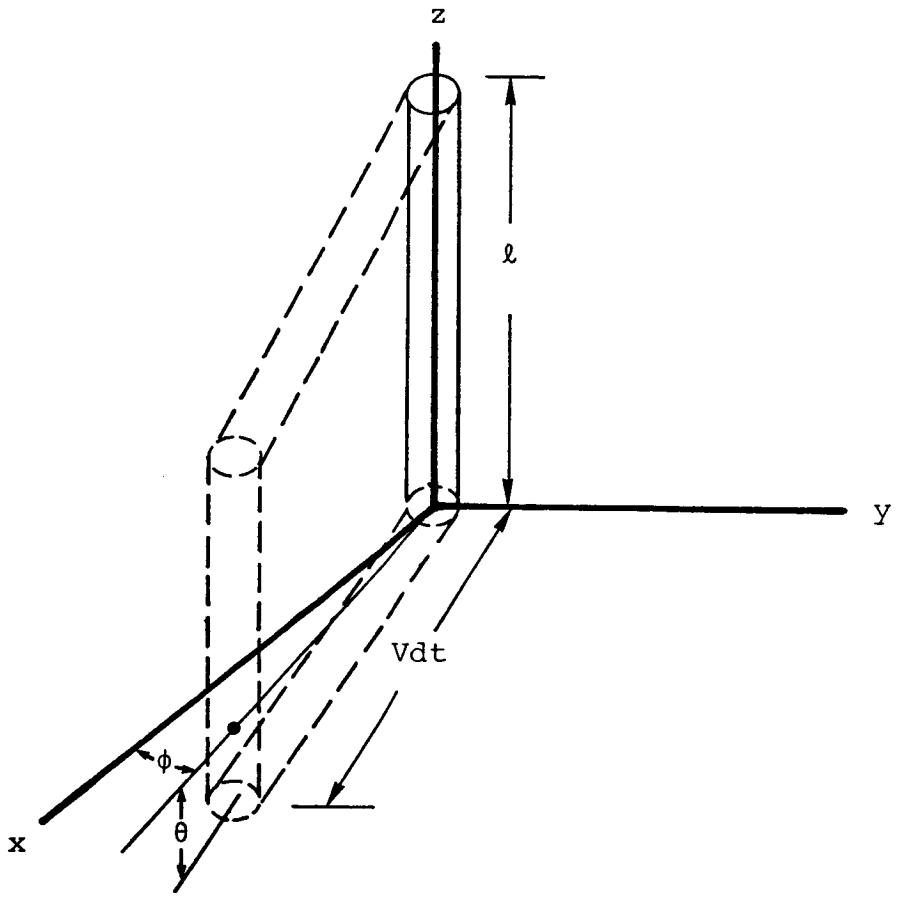
$$\Phi(m) = \frac{UN(m)}{\sqrt{6\pi}} \tag{5}$$

In many cases, the data for meteoroid frequency are approximated by the formula

$$N(m) = Km^{-\gamma} \tag{6}$$

Hits on a Long Cylinder

Consider a circular cylinder of diameter d and length $\ell >> d$ as shown in the following figure:



In the same way as before, all the meteoroids with velocity-component coordinates of V, θ, ϕ in the above volume of $V\ell d \sin\theta$ will hit the cylinder in a unit time. All meteoroids with velocity-component coordinates of V, θ, ϕ outside of that volume will miss the cylinder. Thus, the total rate of hits from all directions is

$$\frac{d\dot{Q}}{dm} = \int_0^{\infty}\int_0^{\pi}\int_0^{2\pi} V\ell d \sin\theta \; f(\vec{v}) \sin\theta \; v^2 d\phi d\theta dv$$

Substituting for $f(\vec{v})$ and integrating gives

$$\frac{d\dot{Q}}{dm} = \pi d\ell \frac{n(m)}{\sqrt{6\pi}} U \qquad (7)$$

The number of hits per unit time with a mass equal to or greater than m is

$$H(m) = \int_m^\infty \frac{d\dot{Q}}{dm}\, dm$$

or

$$H(m) = \pi d\ell\ \Phi(m) \tag{8}$$

where we have made use of the flux equation, Eq. (5).

Average Meteoroid Velocity

The "average" velocity V_{ave} can be obtained as

$$V_{ave} = \frac{1}{n(m)} \int_0^\infty \int_0^\pi \int_{-\pi}^\pi Vf(\vec{V})\ V^2 \sin\theta\ d\theta d\phi$$

$$= \frac{4\pi}{\left(\frac{2\pi}{3}\right)^{3/2} U^3} \int_0^\infty V^3\ e^{-3V^2/2U^2}$$

Evaluating the integral gives

$$V_{ave} = \sqrt{\frac{8}{3\pi}}\ U \tag{9}$$

FRACTURES BY THE "SWEPT-AREA" CRITERION

According to Reference 2, the penetration depth is, for semi-infinite targets

$$P_\infty = k_\infty\ m^{0.352}\ \rho_m^{1/6}\ V^{2/3} \tag{10}$$

where

m = meteoroid mass, g

ρ_m = meteoroid density, g/cc

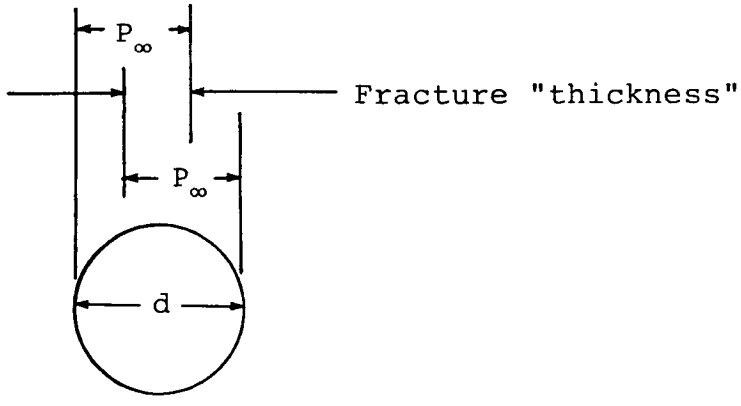
V = meteoroid velocity, km/s

P_∞ = penetration depth, cm

k_∞ = a constant (= 0.42 for aluminum)

According to Reference 3, Denardo, et al, find that the crater diameter is approximately twice the penetration. Let us assume that the long cylinder will fracture whenever the cylinder of radius equal to P_∞ (Eq. (12)) about the meteoroid path encompasses the entire cylinder. Thus, if any part of the cylinder is not swept out by the destructive zone, the cylinder is assumed to be unfractured. This criterion seems to be particularly appropriate for unidirectional filamentary composites.

If $P_\infty(m,V) < d/2$, then there is no fracture. If $P_\infty(m,V) > d/2$, then the thickness of the volume containing meteoroids that will produce fracture is $2P_\infty - d$.



Therefore, the number of fractures per unit time will be (see Eq. (6))

$$\dot{N}_f = \int_0^{\infty} dm \int_{V^*}^{\infty} \int_0^{\pi} \int_{-\pi}^{\pi} (2P_{\infty}-d) V\ell \sin\theta \, f(\vec{v}) \sin\theta \, V^2 d\phi d\theta dv$$

$$= \pi^2 \int_0^{\infty} dm \int_{V^*}^{\infty} (2P_{\infty}-d) V^3 \ell f(V) dV \qquad (11)$$

where V^* is the velocity for which $P_{\infty} = d/2$. Reversing the order of integration and substituting for $f(V)$ yields

$$\dot{N}_f = \frac{3}{2U^3}\sqrt{\frac{3\pi}{2}}\,\ell \int_0^{\infty}\int_{m^*}^{\infty} (2P_{\infty}-d) V^3 \, e^{-3V^2/2U^2} \, n(m)\, dm dV \qquad (12)$$

where, now m^* is the mass (as a function of V) for which $P_{\infty} = d/2$. Thus

$$m^*(V) = \left(\frac{d}{2k_{\infty}\rho_m^{1/6} V^{2/3}}\right)^{1/0.352} \qquad (13)$$

From Eq. (6) we get

$$n(m) = \gamma K m^{-\gamma-1}$$

Then integrating gives

$$\dot{N}_f = \frac{3}{2U^3}\sqrt{\frac{3\pi}{2}}\,\frac{0.352}{\gamma-0.352}\,Kd\ell\left(\frac{2k_{\infty}\rho_m^{1/6}}{d}\right)^{\gamma/0.352}$$

$$\int_0^{\infty} V^{3+(2\gamma/3\ 0.352)} \, e^{-3V^2/2U^2} \, dV \qquad (14)$$

Substituting t for $3V^2/(2U^2)$ gives

$$\frac{\dot{N}_f}{\dot{N}_{f_1}} = \frac{(2/3)^{\gamma/1.056}}{(\gamma/0.352)-1} \int_0^\infty t^{(\gamma/1.056)+1} e^{-t} dt \qquad (15)$$

where N_{f_1} is the simple-minded estimate obtained by assuming that all meteoroids with larger mass than m*(U) (Eq. (13)) will fracture the cylinder if they strike it. Thus from Eqs. (5) and (8)

$$\dot{N}_{f_0} = \sqrt{\frac{\pi}{6}}\, d\ell UN(m^*[U]) \qquad (16)$$

The integral in Eq. (15) can be evaluated in terms of the gamma function to yield

$$\frac{\dot{N}_f}{\dot{N}_{f_0}} = \frac{(2/3)^{\gamma/1.056}}{(\gamma/0.352)-1}\, \Gamma\left(\frac{\gamma}{1.056} + 2\right) \qquad (17)$$

APPLICATION TO EARTH ORBIT

For earth orbit, the meteoroid flux is given in Reference 4 to be

$$\Phi = 4.26 \times 10^{-15}\, \eta m^{-1.213}$$

for the mass m in grams greater than 10^{-6}. The factor η accounts for the effects of earth shadowing and defocusing. It varies from 0.5 at the Earth's surface to a maximum of 0.691 at an altitude of three Earth radii and decreases to about 0.619 at GEO. We therefore set, with only slight conservatism,

$$\eta = 0.7$$

The average velocity is given as 20 km/s. Thus, from Eq. (9)

$$U = 21.7 \text{ km/s}$$

Referring to Eq. (5), we can solve for N(m) to give

$$N(m) = 5.97 \times 10^{-19} \; m^{-1.213} \text{ particles/m}^3$$

Thus,

$$K = 5.97 \times 10^{-19} \text{ particles/m}^3$$

$$\gamma = 1.213$$

For this value of γ

$$\frac{\dot{N}_f}{\dot{N}_{f_0}} = \frac{(2/3)^{1.149}}{2.45} \Gamma \; (3.149)$$

$$= 0.59$$

The value of m*(U) is obtained from Eq. (13) to be

$$m^*(U) = \left[\frac{d}{2 \times 0.42 \times (0.5)^{1/6} \times (21.7)^{2/3}} \right]^{1/0.352}$$

where we have used $k_\infty = 0.42$ (aluminum) for want of a better value, and $\rho = 0.5$ g/cc.

This gives

$$m^*(U) = 0.0067 \; d^{2.84}$$

where d is in centimeters.

Substituting into Eqs. (15) and (16) with ℓ = 1 m gives the fracture rate/m/s of

$$\dot{N}_f = 0.59 \times \sqrt{\frac{\pi}{6}} \times \frac{d}{100} \times 21{,}700 \times 5.97 \times 10^{-19}$$

$$\times (0.0067)^{-1.213} \times d^{-2.84 \times 1.213}$$

$$= 2.4 \times 10^{-14}\ d^{-2.44} \text{ fractures/m/s}$$

$$= 7.6 \times 10^{-7}\ d^{-2.44} \text{ fractures/m/yr}$$

For members 1 cm in diameter and a total length of 1 km, the probability of a fracture in 10 years is about 0.008. On the other hand, if the diameter is only 1 mm and the length is 1 km, then the probability of a fracture in one year is about 0.2, which is too high.

REFERENCES

1. MacNeal, R.H.: Meteoroid Damage to Filamentary Structures. NASA CR-869, September 1967.
2. Meteoroid Damage Assessment. NASA SP-8042, May 1970.
3. Denardo, B.P.; et al.: Projectile Size Effects on Hypervelocity Impact Craters in Aluminum. NASA TN D-4067, 1967.
4. Meteoroid Environmental Model - 1969 (Near Earth to Lunar Surface). NASA SP-8013, March 1969.

1. Report No.	2. Government Accession No.	3. Recipient's Catalog No.
NASA CR-165744		

4. Title and Subtitle	5. Report Date
Considerations in the Design of Large Space Structures	August 1981
	6. Performing Organization Code
7. Author(s)	8. Performing Organization Report No.
John M. Hedgepeth, Richard H. MacNeal, Karl Knapp, and Charles S. MacGillivray	ARC-TN-1101
	10. Work Unit No.
9. Performing Organization Name and Address	11. Contract or Grant No.
Astro Research Corporation 6390 Cindy Lane Carpinteria, CA 93013	NAS1-15347
	13. Type of Report and Period Covered
12. Sponsoring Agency Name and Address	Contractor Report
National Aeronautics and Space Administration Washington, DC 20546	14. Sponsoring Agency Code

15. Supplementary Notes

NASA Langley Technical Monitor: Dr. Melvin S. Anderson

16. Abstract

This report contains several analytical studies of topics relevant to the design of large space structures. Topics covered are:

1. The types and quantitative evaluation of the disturbances to which large Earth-oriented microwave reflectors would be subjected and the resulting attitude errors of such spacecraft
2. The influence of errors in the structural geometry of the performance of radiofrequency antennas
3. The effect of creasing on the flatness of tensioned reflector membrane surfaces
4. An analysis of the statistics of damage to truss-type structures due to meteoroids.

17. Key Words (Suggested by Author(s))	18. Distribution Statement
Large space structures	Unclassified - Unlimited

19. Security Classif. (of this report)	20. Security Classif. (of this page)	21. No. of Pages	22. Price
Unclassified	Unclassified	231	

For sale by the National Technical Information Service, Springfield, Virginia 22161